Max-Planck-Institut für Plasmaphysik

Study of Microinstabilities Using the Paraxial WKB Method

Monica Şerbu (geb. Apostoliceanu)

Technische Universität München

2005

Technische Universität München
Fakultät für Physik
Max Planck Institut für Plasmaphysik

Study of Microinstabilities Using the Paraxial WKB Method

Monica Şerbu (geb. Apostoliceanu)

Vollständiger Abdruck der von der Fakultät für Physik der Technischen Universität München zur Erlangung des akademischen Grades eines Doktors der Naturwissenschaften (Dr. rer. nat.) genehmigten Dissertation.

Vorsitzender:	Univ.-Prof. Dr. E. Nolte
Prüfer der Dissertation:	1. Hon.-Prof. Dr. R. Wilhelm
	2. Univ.-Prof. Dr. M. Kleber

Die Dissertation wurde am 10.02.2005 bei der Technischen Universität München eingereicht und durch die Fakultät für Physik am 08.04.2005 angenommen.

"The flapping of a single butterfly's
wing today produces a tiny change
in the state of the atmosphere. Over
a period of time, what the atmosphere
actually does diverges from what it
would have done. So, in a month's time,
a tornado that would have devastated
the Indonesian coast doesn't happen.
Or maybe one that wasn't going to
happen, does."
(Ian Stewart, Does God Play Dice?
The Mathematics of Chaos)

Abstract

The concept of energy production through the fusion of two light nuclei has been studied since the 1950'. The main goal of controlled thermonuclear fusion research is to achieve a high density and high temperature plasma for a long confinement time. The most common way to confine the plasma is the tokamak. In the tokamak the energy and particle loss was found to be much larger than the neoclassical transport and is called anomalous transport. Today is commonly accepted that anomalous transport is due to microinstabilities driven by temperature and density inhomogeneities. The present Thesis is centered on the study of two major microinstabilities, trapped electron mode (TEM) and ion temperature gradient (ITG).

In studying the microinstabilities, first a linear gyrokinetic code, GS2, was applied to ASDEX Upgrade L-mode discharges heated with Electron Cyclotron Heating. The most unstable mode is found to be the TEM. The scan performed around the parameters obtained from the experiment has revealed that the growth rate of the mode depends on several plasma parameters that are not usually considered when analyzing the experiments, such as the density gradient length, R/L_{ne}, and collisions. The direct comparison of the observed heat flux with results obtained using quasi-linear theoretical calculations shows a good agreement. Both, the experiments as well as calculations show that there is a threshold for the TEM. The normalized growth rate obtained from the gyro-kinetic stability calculations has been also compared with Weiland and GLF23 models. A relative good agreement has been found between GS2 and GLF23 models, whereas the Weiland model performs less well (especially the shear dependence).

The ITG turbulence is generally believed to cause the observed anomalous loss of particles and heat at the core of the tokamak. The study of the ITG mode is performed using a two-fluid model, parallel ion dynamics being also included. Both, analytical and numerical calculations are employed , using a novel asymptotic approach, the beam tracing technique (BT), for solving the eigenvalue problem in the short wavelength limit. To validate the numerical results, the dependence of the ITG mode on different parameters, i.e η_i, T_e, q, is compared with Weiland model. For this comparison, a simplified BT model is used. Dependence on the Shafranov shift, on the elongation and on the magnetic shear is studied.

Acknowledgements

The present research work has been carried out during 2001-2005 at the Tokamak Division, Max-Planck Institut für Plasmaphysik (IPP), Garching. I own thanks to many people who made this thesis possible.

First I would like to express my sincere gratitude to Prof. Wilhelm for his academic supervision. My thesis advisors, Grigori Pereverzev and Arthur Peteers, deserve my most sincere appreciation for supplying the very interesting topic, for their cordiality and all the support and especially for contributing their expertise to this work. Their foresight, physical intuition, and integrity have been a constant guide throughout this entire work.

Thanks to my colleagues, Dr. Clemente Angioni, Dr. F. Jenko, Dr. Giovanni Tardini for permanent collaboration and helpful discussions. I would like to address my thanks to Dr. F. Ryter and ASDEX Up-grade team for providing us with experimental data. Also thanks are expressed to the members of the Tokamak Division at IPP, for their kind collaboration, the friendly working atmosphere. I want to thank to all my friends here in the institute for being with me all these three years and for supporting me in all the situations.

My very special thanks are going to my sister and my brother-in-low, for their unconditioned love and permanent support. Many thanks to all of my family for their guidance and unfailing support. The last, but not the least I address my thanks to Dan, my husband, for his unwavering patience, understanding and encouragement to the whole work. His warmth, love and compassion have enriched my life, and carried me through difficult times.

All of the above and many others have contributed substantially in one way or another to the preparation of this thesis. I express my deepest gratitude and appreciation to all of them.

This dissertation is dedicated to my father, "in memoriam", and to my mum, as the culmination of a long education that they have supported at every step.

Monica Apostoliceanu
Garching, February 2005

Contents

Chapter 1

Introduction

1.1 Thermo-Nuclear Fusion

The development of alternative energy sources is stimulated by the increasing world-wide energy demand. Nowadays, the largest amount of electricity is produced by burning fossil fuel, which is expected to cover the energy needs for the intermediate time, but serious questions have been raised about the impact on the ecosystem and the climate.

For long term strategy the nuclear power as well as renewable energy sources are considered valid alternatives. Energy can be gained from the mass loss after a nuclear reaction, such as the splitting of a heavy nucleus into two lighter ones, or the fusion of hydrogen isotopes to give helium. In industrialized countries, nuclear fission is developed enough to deliver already a significant amount of energy. However, radioactive waste, with an extremely long lifetime, cannot be avoided. Nuclear fusion would have also waste, since the inner walls of a reactor would be activated by neutrons. However, improvements are achieved by choosing appropriate walls and structure materials of low activation. Fusion, as a source of energy, would have many advantages: abundant fuel supply, no risk of nuclear accidents, since no fossil fuels are used, air pollution will not exist.

To produce energy through thermonuclear controlled fusion is still a challenging goal. An economically attractive fusion power plant is desired. A big difficulty appears in realizing it, namely, the very low cross-section of the reaction, due to the Coulomb barrier between charged nuclei. However, the cross-section increases with energy so that this inhibition is overcome by increasing the average kinetic energy. The energy required for fusion is so high that fusion only occurs in appreciable amounts once the temperature gets over 10 millions K. At such temperature the

fuel is fully ionized. The electrostatic charge of the nuclear ions is neutralized by the presence of an equal number of electrons and the resulting neutral gas is called plasma. On Earth, the most feasible fusion reactions are listed in Table 1.1. For temperatures below 500 keV the D-T reaction exhibits the highest cross section and a very good energy production rate (17 MeV per reaction).

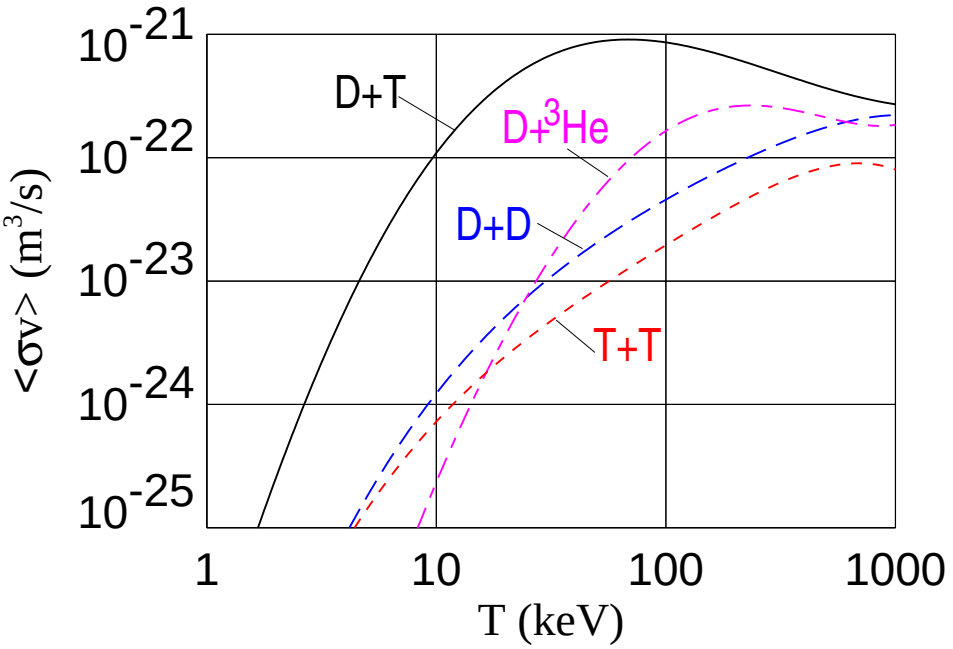

Figure 1.1: Reaction parameters $< \sigma v >$ as a function of T_i for different fusion reaction

D + D → n (2.45 MeV) + ^{3}He (0.82 MeV) [50%]
D + D → p (3.02 MeV) + T (1.01 MeV) [50%]
D + T→ n (14.04 MeV) + ^{4}He (3.54 MeV)
D + ^{3} He→ p(14.64 MeV) + ^{4}He (3.71 MeV)

Table 1.1: Most relevant fusion reactions with deuterium. The particle energy after the reaction is reported in the round brackets.

Therefore, it is the best candidate for a fusion reactor, even if tritium does not occur naturally. The later problem can be solved using the neutrons produced in the D-T reaction. Surrounding the plasma with Lithium, a second reaction can produce Tritium which can be gathered and used for plasma fueling.

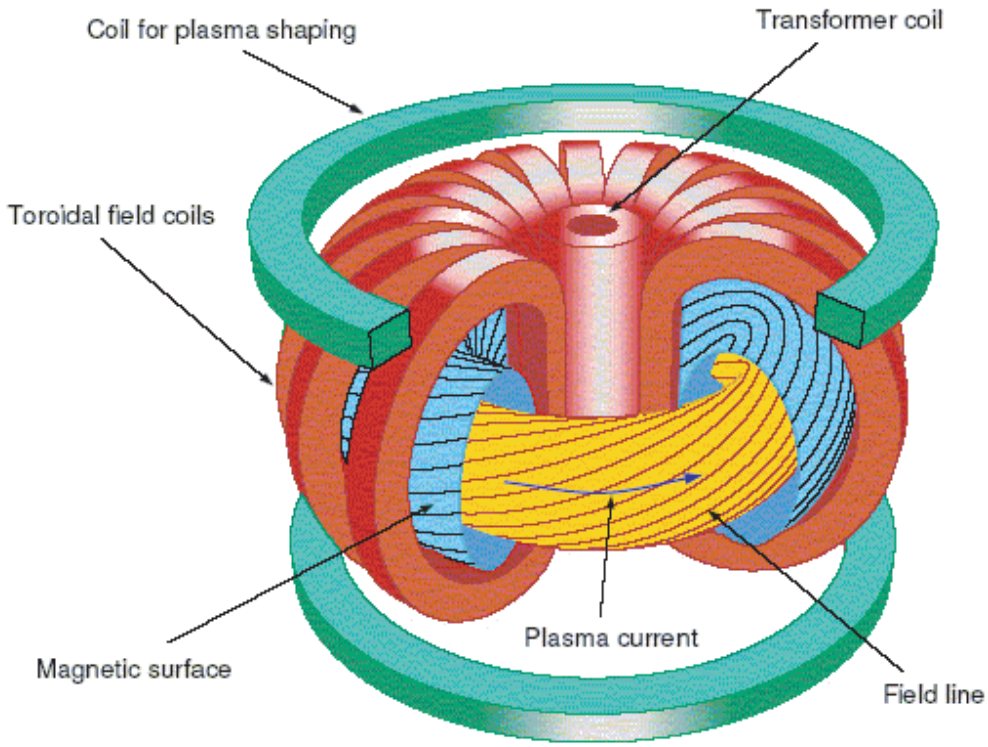

Figure 1.2: Tokamak configuration: The innermost cylinder is the transformer coil which induces the toroidal current and thus the poloidal magnetic field. The ring of D-shaped coils creates the toroidal magnetic field. The resulting field lines run helicoidally on the nested toroidal surfaces. The horizontal coils generate a vertical magnetic field for the radial plasma equilibrium as well as for plasma shaping.

The D-T reaction rate starts to be relevant at particle energies of 10 keV or more. The aim is to achieve the ignition where, as in the case of fossil fuels, the burning process becomes self-sustaining without further applied heating. The conditions needed to induce fusion reactions are so extreme that virtually natural fusion occurs only in the interior of stars. In this case, the gravity compresses the gas, until the temperature and pressure forces balance the gravitational compression. If there is enough material in the star, pressure and temperature will grow large enough and the fusion begins to occur. To obtain ignition on Earth, two approaches are under investigation: "inertial fusion" creates very dense plasmas for a short time, "magnetic fusion" confines a relatively rarefied, hot plasma for a long time with the

use of a magnetic field.

In the present fusion experiments ignition has not yet been reached: it is necessary to supply power from outside to obtain the desired high temperature. One of the main problems is the relatively large transport of the heat out of the plasma. In the last 50 years many different approaches were investigated in order to approach the fusion reaction. Among them, the most advanced concept towards the achievement of the required fusion reactor parameters is so-called Tokamak, realized for the first time by L. Artsimovich in 1952. The name comes from the Russian acronym TOroidalnaya KAmera MAgnitnymi Katushkami, toroidal chamber with magnetic coils. The Tokamak is a toroidal system which confines the plasma by a magnetic field [1]. The dominant magnetic field component is the toroidal one, B_ζ, produced by external coils. However, this field alone does not allow the confinement of the plasma and an additional poloidal magnetic field B_ϑ is necessary for an equilibrium which has the plasma forces balanced by the magnetic forces. This additional magnetic field is produced by a large toroidal current in the plasma and by outer poloidal field coils, figure (1.2). The combination of the toroidal and the poloidal fields results in magnetic field lines with helical trajectories around the torus lying on so called magnetic surfaces. That way, the hot charged particles are confined and cannot travel in the radial direction. An external energy source generates initial current in the primary winding of the transformer (1.2). Lot of additional magnetic coils help to variate shape of the plasma and to control its behavior during tokamak operation.

At the beginning of the discharge, the plasma is heated by ohmic dissipation of the plasma current. This heat is not enough for the typical fusion parameters described. Thus, additional heating, such as the injection of high energy neutral beams or launching electromagnetic waves into the plasma, are applied in fusion experiments [1]. Once ignited, the nuclear reaction in the plasma would be completely self-heating through the fusion-born α-particles.

Unfortunately, different types of instabilities appear in the plasma. They strongly reduce plasma parameters and may even lead to disruption (dramatical event in which plasma confinement is suddenly destroyed). The investigation of the instabilities is, therefore, of crucial importance and they make the subject of this thesis.

1.2 Transport in plasma

One of the main problems in fusion research is to understand the mechanisms that govern heat and particle transport in the direction perpendicular to the magnetic surfaces. It is thought that plasma is prone to instabilities, which causes the particle and the energy to escape from the core of the plasma, damaging in this way the plasma confinement. During the last years, as larger tokamaks were built, improvement in confinement was achieved. Building larger tokamaks has also a very important economical implication. Like fission, the cost optimum is achieved by "big units" also in case of fusion (energy fission $\geq$ 1.2 GWe). To demonstrate the feasibility of fusion would be easier by "small device" (like the first fission reactors).

1.2.1 Confinement and ignition

The goals of fusion research include:

- To achieve the required temperature to ignite the fusion plasma.
- To confine the plasma at this temperature long enough to obtain useful amount of energy out of the thermonuclear fusion reactions.
- To obtain more energy from the thermonuclear reaction than is used to heat the plasma to the ignition temperature.

These goals are not trivial. The only reasonable "container" for a plasma at 10 million K is a magnetic field.
The thermal energy stored in a plasma (see [1]) is

$$W = \frac{3}{2}\int_V (n_e T_e + n_i T_i) dV,$$

where the labels refer to electrons and ions, n_j and T_j represent the particle density and temperature, respectively. We denote temperatures in terms of the average kinetic energy of random motion per particle, expressed in units of energy. So one million degree Kelvin corresponds roughly to $k_B T = 100$ eV or an average energy of one hundred electron volts. Here, $k_B = 1.38 \times 10^{-16}$ ergs per degree Kelvin, or equivalently one electron volt per about 11.600 degree Kelvin. In plasma physics one normally expresses the temperature in eV with the Boltzmann constant k_B understood. In the steady state, the energy losses P_{out} are equal to the input power P_{in}, supplied by different heating mechanisms. A measure of the thermal

isolation capability of a plasma can be described by its confinement time τ_E, which corresponds to the heat recycling rate

$$\tau_e = \frac{W}{P_{out}},$$

The reaction rate $\Re$, is proportional to the square of plasma density , $\Re \propto n_{DT}^2$, where $n_{DT} = n_D + n_T$, with n_D and n_T being the deuterium and tritium density, respectively. For a given ion density, a maximum rate is achieved for $n_D = n_T$. For the quasineutral plasma (i.e no ash and no impurities) $n_e = n_{DT}$.

The so-called triple product $n_e T_i \tau_E$ is a very important for the fusion efficiency: the ignition is reached, as shown in [1], when the following relation is fulfilled:

$$n_e T_i \tau_E > 3 \times 10^{21} m^{-3}\ keV\ s.$$

1.2.2 Particle orbits

Before we can discuss different transport mechanisms we must first look at the particle orbits in a tokamak reactor. A tokamak is a device for magnetic confinement of plasma. The principle is simple: charged particles in a uniform magnetic field gyrate around the magnetic field direction with a fixed radius, called Larmor radius and given by

$$\rho_j = \sqrt{\frac{T_j}{m_j \omega_{cj}^2}} \tag{1.1}$$

where $\omega_{cj} = q_j B / m_j$ is the gyration frequency of the particle species j in presence of a magnetic field B; q_j is the particle electric charge and m_j its relativistic mass. If $\rho_j \ll a$ particles are confined. The direction of the gyration is always such that the magnetic field generated by the charged particle is opposite to the externally imposed field. The plasma particles tend to reduce the magnetic field and plasmas are *diamagnetic*. The trajectory of a charged particle is, in general, a helix. The particles can only leave the plasma through Coulomb collisions (classic and neoclassic transport) or through fluctuating electromagnetic fields.

Particle drifts

In a laboratory plasma the electric and magnetic field strengths are actually inhomogeneous. In addition the magnetic field lines are not straight. Both the curvature radius as well as the gradient length, L_B, are of the order of the major radius R and therefore much larger than ρ_j. Every force acting in the plasma is associated

with a particle drift. We try to give a simple physical picture of the drift associated with ∇B. For simplicity, we assume that $\mathbf{B} = B\hat{z}$. Here the magnetic field lines are straight, but their density increases in y direction, B=B(y).

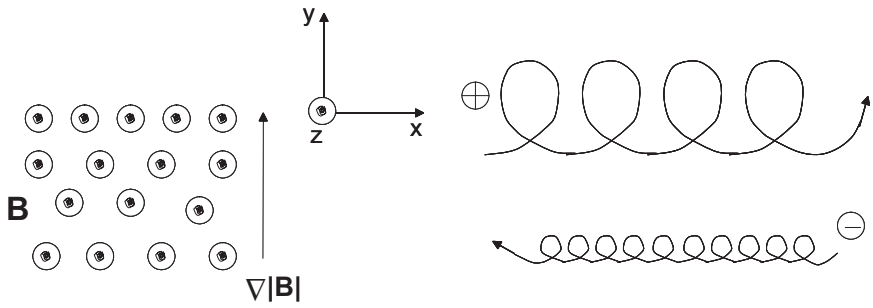

Figure 1.3: The drift of a gyrating particle in a nonuniform magnetic field

The gradient in $|B|$ causes the Larmour radius to be larger at the bottom of the orbit than at the top, and this should lead to a drift, in opposite directions for ions and electrons, perpendicular to, both, $\mathbf{B}$ and $\nabla\mathbf{B}$. Fig. 1.3 shows, the "center" of the gyration (the guide center) drifts from the ideal field-line following trajectory. The drift is in opposite directions for ions and electrons because the gyration motion around B is anticlockwise for ions and clockwise for electrons. This drift causes a current transverse to B.

Particle trapping

Another important effect of the magnetic field inhomogeneity is particle trapping. In this section we make use of the conservation of the kinetic energy (E = $mv^2/2$) and of the magnetic moment ($\mu = mv_\perp^2/2B$), which is an adiabatic invariant. The magnetic field strength in a tokamak has the form $B = B_0R_0/R$, figure (1.4), so that it increases towards the tokamak axis. Since the field line is twisted around a toroidal surface, as a particle moves from a weak field region to a strong field region in course of its thermal motion, it sees an increasing B, and therefore its $v_\perp$ must increases in order to keep μ constant. Since the total energy must remain constant, $v_{||}$ must necessarily decrease. If B reaches a critical value, B_{ref}, $v_{||}$ eventually becomes zero and, the particle is "reflected" back in the weak field region. This is known as "mirror effect". The trapping condition reads

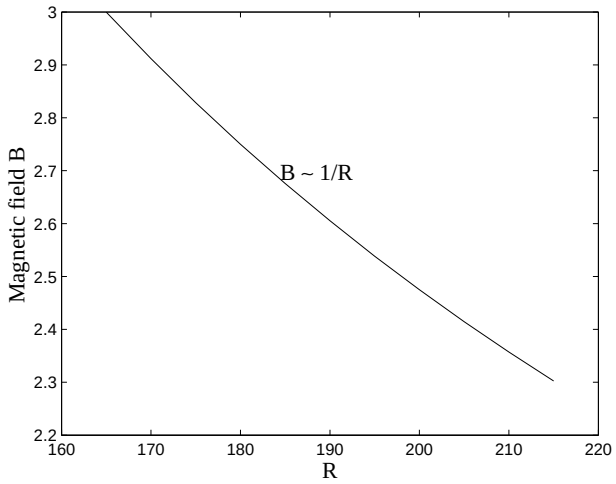

Figure 1.4: The magnetic field strength behaviour in a tokamak. The magnetic field decreases from the center to the plasma edge.

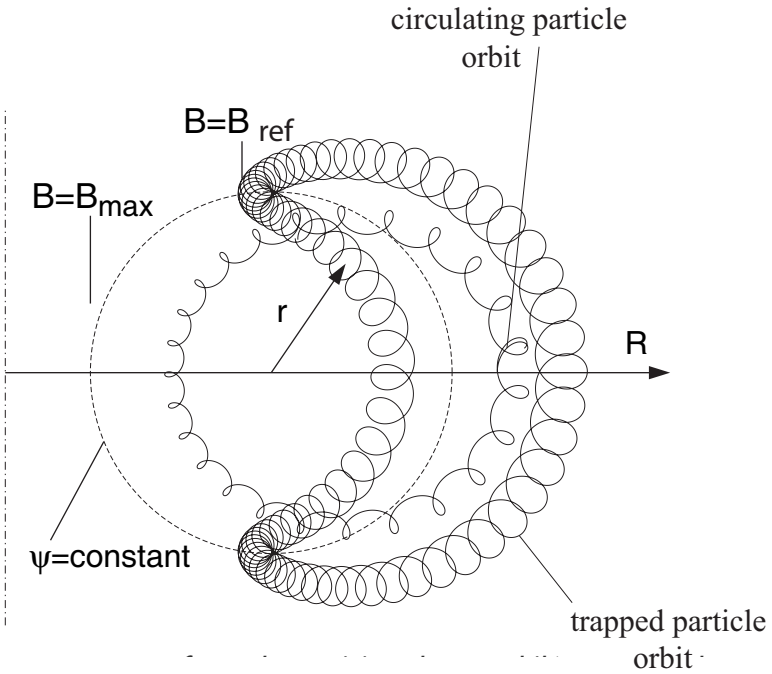

Figure 1.5: Particles orbits.

$$\frac{1}{2}mv_{||0}^2 < \mu B_{max} - \mu B_{min},$$

where B_{max} is the maximum field seen by a passing particle and $v_{||0}$ is the parallel velocity at the place where $B = B_{min}$. For an isotropic distribution function, in a tokamak we have:

$$\frac{v_{||0}^2}{v_0^2 - v_{||0}} = \frac{v_{||0}^2}{v_\perp^2} < \frac{B_{max} - B_{min}}{B_{min}} \approx \frac{2r}{R_0 - r} = \frac{2\epsilon}{1-\epsilon}$$

where $\varepsilon = r/Ro$ is the local inverse aspect ratio of the tokamak at the radial position r. The trapped particles fraction is

$$f = \frac{n_t}{n} \approx arcsin(\frac{v_{||0}}{v_0})_{limit} \approx \frac{v_{||0}}{v_0}|_{limit} \approx \sqrt{\frac{2\epsilon}{1+\epsilon}}.$$

The projection of a trapped particle orbit on the poloidal plane of an axisymmetric torus is sketched in figure (1.5). The flux surfaces are assumed to have circular cross-sections. If particle drifts were not present, the orbit would be aligned to the field line and would have zero width. But since B increases towards the torus axis, both species drift in the vertical direction. Trapped particles may encircle the torus in the toroidal direction but be poloidally confined to the low field side of the torus.

The width of the trapped particle orbit can easily be calculated

$$\Delta r = 2\frac{v_{||m}}{eB_{p,m}/c\,m} \tag{1.2}$$

where r is the cylindrical radius and $v_{||m}$ is the value of the parallel velocity at the midplane. Note that the denominator is the gyro-frequency in the poloidal field at the mid-plane $B_{p,m}$.

1.2.3 Anomalous transport

As has been already said, the effect of the magnetic field is to turn the particle motion perpendicular to the field into small circular orbits. Typically the orbit of the plasma ions has a radius of a few millimeters. This means that the particles perform very many orbits, a deuteron ion completing about 30 orbits per microsecond. The electrons, being faster and less massive, move in an orbit 60 times smaller at 3672 times the ions gyrofrequency. The particles move freely parallel to the magnetic field, but this takes them along surfaces which are closed within the tokamak.

The question naturally arises to what limits confinement in the magnetic field of a tokamak. Why would particles not gyrate about a field line forever? The

first answer is that the particles collide with each other and the collisions cause a displacement of the orbit. These displacements are random and so the particles diffuse across the magnetic field until they reach the edge of the plasma. Collisions also lead to a diffusive transfer of heat, as in a gas, the hotter particles passing energy to their cooler neighbors.

Heat transport coefficient of the species j can be introduced without loss of generality

$$\chi_j = -\frac{q_j}{n_j|\nabla T_j|},$$

where q_j is the absolute value of the heat flux $\mathbf{q}_j$, i. e. the amount of energy flowing through a magnetic surface in the unit time per unit surface. The relation between the confinement time and the heat transport coefficient is simply

$$\tau_{Ej} \propto \frac{n_j T_j V}{q_j S} \propto \frac{n_j \nabla T_j a V}{n_j \chi_j \nabla T_j S} \propto \frac{a^2}{\chi_j},$$

where a is the minor radius of the tokamak. Therefore, χ_j provides a measure of the effective perpendicular heat transport, regardless of its physical meaning and of the mechanism governing transport.

Although calculation of the collisional diffusion is complicated, the simple account given above implies a straightforward process of particle and energy loss. However, it is not like that. From the earliest days of fusion research, it was recognized that experimental plasmas were not governed by the rules of collisional transport. The loss rates are higher than calculated, and a large part of the experimental effort on tokamak has been devoted to trying to understand this behaviour.

In tokamak experiments is found that the transport coefficients are much larger than predicted by collisional transport theory. Having unexpected properties the transport of heat and particles in tokamaks is called "anomalous". With high temperatures and strong magnetic fields, it was expected that the losses of particles and heat energy would be low enough, so that fusion would be demonstrated as soon as the equilibrium problem was solved. The ion thermal transport is typically a few times the collisional value, the precise ratio depending on the conditions. For electrons, the energy confinement time decreases dramatically, while ion transport is less affected. The electron thermal transport is much more anomalous but, because the electron collisional transport is very small, the outcome is that experimentally the two types of thermal transport are comparable in magnitude. Scaling laws have been extracted from the experimental databases of different tokamaks [2] but their understanding in terms of physics is still being investigated.

The obvious explanation of this anomalous behaviour, in general terms, is that the plasma is subject to instability. It turns out that plasmas are not quiescent at all, but are always quivering with "fluctuations" in all their parameters: density, temperature and even the magnetic field. All these parameters have disturbances about their mean values, and the disturbances are of the incoherent type of motion called "turbulence" if it is associated with waves or fluid-like flows. Additionally, the electric field is never exactly zero, as might have been expected in an electrically neutral plasma (average charge density zero), but participates as well in the fluctuations. This is important since it gives rise to a fluid-like motion called the "ExB drift". This is a drift of the plasma across magnetic field lines. Fluctuations in the magnetic field could also give rise to transport since particles are not constrained against motion along magnetic field lines (when the magnetic field fluctuates, all three components are involved). Turbulent transport could be "electrostatic" if due to ExB turbulence or "electromagnetic" if due to magnetic fluctuations. At this moment both possibilities are open.

Since transport in confined plasmas is not yet fully understood, and it strongly affects how well fusion devices perform, it is among the most important outstanding problems in plasma physics. It is important to note as well that this is a physics problem, in contrast to all other likely sources of energy, for which the problems are of a technical or engineering nature.

1.2.4 Microinstabilities

A plasma instability involves plasma waves that grow exponentially. For proper description of a particular instability, one should be able to define the mode of the growing wave, the nature of the growth source of the free energy.

Because of all these points of view, the nomenclature for plasma instabilities is even more cumbersome than for the wave modes themselves. A solid understanding of plasma theories is needed in order to study the formation of different instabilities. One important way to classify different instabilities is to divide them into macroinstabilities and microinstabilities.

A macroinstability is driven by the structure of the medium in configuration space. A familiar example of a macroinstability is for a convectively unstable system: when the temperature gradient is super-adiabatic, internal gravity waves grow to large amplitude and cause a large-scale convection of the fluid, which tends to reduce the temperature gradient. Other familiar examples are the Rayleigh-Jeans

instability, in which a denser fluid is supported by a less dense fluid, and the Kelvin-Helmholtz instability, in which one fluid flows over another fluid, e.g., wind over water, causing surface waves to grow. In plasmas the macroinstabilities occur in the low-frequency regime and usually involve the magnetic field. Examples include flute (or interchange) and ballooning instabilities. The latter ones are used, for example, in some substorm models.

Microinstabilities, on the other hand, are usually driven by temperature and density gradients. A consequence of a microinstability is a greatly enhanced level of fluctuations in the plasma associated with the unstable mode. These fluctuations are called microturbulences. Microturbulences can lead to an enhanced radiation from the plasma and to enhanced scattering of particles resulting in 'anomalous' transport coefficients, e.g., anomalous electric and thermal conductivities.

Before stability analysis is performed on any plasma, sources of free energy must be identified. If there are sources of free energy, potential for instabilities exists. In the tokamak, there are density and temperature gradients perpendicular to the magnetic field. These gradients are sources of free energy which may drive drift type modes. Microinstabilities may be driven by these sources of free energy.

Drift wave instabilities occur in low-frequency collective oscillations in which the electric field, with a substantial perpendicular component and a small parallel component arises, from the large scale charged particle interactions. The oscillation frequencies are low compared to the ion gyrofrequency ω_{ci} (the gyrofrequency has been introduced before in 1.2.2). A drift wave is a mode with frequency of the order of the diamagnetic frequency $\omega \approx \omega_\star = k_\perp \rho_s c_s / L_n$, with $k_\perp$ the perpendicular wave vector, ρ_s electron Larmour radius, c_s electron thermal speed and L_n the density gradient length. Because of their different masses, electrons and ions respond differently to the electromagnetic field perturbation and therefore play different roles in the evaluation of microinstabilities. Typically, one species will provide the drive, while the other provide the damping. Dissipation often plays a crucial role in causing instabilities; this can be either collisional as in a low temperature plasma, or due to a Landau resonance when the collisional frequency is low. The resulting instabilities are called *dissipative*. Some of the microinstabilities are *reactive* and do not require dissipation. The ion temperature gradient mode (ITG), is an example of this type.

There is agreement that the main candidate to explain ion transport is the Ion Temperature Gradient (ITG) driven turbulence, possibly coupled to the Trapped Electron Mode (TEM). The stabilizing contribution of the sheared plasma rotation $\omega_{E\times B}$ [5] is also commonly accepted. A physical picture of the toroidal ITG and

TEM instabilities mechanism is given in section 2.4. However, different models based on the same basic modes yield different predictions, depending on the closure of the set of equations, on the stabilizing and destabilizing terms included and on the approximations made. For electron transport until a few years ago most of the modelling attempts relied on empirical and semi-empirical models.

1.3 Ray tracing and eigenmodes

In order to study the wave phenomena in the short wavelength limit, different asymptotic approaches have been used. One of the most famous technique is the WKB method. The short wavelength domain is of interest for tokamak plasma. In this limit, the waves behave as particles so that one can use the geometrical optics to study them. In this thesis, a modification of the WKB approach is introduced, the beam tracing method (BT).

Actually, in spite of all the essential differences between the various asymptotic approaches that exist, the leading order of any of them results in the description of the ray tracing technique. So that discussing the BT method, or any other short wavelength asymptotic method, is appropriate to discuss first the ray tracing.

A simple problem is proposed to be solved: one has to find the eigenfunctions of the elliptic membrane.

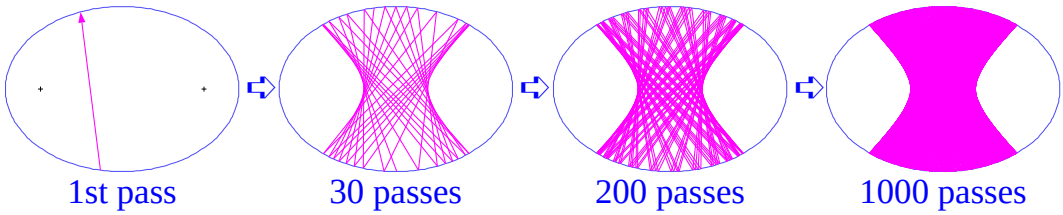

Figure 1.6: The behaviour of one ray launched in a resonator.

Independent on the type of the excitation, the field amplitude distribution inside the resonator will characterize the eigenmode structure. It can assumed that the wavelength is so small that the one can use the ray representation for the propagating waves. For this purpose one experiment is thought: a wave (a ray) is launched in the resonator and its behaviour is traced, figure (1.6). A concentration of rays in some region inside the resonator indicates that a localized eigenmode can be found in this region. In turn, it is intuitively clear that the rays are localized around a closed ray trajectory. This will be a limit cycle for any ray family representing the

eigenmode and it will be called the basic contour. Then, a localized eigenfunction can be found in the vicinity of a closed ray.

In [6] has been shown that subsequences of eigenfunction do exist in the neighborhood of a closed ray trajectory. The eigenfunctions are concentrated in the vicinity of a closed ray, and exponentially decay with the increasing distance from the ray (see the end of this section).

Not any arbitrary ray trajectory can generate an eigenfunction. Only stable closed trajectories give rise to an eigenmode. One has to distinguish between the stability of an eigenmode and the stability of a closed trajectory. The stability of an eigenmode describes how the mode is decreasing or increasing in time. When the stability of a closed trajectory is discussed, this means that: after a long enough pass in the medium, the rays that are initially closed to this trajectory are still located in the small neighborhood. This is illustrated by figure (1.7) right-hand side. No regular structure can be expected if the mode is unstable, figure (1.7) left-hand side.

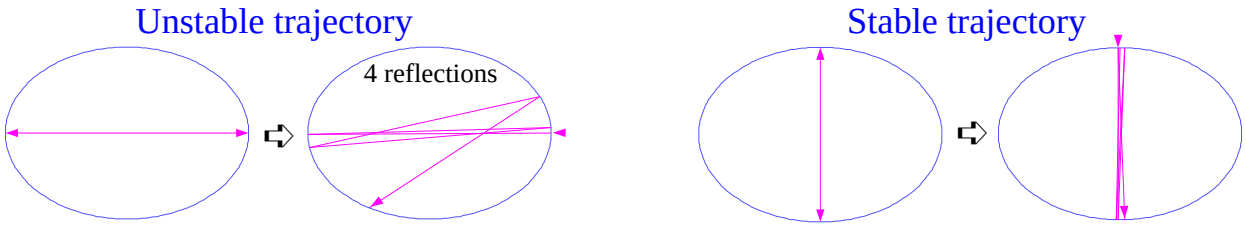

Figure 1.7: Unstable trajectory and stable stable trajectory of the bouncy type.

After a closed ray trajectory is found, the conventional quantization condition for the eikonal should be applied. This provides a set of wave numbers and eigenfrequencies associated with the trajectory, but they do not say anything abound the stability of the found trajectory and, therefore, about the realization of the eigenmodes. In frames of the ray approach, one should further investigate the stability of the ray traces around the basic contour.

In fusion plasmas, even when the condition $\lambda \ll L$ is fulfilled with large margin, the ray tracing could fail very often. The reason for this failure is that this inequality provides only the necessary, but not sufficient, condition for applicability of ray tracing. A breakdown of the applicability condition means that diffraction phenomena which are not taken into account by the ray tracing, become significant.

The sufficient condition of applicability is known as Fresnel condition and in addition to $\lambda \ll L$, it imposes a limitation on width of the beam Λ. In inhomogeneous media, diffraction effects are significant for $\Lambda \approx \sqrt{\lambda L}$.

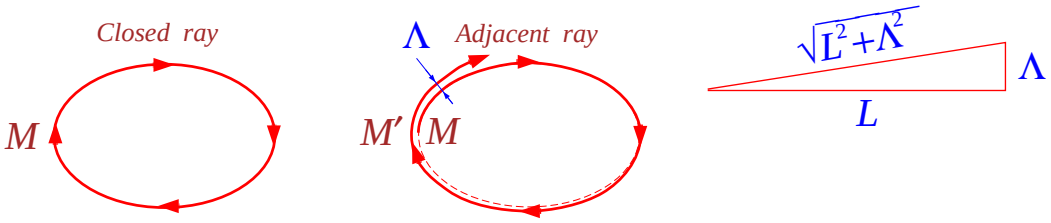

Figure 1.8: The width of the mode.

In order to evaluate the eigenmodes width consider a closed ray trajectory as shown in figure (1.8) (left). Here the ray starting from the point M arrives at the same point. An adjacent ray starting in the point M, after one loop, arrives into the point M'. As known from the Huygens-Fresnel principle, the diffraction becomes important if the phase difference between the two points reaches π, or in terms of the trajectory length, $\lambda/2$. The length difference between the two trajectories can be evaluated as shown in figure (1.8) (right). We write $\sqrt{L^2+\Lambda^2} - L \approx \Lambda^2/2L = \lambda/2$ and find that the mode widths amounts to $\Lambda \approx \sqrt{\lambda L} \ll L$. The mode widths depends on the real frequency ω and on the wavelength (the smaller is the wavelength the narrower is the wave beam). So that:

• the phase information is essential,

• eigenmodes can be represented as narrow wave beams.

Both this requirements are contained in the BT technique. This method treats the entire wave packets of the finite width and retains a description of the wave phenomena. The full description of the BT method, including the full set of equations used by this method, is given in Chapter 4.

1.4 Motivation and Outline

Understanding the anomalous transport in tokamaks is nowadays a primary challenge in fusion plasma research. In this thesis, in order to study the microturbulences, which are considered to be the main cause of anomalous transport, a new numerical code is developed. In the same time comparison with the existing ones is done. The thesis is structured as follows:

Chapter 2 introduces the drift-waves. A simple description of the physics of microinstabilities, focusing on the ion temperature gradient mode, trapped electron mode and electron temperature gradient mode, is also provided. This chapter intends to provide the physical insight needed to understand the microturbulence.

Chapter 3 presents the results of the simulation done for the standard L-mode discharges. The gyrokinetic GS2 code is used in the simulations. The trapped electron mode is found to be dominant for the considered set of parameters. The results of the simulations are compared with the experiment. Comparison with two other well known models, Weiland and GLF23 models, is also done. Good agreement between GS2 and GLF23 models is found.

In **Chapter 4**, the BT method is applied for solving the stability problem in multi-dimensionally inhomogeneous plasmas. In this method, eigenfunctions are constructed as wave patterns located in the vicinity of closed ray trajectories.

The approach is applied to the analysis of ion temperature gradient instability in a tokamak. The eigenmode can be thought of as a wave propagating in the toroidal direction. The eigenmode axis is purely toroidal while the mode amplitude exponentially decays both in radial and poloidal directions. Finally, wave interaction with a plasma defines whether such a mode absorbs or releases energy.

The paraxial WKB method can describe drift-ballooning instabilities in the presence of sheared plasma rotation when the ballooning representation usually used for this problem fails. Unlike the ballooning representations, the pWKB technique allows for a radial dependence of the wave field $k_\rho \neq 0$, it can be easily extended to arbitrary geometry and three-dimensional systems, such as stellarators. On the other hand, the two approaches are closely related because both use the same small parameter $(\lambda/L)^{-1/2}$. In some aspects, the pWKB is more restrictive than the ballooning representation, therefore, the two techniques should be viewed as complimentary.

In **Chapter 5** the solution of the equations that describe the ITG turbulence is presented. By using the pWKB method the set of equations that describe the ITG mode is reduced to a set of algebraic equations easy to be solved by numerically treatment. In the first step, the dependence of the growth rate of the ITG mode is compared with Guo and Weiland model. Results from the full set of BT equations are also shown. The BT model can be easily extended to arbitrary geometry so that dependence on the Shafranov shift and on the elongation can be studied. Dependence on the magnetic shear is also studied.
Finally, the results are summarized and their impact on transport research is discussed.

Chapter 2

Drift waves in plasma

2.1 Introduction

Work for understanding transport in magnetic confined systems has been going on for about 50 years. Despite this the transport problem is still a major scientific issue. Its importance for the costs and size of the reactor its obvious and critical, but the scientific difficulties associated with it are huge.

Low frequency modes with frequency, ω, much smaller than the ion cyclotron frequency ω_{ci} are considered to be the most dangerous ones for the establishment of quasi-stationary high beta-plasma states, necessary for the realization of the thermonuclear fusion. The main common feature of these modes is that they have $k_{||} \ll k_{\perp}$. This means that these modes have a very slow variation along the magnetic field and may be denoted as quasi-flute modes. In this section we are going to concentrate our attention exactly on these modes, trying to emphasize the physics behind different kind of waves which can appear in plasma.

In studying plasma different models were used in order to get a good description of the phenomena noticed in it. The transport phenomena observed in real experiments can be explained using the fluid model, in which the identity of the individual particle is neglected and only the motion of fluid element is taken into account. In the case of plasma, of course, the fluid contains electrical charge. In an ordinary fluid, frequent collisions between particles keep the particle in a fluid element moving together. It is surprising that such a model works for plasmas, which generally have infrequent collisions. The fluid description of plasma is so far the simplest description of the plasma and is indeed fortunate that this approximation is sufficiently accurate to describe the majority of observed phenomena. A more refined treatment - the kinetic theory of plasma - requires more mathematical treatment.

2.2 Equilibrium

Before introducing the different descriptions of plasma is useful to present the tokamak equilibrium and the employed coordinate system.
The basic condition of equilibria in a tokamak is that the force on the plasma be zero at all points. This requires that the magnetic force balances the force due to the plasma pressure

$$\vec{j} \times \vec{B} = \nabla p \tag{2.1}$$

$$\nabla \times \vec{B} = \mu_0 \vec{j} \tag{2.2}$$

$$\nabla \cdot \vec{B} = 0 \tag{2.3}$$

It is clear from equation (2.1) that $\vec{B} \cdot \nabla p = 0$, i.e. there is no pressure gradient along the magnetic field lines and the magnetic surfaces are surfaces of constant pressure. Furthermore, $\vec{j} \cdot \nabla p = 0$ and consequently the current lines also lie in the magnetic surface.

To describe the toroidal magnetic configuration is convenient to use coordinates defined by the field itself. The advantages gained by using a coordinate system which is defined by, and is natural for, the description of the magnetic field outweigh those gained by using a standard orthonormal system. The coordinates are taken to be toroidal in form, because of the necessarily toroidal topology of the magnetic field surface.

The general coordinates (ψ, ϑ, ζ) are introduced, as shown in figure (2.1). Surfaces of constant ψ are taken to consist topologically of nested axisymmetric tori, which necessarily posses one axis designed usually by $\psi = 0$. Surfaces of constant ϑ define a general poloidal angle and finally ζ defines the "toroidal" direction. The surface labeled with ψ is taken to be increasing outward and thus the system (ψ, ϑ, ζ) defines a right hand coordinate system.

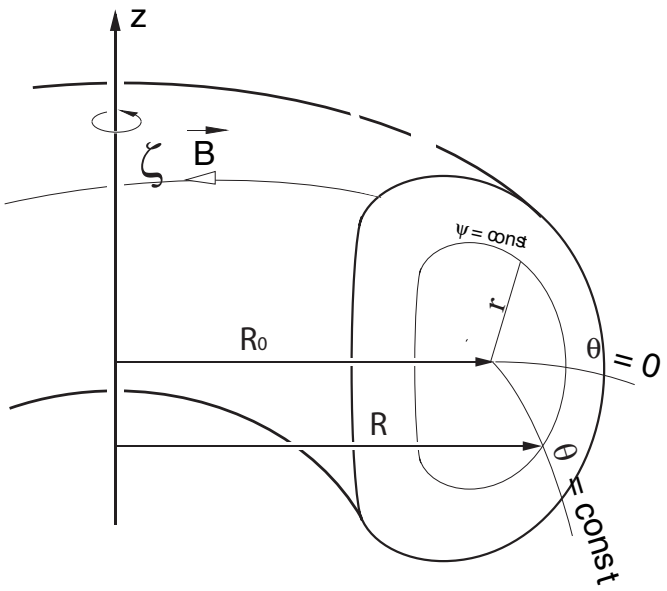

Figure 2.1: Toroidal geometry

For a given surface, the minor radius is r and the major radius is R_0. While R_0 is constant, r is a surface label and therefore useful as a coordinate. The other two coordinates being again ϑ and ζ, which are cyclic on the interval $[0, 2\pi]$. The surface which has $r = 0$ is called the magnetic axis, and the reference surface at which the turbulence is to be evaluated is $r = a$, with "a" constant.

The equilibrium quantities are assumed to be functions of r only. The exception is the magnetic field, whose flux is a function of r only but whose strength varies inversely with R. The most general divergence axially symmetric free magnetic field that confines the plasma has the form

$$\vec{B} = I\nabla\zeta + \nabla\psi \times \nabla\zeta,$$

with $I = R_0 B_0$, B_0 represents the magnetic field at the mid-plane, $R = R_0$.

The magnetic flux ψ is a function of the minor radius a, so that one can write $\nabla\psi = (d\psi/da)\nabla a$ and the magnetic field is then written

$$\vec{B} = I(\nabla\zeta + \Theta\nabla a \times \nabla\zeta), \;\; B = \frac{I}{R}\sqrt{1 + g^{aa}\Theta^2}$$

where $\Theta(a) = a/(2R_0 q_s)\,[\lambda(a) + (a\lambda)']$. When $\Delta(a) = 0$, $\delta(a) = 0$ and $\lambda(a) = 1.0$ we obtain a circular geometry of the magnetic surfaces. The parameter $q_s(a)$ is an

arbitrary safety factor defined as

$$q(a) = \frac{\Delta\zeta}{\Delta\vartheta} = \frac{B_\zeta}{B_\vartheta}\frac{r}{R}, \tag{2.4}$$

where $\Delta\vartheta$ and $\Delta\zeta$ are changes in ϑ and ζ on a translation along a field line. B_ζ and B_ϑ are the toroidal and poloidal components of the magnetic field. They satisfy the relation $B_\vartheta \ll B_\zeta$.

The wave vector is given by

$$\vec{k} = k_a \nabla a + k_\vartheta \nabla\vartheta + k_\zeta \nabla\zeta$$

where ∇a, $\nabla\vartheta$, $\nabla\zeta$ are the reciprocal basis vectors, given in the appendix B, and k_a, k_ϑ, k_ζ are the covariant components of the wave vector. In literature, the covariant component of the poloidal wave number is found as $k_\vartheta = m$ and of the toroidal wave number $k_\zeta = n$. Physical significance has $k_\theta = m/a$. The components of $\vec{k}$ parallel and perpendicular to the magnetic field are approximated by

$$\begin{aligned} k_{||} &= \frac{\vec{k}\cdot\vec{B}}{B} = \frac{k_\zeta}{R} - \frac{k_\vartheta\Theta}{ad} \approx \left[m - nq_s\right]/Rq_s, \\ k^2 &= k_a^2 g^{aa} + k_\vartheta^2 g^{\vartheta\vartheta} + 2k_a k_\vartheta g^{a\vartheta} + k_\zeta^2 g^{\zeta\zeta}, \end{aligned} \tag{2.5}$$

where g^{aa}, $g^{a\vartheta}$, $g^{\vartheta\vartheta}$, $g^{\zeta\zeta}$ and d in the general geometry are given in appendix B.

Another quantity of interest in the tokamak plasma is the magnetic shear, introduced as

$$\hat{s} = \frac{dlnq}{dlnr} = \frac{r}{q}\frac{dq}{dr}. \tag{2.6}$$

For a tokamak, $\hat{s}$ is typically small near the axis and is otherwise of order 1.

2.3 Fluid description of plasma

The most convenient and simple way to study tokamak plasma is the fluid approach. This method allows in particular to define measurable quantities for the heat transport analysis and diagnose the energy confinement capability of a plasma. The fluid equations are given by the moments of the Boltzmann equation

$$\frac{\partial f}{\partial t} + \mathbf{v}'\cdot\nabla f + \frac{\vec{F}}{m}\cdot\frac{\partial f}{\partial v} = (\frac{\partial f}{\partial t})_c, \tag{2.7}$$

where $f(\vec{r}, \mathbf{v}', t)$ is the distribution function, $\vec{F}$ is the force acting on particles, the symbol $\mathbf{v}'$ being now used to distinguish the particle velocity from fluid velocity $\vec{v}$, $(\partial f/\partial t)_c$ is the time change of f due to collisions. In a sufficiently hot plasma, Coulomb collisions can be neglected. If the force is entirely electromagnetic, equation (2.7) takes the special form

$$\frac{\partial f}{\partial t} + \mathbf{v}' \cdot \nabla f + \frac{q}{m}(\vec{E} + \vec{v} \times \vec{B}) \cdot \frac{\partial f}{\partial v} = (\frac{\partial f}{\partial t})_c \tag{2.8}$$

and in this case is called the Vlasov equation. $\vec{E}$ and $\vec{B}$ are self-consistent fields, defined by the plasma particles. The equation (2.7) is multiplied by chosen functions $\phi(\mathbf{v}')$ and integrated over the velocity space to obtain equations for

- Density: $\mathrm{n} = \int f(\vec{r}, \mathbf{v}', t) d\mathbf{v}'$
- Velocity: $\vec{v} = \frac{1}{n} \int f(\vec{r}, \mathbf{v}', t) \mathbf{v}' d\mathbf{v}'$
- The pressure tensor: $\mathrm{P} = \mathrm{m} \int f(\vec{r}, \mathbf{v}', t)(\mathbf{v}' - \mathbf{v})(\mathbf{v}' - \mathbf{v}) d\mathbf{v}'$

2.3.1 Continuity and Momentum Equations

The electron and ion fluid equations in a collisional plasma, i.e. the continuity equation, motion and heat balance are called the *Braginskii equations*, since they were first obtained in the celebrated article by S. Braginskii.
The continuity equation is obtained by integrating equation (2.7). One gets

$$\frac{\partial n_j}{\partial t} + \nabla \cdot (n_j \vec{v}_j) = 0, \;\; j = i, e. \tag{2.9}$$

The equation expresses the density change at a stationary point as a divergence of the particle flux $\vec{\Gamma}_j = n_j \vec{v}_j$. There is no collision term considered, since Coulomb collisions do not change the number of particles.

The momentum balance equation is obtained by multiplying equation (2.7) by $\mathrm{m}\vec{v}$ and integrating over $d\vec{v}$. In this way we obtain the equation of motion which describes the flow of momentum. Taking $\vec{F}$ to be the Lorentz force, for each species, we have an equation of motion

$$m_j n_j \frac{d\vec{v}_j}{dt} = m_j n_j \left[\frac{\partial \vec{v}_j}{\partial t} + (\vec{v}_j \cdot \nabla)\vec{v}_j \right] = n_j q_j (\vec{E} + \vec{v}_j \times \vec{B}) - \nabla p_j - \nabla \cdot \pi_j + R_j. \tag{2.10}$$

Here, the isotropic pressure $p_j = n_j T_j$ and the anisotropic stress tensor π_j were introduced, n_j and T_j are the density and the temperature of the ions or electrons,

m_j and q_i represent the electron or ion mass and charge, R_j is the rate of momentum transfer due to collisions.

Assuming an electrostatic approximation, $\vec{E} = -\nabla\phi$, we obtain taking the vectorial product of equation (2.10) with $\vec{e}_{||}/m_j n_j$

$$\frac{d}{dt}\vec{e}_{||} \times \vec{v}_j = \frac{q_j}{m_j}\left\{\vec{e}_{||} \times \vec{E} + B\left[\vec{v}_j - \vec{e}_{||}(\vec{e}_{||} \cdot \vec{v}_j)\right]\right\} - \frac{1}{m_j n_j}\vec{e}_{||} \times (\nabla p_j + \nabla \cdot \pi_j) \quad (2.11)$$

with $d/dt = \partial/\partial t + \vec{v}_j \cdot \nabla$, and $\vec{e}_{||} = \vec{B}/B$.

Since $\vec{v}_j - \vec{e}_{||}(\vec{e}_{||} \cdot \vec{v}_j)$ is $\vec{v}_{\perp j}$ we find

$$\vec{v}_{\perp j} = \frac{1}{B}(\vec{E} \times \vec{e}_{||}) + \frac{1}{\omega_{cj}}\frac{d}{dt}(\vec{e}_{||} \times \vec{v}_j) + \frac{1}{q_j n_j B}\vec{e}_{||} \times (\nabla p_j + \nabla \cdot \pi_j) \quad (2.12)$$

The parallel velocity is obtained by considering the scalar product of $\vec{e}_{||}$ with the equation (2.10)

$$\frac{\partial v_{||j}}{\partial t} + \vec{e}_{||} \cdot (\vec{v}_j \cdot \nabla)\vec{v}_j = \frac{q_j}{m_j}\vec{e}_{||} \cdot \vec{E} - \frac{1}{m_j n_j}\vec{e}_{||} \cdot \nabla p_j = -\frac{q_j}{m_j}\vec{e}_{||} \cdot \nabla\phi - \frac{1}{m_j n_j}\vec{e}_{||} \cdot \nabla p_j \quad (2.13)$$

The linearized and Fourier transformed equation is

$$v_{||j} = -\frac{i}{\omega m_j}\vec{e}_{||} \cdot \nabla(q_j\phi + \frac{p_j}{n_j}) \quad (2.14)$$

In the equation (2.13) the term $\vec{e}_{||} \cdot (\vec{v}_j \cdot \nabla)\vec{v}_j$ contains only the perturbed velocity so that the linear term is zero. Using the equations (2.14) and (2.13) the total velocity is given by

$$\vec{v}_j = \vec{v}_{\perp j} + v_{||j}\vec{e}_{||} \quad (2.15)$$

2.3.2 Drifts in plasma

As will appear clear further on, important features underlying the instabilities in plasma are the various drifts that can arise in a magnetized plasma.

The perpendicular velocity in the equation (2.12) can be written as

$$\vec{v}_{\perp j} = \vec{v}_{Ej} + \vec{v}_{pj} + \vec{v}_{\star j} + \vec{v}_{\pi j} \quad (2.16)$$

In equation (2.16) the first term is the $\vec{E} \times \vec{B}$ drift. The second term is the polarization drift and contains the perturbed velocity. If the $\vec{E} \times \vec{B}$ drift is assumed

to be the dominating part of the perturbed velocity it can be substituted into the polarization drift. In equation (2.16) we have:

$$\vec{v}_E = \frac{\vec{E} \times \vec{e}_{||}}{B}, \tag{2.17}$$

$$\vec{v}_{pj} = \frac{1}{B\omega_{cj}} \left[\frac{\partial}{\partial t} \vec{E} + (\vec{v}_j \cdot \nabla)\vec{E} \right] \tag{2.18}$$

$$\vec{v}_{\star j} = -\frac{\nabla p_j \times \vec{e}_{||}}{q_j n_j B}, \tag{2.19}$$

$$\vec{v}_{\pi j} = \frac{\vec{e}_{||} \times \nabla \cdot \pi_j}{q_j n_j B} \tag{2.20}$$

The assumption $\vec{v}_{pj} \ll \vec{v}_E$ is consistent with the assumption $\omega \ll \omega_{cj}$. For this approximation to be generally valid we must have $\omega \ll \omega_{ci}$. The $\vec{E} \times \vec{B}$ drift is the same for ions and electrons. It is important to note that $\vec{v}_E$ is independent of q_j and m_j. The velocity $\vec{v}_{\star j}$ is the diamagnetic drift velocity. It is a pure fluid velocity and it is not a particle drift.

The velocity $\vec{v}_{pj}$, is the polarization drift while the velocity $\vec{v}_{\pi j}$ is due to the stress tensor π_j. The stress tensor contains a viscosity part π_v and a finite Larmor radius part π_l. The finite Larmor radius part $\vec{v}_{\pi l}$ of $\vec{v}_\pi$ fulfils $\nabla \cdot (n\vec{v}_{\pi l}) \sim k_\perp^2 \rho^2 n_0 |\nabla ln\, n_0| \vec{v}_\perp$. The contribution may be neglected if $k_\perp^2 \rho^2 \ll 1$.

2.3.3 Interpretation of the drifts

The drifts presented above are fluid drifts. They may differ from the particle or guiding center drifts and these differences are sometimes sources of confusion. The fluid velocity of a constituent species of plasma at a given point is simply the mean velocity of the particle of that species in a small volume around the point. However, the gyro-averaged velocity of the particle is the velocity of their guiding center. Generally the fluid velocity and velocity of the guiding center at a given point is not the same. Since the fluid element is composed of many individual particles, it is expected to have drifts perpendicular to $\vec{B}$ if the individual particles have such drifts. Since the ∇p_j term appears only in the fluid equation, there is a drift associated with it which the fluid elements have but the particles do not have. Therefore, we will have drifts associated with fluid and drifts associated with particles.

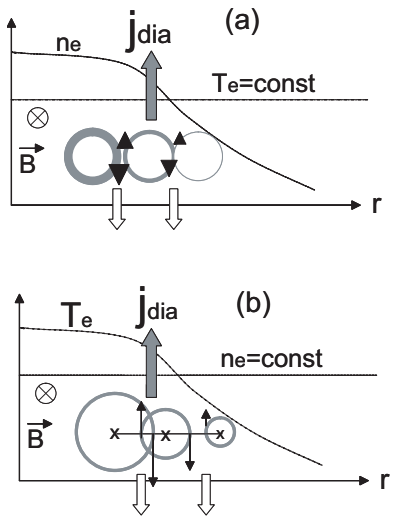

Figure 2.2: Origin of the diamagnetic drift.

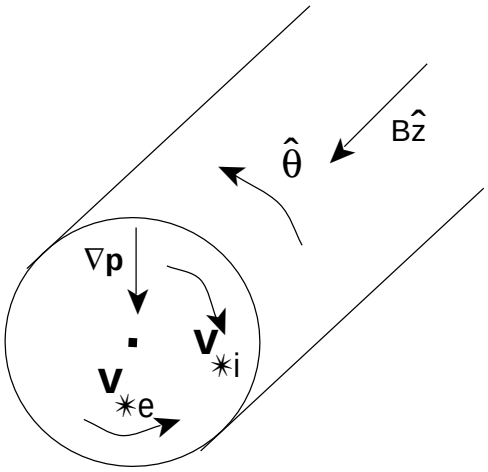

Figure 2.3: Diamagnetic drift in a cylindrical plasma.

The diamagnetic drift is due to the pressure gradient. The physical reason for this drift can be seen in figure (2.2). Here we consider electrons gyrating in a magnetic field. Two special cases are discussed: i) In figure (2.2a), there is a density gradient, the electron temperature T_e is kept constant. Through any fix volume element there are more electrons moving downward than upward, since the downward moving electrons are coming from a region with higher density. There is, therefore, a fluid drift perpendicular to density gradient and $\vec{B}$, even though the guiding centers are stationary. An upward diamagnetic current appears; ii) In the second case, figure (2.2b), the density is kept constant, so that the pressure gradient is due only to the temperature gradient. The electrons moving downwards are much faster and they have much larger gyroradius, since they are coming from regions with higher temperature. Once again, there is an upward diamagnetic current. The diamagnetic drift reverses its sign with the particle charge q_j, (see Fig. 2.3) and produces a diamagnetic current, which in turn balances the plasma pressure through the $\vec{j} \times \vec{B}$ term.

The remaining drifts (except $\vec{v}_\pi$) are the same for the fluid and particle description. Because the $\vec{v}_E$ term is the same for electrons and ions it does not give rise to a current.

The polarization drift, given by

$$\vec{v}_{pj} = \frac{\vec{e}_{||}}{\omega_{ci}} \times \frac{d\vec{v}_E}{dt},$$

reduces to equation (2.18) when the magnetic field is stationary but the electric field varies in time. This expression can be understood as a polarization drift by considering what happens if an electric field is suddenly imposed on a particle at rest. The particles initially accelerates in the direction of the electric field, but then are deflected by the magnetic force. Thereafter, particles undergo conventional gyromotion combined with the $\vec{E} \times \vec{B}$ drift. Note that, there is no deflection if the electric field is directed parallel to the magnetic field, so this argument only applies to perpendicular electric fields. The initial displacement of particles in the direction of the field is of the order of $\delta \sim \frac{eE}{m}(\Delta t)^2$, where $\Delta t \sim \omega_{ci}^{-1}$ represents the time between the switch-on of the field and the magnetic deflection. Since, because $\omega_{ci} \propto m^{-1}$, the displacement of ions greatly exceeds that of the electrons, so that the electrons polarization drift is usually neglected. Thus, when an electric field is suddenly switched on in a plasma, there is an initial polarization of the plasma medium caused, predominately, by a displacement of the ions in the direction of the field. If the electric field, in fact, varies continuously in time, then there is a slow drift due to the constantly changing polarization of the plasma medium.

The polarization drift is regarded as a correction to $\vec{E} \times \vec{B}$ drift when the $\vec{E}$-field is time dependent. There is also, a strong similarity between the polarization drift caused by the time variation of $\vec{E}$ and the finite Larmor radius drift, which is due to the space variation of $\vec{E}$, since a gyrating particle cannot decide if the variation in $\vec{E}$, which is experienced along its orbit originates from the time or space variation of $\vec{E}$. In [10] both the polarization drift and stress tensor drift are evaluated.

2.3.4 The Energy Equation

The highest order moment equation that is used is the energy equation. To treat the flow of energy, the next momentum in the Vlasov equation has to be considered. By multiplying the Vlasov equation by $\frac{1}{2}m\vec{v}\vec{v}$, the heat flow equation results in the form

$$\frac{3}{2}\left(\frac{\partial}{\partial t} + \vec{v}_j \cdot \nabla\right) p_j + \frac{5}{2} p_j \nabla \cdot \vec{v}_j = -\nabla \cdot \vec{q}_j - \pi_j \nabla \vec{v}_j + Q_j \tag{2.21}$$

where $\vec{q}_j$ is the heat flux and Q_j is the heat transfer from one species to another by means of collisions which here is neglected. Another usual form of the energy equation is obtained after substracting the continuity equation (2.9). It is written as

$$\frac{3}{2} n_j \left(\frac{\partial}{\partial t} + \vec{v}_j \cdot \nabla\right) T_j + p_j \nabla \cdot \vec{v}_j = -\nabla \cdot \vec{q}_j \tag{2.22}$$

The heat flux $\vec{q_j}$ for the collision dominating case ($\lambda \gg l_f$), with λ the wavelength and l_f the mean free path, according to Braginskii [7]

$$\vec{q_j} = 0.71 n_j T_j \vec{U}_{||} - \kappa_{||} \nabla_{||} T_j - \kappa_{\perp} \nabla_{\perp} T_j + \vec{q}_{\star j} + \frac{3}{2} \nu_j \frac{n_j T_j}{\omega_{cj}} (\vec{e}_{||} \times \vec{U}) \tag{2.23}$$

where $\vec{U}$ is the relative velocity between species. $\kappa_{||j}$ and $\kappa_{\perp j}$ represents the thermal conductivity for in parallel and perpendicular direction for ions and electrons and

$$\vec{q}_{\star j} = \frac{5}{2} \frac{n_j T_j}{m_j \omega_{cj}} (\vec{e}_{||} \times \nabla T_j) \tag{2.24}$$

One has

$$\nabla \cdot \vec{q}_{\star j} = \frac{5}{2} n_j (\vec{v}_{\star j} - \vec{v}_{Dj}) \cdot \nabla T_j \tag{2.25}$$

where

$$\vec{v}_{Dj} = \frac{T_j}{m_j \omega_{cj}} \vec{B} \times \left(\frac{\nabla B}{B} + \kappa \right) \tag{2.26}$$

is the drift due to $\nabla |B|$ and magnetic curvature $\kappa = \vec{B} \cdot \nabla \vec{B}$. We have also $\vec{k} \cdot \vec{v}_{Dj} = \omega_{Dj}$ is the $\nabla |B|$ and curvature drift frequency.

The equations (2.21) and (2.22) are fluid equations and the velocities contain the diamagnetic drifts.

2.4 Drift-waves

The micro-instability considered in this thesis is excited through the onset of drift type waves. These waves, which are driven by temperature and density inhomogeneities have their name from their propagation velocity, the electron diamagnetic drift velocity.

To understand how waves can create turbulence, one has to think of the surface of a pond. If a stone is thrown in, a well defined circular wave starts to propagate from the point where the stone hit the water. If, instead, a bunch of stones are thrown in, the water surface becomes jumbled. Even though each stone still create a well defined wave, the merging of all waves from all stones renders the surface chaotic. In a similar way, a magnitude of drift waves causes the motion of the turbulent motion in plasma. Hence, if one can improve the understanding of the excitation and driving mechanisms of these waves one might be able to suppress them and the turbulence they create.

J.B. Taylor [8] showed in 1977 that the drift waves could be damped due to tilted magnetic filed lines in a tokamak plasma (magnetic shear damping). This

damping mechanism may be decreased to the extent that it is lost by coupling of drift modes situated on different magnetic surfaces.

For a plasma, or any other gas, to be completely stable it has to be in thermodynamical equilibrium. This requires a Maxwell distributed plasma particles and a spatial homogeneous plasma density. If the mobility of the particles is restricted and the plasma is confined, these conditions are invariably broken. The plasma then tries to regain equilibrium by exciting turbulent processes.

Drift waves are low frequency waves, ($\omega \ll \omega_{ci}$), and have an electric field component along the magnetic field. The parallel electric field allows electrons to flow freely along the magnetic field lines and cancel any space charge in the plasma. In addition, low frequency modes have often quite a slow variation along the magnetic field lines and usually we assume that $k_\perp \gg k_{||}$, where $k_\perp$ and $k_{||}$ are the wave vector perpendicular and parallel to the magnetic field, respectively.

Since, the pressure inhomogeneities which drive drift waves are inherent in confined plasma, this type of instability is often referred to as the universal instability. In the very beginning we assume that the temperatures are constant and thus the drift waves will be driven exclusively by density inhomogeneities.

2.4.1 The Universal Instability

From electromagnetic field theory we know that charged particles are trapped around a magnetic field line due to a Lorentz force, but can move freely along the magnetic field line. Moreover, any gas which contains particles which move without constraint tends to equilibrate the temperature and the so called thermalization takes place. The long wavelength characteristic along the magnetic field lines of drift waves allow electrons to flow freely parallel to the magnetic field. Thermalized electrons obey the Boltzmann relation

$$n = n_e e^{(e\phi/T_e)}, \tag{2.27}$$

where n_e is the ambient electron density, e is the electron charge, ϕ is the perturbed electrostatic potential and T_e is the electron temperature.
If the perturbation in the potential is small, we can expand equation (2.27) in Taylor series around zero and the perturbed electron density $\tilde{n}_e$ becomes

$$\frac{\tilde{n}_e}{n_e} = \frac{e\phi}{T_e}, \tag{2.28}$$

so $\tilde{n}_e$ and ϕ are in phase. The density fluctuation in Fig.(2.4) also depicts a potential variation. The equation (2.28) describes the so called 'adiabatic' behaviour.

At point 1 in figure (2.4) the density is larger than in the equilibrium, $\tilde{n}_e$ is positive, and therefore ϕ is positive. Similarly, at point 2, $\tilde{n}_e$ and ϕ are negative. The difference in potential means there is an electric field $\vec{E}_1$ between points 1 and 2. Together with the background magnetic field $\vec{B}_0$, $\vec{E}_1$ creates a plasma flow with the $\vec{E} \times \vec{B}$ - velocity $\vec{v}_E$. As can be seen, the flow pushes the plasma in the x direction between points 1 and 2 and then pulls the plasma in x direction between points 2 and 3, so that the perturbation starts to oscillate. So, if one stands in point 1 can observe the plasma of different densities move back and forth. This results in the density perturbation propagating in y direction. A drift wave, therefore, has a motion such that the plasma moves back and forth in the x direction although the wave travels in y direction [9].

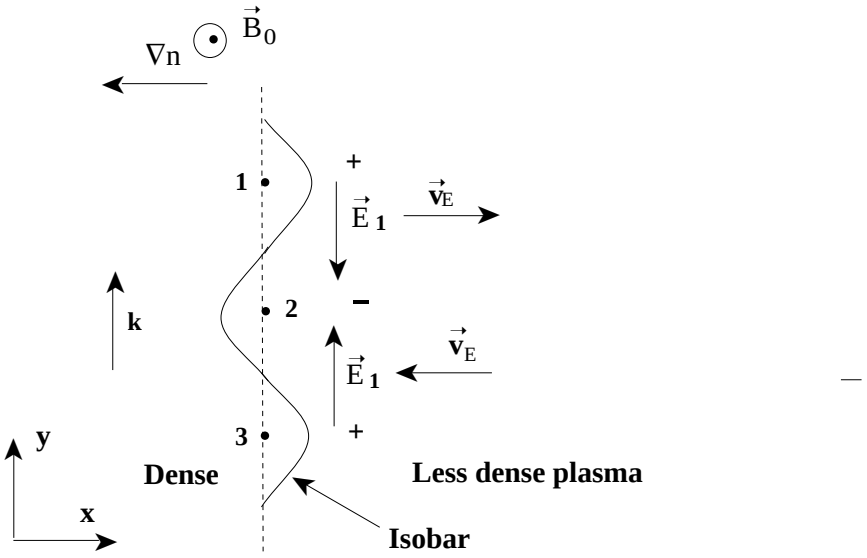

Figure 2.4: Density perturbation in a plasma depicted by a fluctuation of the isobar. The perturbation propagates in the $\vec{k}$ direction.

The instability of the drift waves comes about when one realize that the velocity, $\vec{v}_E$ for ions is not quite the $\vec{E} \times \vec{B}$ velocity. Corrections have to be calculated for drifts arising from temporal and/or spatial variations in the electric fields. As a result of these drifts, the electrostatic potential ϕ always lags behind the perturbed density $\tilde{n}_e$. Plasma already shifted outwards then has a velocity $\vec{v}_E$ also pointing outwards and vice-versa. Hence the amplitude of the perturbation increases and waves become unstable.

The electric field $\vec{E}_1$, in the above model (Fig.(2.4)), would be short-circuited by the unobstructed electron flow along the magnetic field lines. In reality, there

are mechanisms which impede the electron motion such as electron-ion collisions, magnetic mirror trapping of the electrons and Landau damping. When electron can no longer provide quasineutrality, a phase shift between the perturbed density and electrostatic potential emerges and one can write into equation (2.28)

$$\frac{\tilde{n}_e}{n_e} = \frac{e\phi}{T_e}(1 - i\delta), \tag{2.29}$$

which describes the 'nonadiabatic' behaviour. The resulting resistivity, given by the phase shift δ, in conjunction with the long wavelength along the magnetic field lines creates a potential drop and makes a finite value of $\vec{E}_1$ possible.
One can conclude that drift waves are always present in plasma and these waves are intrinsically unstable.

2.4.2 Reactive modes

In the present section we study the drift-type modes which, now, are driven by temperature inhomogeneities in addition to density inhomogeneities. This class of modes are called reactive drift modes and do not necessarily require dissipative effects to be unstable. As it has been already said, to destabilize drift waves driven only by density inhomogeneities demands some kind of mechanism which inhibits electrons from flowing freely along the magnetic field lines and neutralize space charge. The mechanism that renders the reactive drift modes unstable is the competition between the compression and expansion, driven by density and temperature inhomogeneities which enter into the energy equation. The energy equation plays an important part when it comes to closing the system of fluid equations introduced in section 2.3. Since we are dealing with both, temperature and density perturbations, the energy equation will be needed to close the system. In the energy equation, different fluid models use different methods to truncate the expression for the heat flow and this is what distinguishes one fluid model from another. The Weiland model [10] inserts the expression of the diamagnetic heat flow into the energy equation to close the set of fluid equations.

From the perspective of plasma confinement, reactive drift modes are commonly considered the second most dangerous after MHD modes and are likely to be a significant source of anomalous transport.

The driving mechanism responsible for the reactive drift type waves is the interchange instability [9]. This instability is closely related to the Rayleigh-Taylor instability response for the mixing of fluids when a light fluid supports a denser fluid.

A classical example of this is the convection taking place in a saucepan. The heating of the fluid from below, causes the fluid to expand, and as a result, it becomes less dense than the cooler fluid on top. When the density difference reaches a critical value, the lighter fluid rises and changes place with the cooler fluid, which heats up and the convection motion of the fluid is excited. The driving force in this case is the gravity.

In plasma, the magnetic field plays the role of the lighter fluid supporting the heavier plasma fluid. The gravitational force is replaced by the centrifugal force experienced by the plasma particles following the curved magnetic field lines of the toroidal plasma. Heating of plasma is redundant. Since the magnetic field lines lie closer together at the inside of the toroidal plasma, compression, which heats the plasma automatically, occurs when particles move along the field lines.

The interchange stability is essentially a magnetohydrodynamic instability but it can be recovered for drift-type waves in two cases. First, if some of the electrons are trapped, e.g. due to the curvature of the magnetic field, they are not able to cancel space charge which implies that curvature drifts lead to charge separation [11]. Secondly, the curvature of the magnetic field in combination with temperature gradients can give an interchange-type mode which does not correspond to the charge separation but rather to the compressibility of the plasma. One more mode will be also briefly discussed, the electron temperature gradient. We will start by considering the second case when an ion temperature gradient is present in a toroidal plasma [12].

Ion Temperature Gradient Mode

There is now substantial experimental evidence that anomalous energy and particle losses observed in large scale tokamak discharges can occur through the ion conduction channel [13]. In this case, the dominating instabilities causing the transport in the bulk part of the plasma are considered to be electrostatic, low-frequency drift wave type modes which are driven by the density and temperature gradients, and inhomogeneities in the magnetic field. A particular class of drift instabilities which has been recently proposed as the most probable candidate to explain the anomalous ion thermal transport in tokamaks is the ion temperature gradient (ITG) driven drift mode, so called η_i=L_{ni}/L_{Ti} mode, where L_{ni} and L_{Ti} are the characteristic length scales of the density and the temperature inhomogeneity respectively. Two important features of the η_i mode make it interesting for implication to experimental observations. First, the mode has a threshold in η_i in order to be unstable,

$\eta_i > \eta_{ic} \geq 1.5$, where η_{ic} denotes the critical value η_i necessary for instability. Therefore, the mode is expected to be important in devices with broad density profiles ($\eta_i > 1$). Second, being a reactive drift mode, its dynamics is independent of collisions. This characteristic is also in quantitative agreement with observed anomalies in the ion thermal transport.

The ITG instability was first identified in the slab geometry where it occurs as a modified ion-acoustic wave [14]. Later it was found that another branch of this mode can be destabilized by interchange effects even in the $k_{||} \to 0$ limit, and this branch is in fact the one with the largest growth rate. In the later case the toroidal effects dominate in the dynamics of the mode. The growth rate of the toroidal ITG driven mode is typically two or three times larger than the growth rate of the slab ITG modes [15].

Typically, the fastest growing ITG driven modes exhibit a perpendicular scale of the order of the ion Larmor radius, satisfying $k_\perp^2 \rho_s^2 \sim 1$. This means that the ITG spatial scale is small compared to the tokamak minor radius, but much larger than the Debye length. Frequencies are in the range of the diamagnetic drift frequency $\omega_\star$, therefore much lower than the plasma frequency.

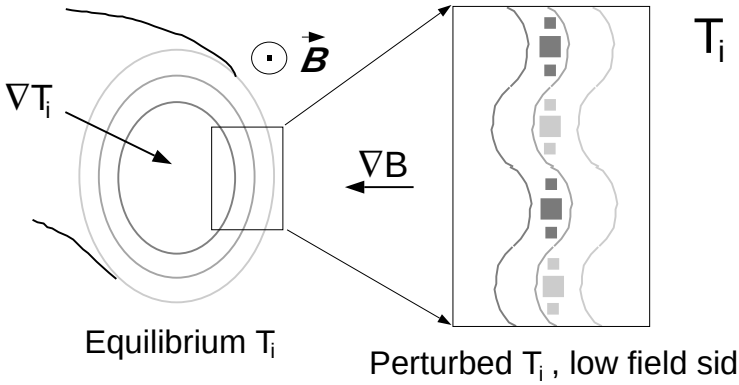

Figure 2.5: T_i perturbation in the low field side of the tokamak: $\nabla B \,||\, \nabla T_i$.

The toroidal version of this mode is basically due to the combination of the curvature and ∇B ion drifts on the one hand, and the $\vec{E} \times \vec{B}$ drift on the other. A simplified picture of the instability in toroidal geometry can be given assuming a local approximation, where each Fourier component of the perturbation is considered independent, thus neglecting the possible coupling effect of plasma inhomogeneities [18]. The instability grows in the unfavorable curvature region, where ∇Ti and ∇B are parallel; this is the case in the low field side of tokamaks. A magnetic surface has constant T_i, unless a perturbation occurs for some reason (figure 2.5). The poloidal

ion drift, due to, both, ∇B as well as magnetic field curvature, is proportional to T_i.

Therefore, if T_i is perturbed, this drift leads to a compression of ion density in the poloidal direction, with queues where the poloidal velocity gradient is negative and rarefaction in the zones with positive velocity gradient (figure 2.6). Quasi-neutrality forces a corresponding electron density perturbation which is equal and hence also in phase with the ion density perturbation. The electrons can assumed to be adiabatic because of their fast dynamics, yielding an electrostatic potential proportional to the density perturbation and with the same phase:

$$\frac{\tilde{n}_e}{n_e} = \frac{e\phi}{T_e} \tag{2.30}$$

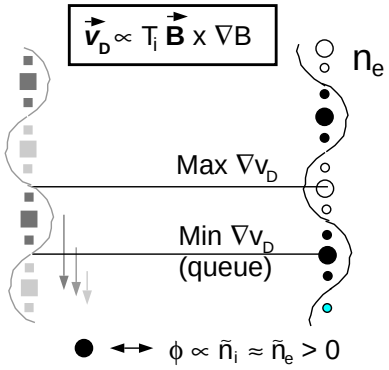

Figure 2.6: n_i compression due to the magnetic curvature and ∇B.

The density perturbation is, therefore, associated with a poloidal variation of ϕ, which gives rise to a radial electrostatic drift (figure 2.7). The perpendicular ion fluid motion carries plasma from the side with lower B to the cold spot and from the higher B region to the warm spot. If the background ∇T_i is parallel to ∇B, cold plasma is carried to the cold region, thus amplifying the perturbation and driving the instability, as shown in figure (2.7). A net amount of heat is transported as to flatten the background ion temperature gradient: in figure (2.7), the heat flows towards the right hand side. We notice that, since $\vec{v}_E$ and $\tilde{n}_e$ are phase shifted by $\pi/2$, there is no net particle transport according to this simplified model.

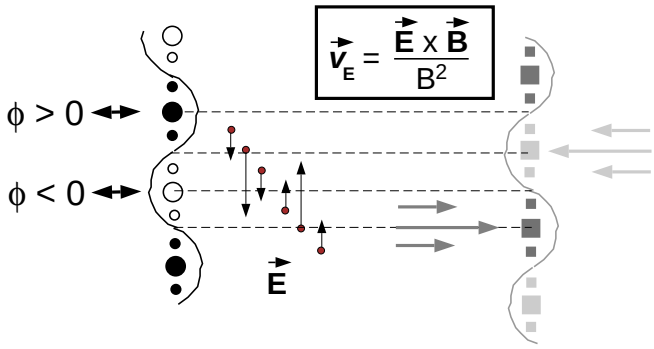

Figure 2.7: Amplification of the perturbation in T_i through the electrostatic drift, last step of the $n_i - T_i$ instability loop.

To derive a dispersion relation for the ion temperature (ITG) modes we reapply the two fluid model used in the previous section. After replacing the expression for the total velocity equation (2.15) in the continuity equation (2.9), the continuity equation in case of ITG modes takes the form

$$\frac{\partial n_i}{\partial t} + \cdot\nabla(n_i\vec{v}_{||}) + \nabla \cdot (n_i\vec{v}_E) + \nabla \cdot (n_i\vec{v}_{\star i}) + \nabla \cdot [n_i\,(\vec{v}_{pi} + \vec{v}_{\pi i})] = 0, \tag{2.31}$$

where the drift velocities, $\vec{v}_E$, $\vec{v}_{\star i}$, $\vec{v}_{\pi i}$, $\vec{v}_{pi}$ have been already introduced in section (2.1) and their expressions in the case of the ions is written by equations (B.4).
In the following derivation we neglect, for simplicity, the parallel ion motion term $\nabla \cdot (n_i\vec{v}_{||})$, although it will be included later in our model. An estimate of this quantity can be found in appendix B, equation (B.5). In the continuity equation we introduce the density $n_i \to n_i + \tilde{n}_i$ by defining the harmonic perturbation

$$\tilde{n}_i \to \tilde{n}_i e^{(i\vec{k}\cdot\vec{r} - i\omega t)}.$$

The frequency is in general a complex quantity, i.e. $\omega = \omega_r + i\gamma$. In this convention, an instability occurs if $\gamma > 0$. The linearized first order equation has the form

$$\frac{\partial \tilde{n}_i}{\partial t} = -n_i\nabla \cdot \tilde{\vec{v}}_{drift} - \nabla n_i \cdot \tilde{\vec{v}}_{drift} - \tilde{n}_i\nabla \cdot \vec{v}^{(0)}_{drift} - \nabla\tilde{n}_i \cdot \vec{v}^{(0)}_{drift}, \tag{2.32}$$

- where $\vec{v}_{Di}$ is no fluid drift, so it does not appear in the fluid equations and does not contribute directly to $\nabla \cdot (n_i\vec{v}_i)$.

- $\nabla\tilde{n}_i/\nabla n_i$ can be assumed to be of the order 1 at the saturation, but in the linear case it is arbitrarily small.

- The products $\tilde{n}_i \nabla \cdot \vec{v}^{(0)}_{drift}$ and $\nabla \tilde{n}_i \cdot \vec{v}^{(0)}_{drift}$, where $\vec{v}^{(0)}_{drift}$ is the background velocity, should be considered, but here we assume that the background velocity is zero. In the following, for simplicity, we write $\vec{v}_{drift}$ instead of $\tilde{\vec{v}}_{drift}$. Calculation with the drift background velocity different from zero will to be considered later in our calculations.

Equation (2.32) is written as:

$$-i\omega\tilde{n}_i = -n_i \nabla \cdot \vec{v}_E - \nabla n_i \cdot \vec{v}_E - \nabla \cdot [n_i(\vec{v}_{pi} + \vec{v}_{\pi i})] - \nabla \cdot (n_i \vec{v}_{\star i}). \tag{2.33}$$

In appendix B, equations (B.5), all terms appearing in equation (2.33) are evaluated. The density inhomogeneities in equation (2.31) are coupled with the temperature inhomogeneities through the energy equation

$$\frac{3}{2} n_i \left(\frac{\partial}{\partial t} + \vec{v}_i \cdot \nabla \right) T_i + n_i T_i \nabla \cdot \vec{v}_i = -\nabla \cdot \vec{q}_i. \tag{2.34}$$

In equation (2.34) the ion heat flux, $\vec{q}_i$ is given by the diamagnetic expression

$$\vec{q}_{\star i} = \frac{5}{2} \frac{n_i T_i}{m_i \omega_{ci}} (\vec{e}_{||} \times \nabla T_i), \tag{2.35}$$

and with this truncation the fluid hierarchy is closed. The divergence of the heat flux in equation (2.34) takes the form

$$\nabla \cdot \vec{q}_{\star i} = \frac{5}{2} n_j (\vec{v}_{\star j} - \vec{v}_{Dj}) \cdot \nabla T_j \tag{2.36}$$

where $\vec{v}_{Di}$ is the total magnetic drift of the ions due to $\nabla |B|$ and the magnetic curvature. Here, the first convective diamagnetic part cancels with other convective diamagnetic terms after substitution of the continuity equation for $\nabla \cdot \vec{v}_i$. We shall here retain the curvature part of $\vec{q}_{\star i}$, which will turn out to be very important.
The linear temperature perturbation is now

$$\frac{\tilde{T}_i}{T_i} = \frac{\omega}{\omega - \frac{5}{3}\omega_{Di}} \left[\frac{2}{3} \frac{\tilde{n}_i}{n_i} - \frac{\omega_{\star e}}{\omega} \left(\frac{2}{3} - \eta_i \right) \frac{e\phi}{T_e} \right]. \tag{2.37}$$

Inserting equation (2.37) into the linearized ion continuity equation (2.31) reveals

$$\frac{\tilde{n}_i}{n_i} = \frac{\omega \left(\omega_{\star e} - \omega_{De} \right) + \left(\eta_i - 7/3 + 5/3\varepsilon_n \right) \omega_{\star e} \omega_{Di} - k^2 \rho_s^2 \left(\omega - \omega_{\star iT} \right) \left(\omega - 5\omega_{Di}/3 \right)}{\omega^2 - 10\omega\omega_{Di}/3 + 5\omega_{Di}^2/3} \frac{e\phi}{T_e} \tag{2.38}$$

Here we have introduced the diamagnetic drift frequency $\omega_{\star j} = \vec{k} \cdot \vec{v}_{\star j}$, $j = e, i$, magnetic frequency $\omega_{Dj} = \vec{k} \cdot \vec{v}_{Dj}$, where $\vec{k}$ the perpendicular wave vector, the

ion Larmor radius at the electron temperature, $\rho_s = c_s/\omega_{ci}$, the ion sound speed $c_s = \sqrt{T_e/m_i}$, $\omega_{\star iT} = \omega_{\star i}(1+\eta_i)$, $\varepsilon_n = 2L_n/R$.
The polarization drift and the lowest order FLR effects are also included here. The key property of equation (2.37) is that we obtain the correct isothermal limit $\tilde{T}_i \to 0$ when $\omega_{Di} \gg \omega, \omega_{\star i}$. This is entirely due to the curvature part of $\nabla \cdot \vec{q}_{\star i}$, which enters as an additional higher order contribution to the pressure force that may be either destabilizing or stabilizing. For ion temperature modes it is usually stabilizing.
To find the dispersion relation of ITG modes it is assumed that the quasineutrality holds and that the electrons are Boltzmann distribution. Replacing $\tilde{n}_i/n_i$ in equation (2.38) with $\tilde{n}_e/n_e$, equation (2.28,) yields the dispersion relation

$$\omega = \omega_r + i\gamma. \tag{2.39}$$

The real part

$$\omega_r = \frac{1}{2}\omega_{\star e}\left[1 - \varepsilon_n\left(1 + \frac{10}{3\tau}\right) - k^2\rho_s^2\left(1 + \frac{1+\eta_i}{\tau} - \varepsilon_n - \frac{5}{3\tau}\varepsilon_n\right)\right] \tag{2.40}$$

and the growth rate

$$\gamma = \frac{\omega_{\star e}\sqrt{\varepsilon_n/\tau}}{1+k^2\rho_s^2}\sqrt{\eta_- \eta_{thi}}, \tag{2.41}$$

with the ITG threshold,

$$\eta_{thi} = \frac{2}{3} - \frac{\tau}{2} + \varepsilon_n\left(\frac{\tau}{4} + \frac{10}{9\tau}\right) + \frac{\tau}{4\varepsilon_n} - \tag{2.42}$$

$$\frac{k^2\rho_s^2}{2\varepsilon_n}\left[\frac{5}{3} - \frac{\tau}{4} + \frac{\tau}{4\varepsilon_n} - \left(\frac{10}{3} + \frac{\tau}{4} - \frac{10}{9\tau}\right)\varepsilon_n + \left(\frac{5}{3} + \frac{\tau}{4} - \frac{10}{9\tau}\right)\varepsilon_n^2\right].$$

The presence of ε_n in η_{thi}, introduces an upper stability limit for large ε_n. Usually, large values of ε_n can be found in the bulk of tokamak plasma and especially in the so called high confinement regime in which flat density profiles are common. It is noticed that the ITG growth rate equation (2.41) and the threshold equation (2.42) depend on both the ion and electron temperature explicitly. As it will be seen later this in not the case for trapped electron mode. ε_n is referred to as fully toroidal, its influence being one of the most important toroidal effects on drift-type waves.

Electron Temperature Gradient Mode

A mode that is sometimes used to explain the anomalous electron and heat transport in a collisionless regime is the electron temperature gradient (ETG) mode. This

mode exists in both slab and toroidal version. It is a very short wavelength mode which satisfied

$$\rho_e \ll \lambda \ll \rho_i.$$

The ETG mode is characterized by a large mode number which makes the frequency large, $\omega > \omega_{ci}$. The equations that describe the microinstability driven by ETG are very similar with those describing the ITG. In fact, the linear instabilities are exactly the same, except the species labels for length and time scales are exchanged. The length scale for each is the Larmor radius for the non-adiabatic species, ρ_e and ρ_i respectively.

The ITG mode propagates in the ion drift direction and ETG mode propagates in the electron drift direction. Due to its short wavelength, the ETG mode only gives a small nonlinear transport. However, it can excite modes with longer wavelength through mode coupling. The slab version of the ETG mode is analogous to that of ITG mode.

Trapped Electron Mode

When electrons are no longer free to move along the magnetic field lines and cancel the space charge caused by the difference between the ion and electron curvature drifts, the interchange instability is recovered. The magnetic configuration of the tokamak, with stronger magnetic field on the inside (plasma facing the 'hole' of the doughnut) than the outside, traps the electrons in the so called banana orbits (as have been already discussed in the previous chapter).

The trapped electrons do not contribute to the current parallel to the magnetic field, since their bounce averaged velocity cancels out in this direction and one may subsequently neglect the parallel electron motion. Comparison of the kinetic integrals for trapped electrons and ions without parallel motion show that they are symmetric. One may thus use the same model equation for trapped electrons as for the ions. The Boltzmann distribution equation (2.28), valid exclusively for free electrons in the derivation of trapped electrons (TE) modes is replaced by

$$\frac{\tilde{n}_e}{n_e} = f_t \frac{\tilde{n}_{et}}{n_{et}} + (1 - f_t) \frac{\tilde{n}_{ef}}{n_{ef}}, \tag{2.43}$$

where $\tilde{n}_{ef}$ is the perturbed density of the free electron and $f_t = n_{et}/n_e$ is the fraction of trapped electrons given by $\tilde{n}_{et}$. Since is nothing to prevent the free electrons from becoming thermalized, one can suppose that they are Boltzmann distributed in accordance with equation (2.28).

If quasineutrality is assumed, so that $\tilde{n}_i = \tilde{n}_{ef} + \tilde{n}_{et}$, the dispersion relation can be obtained equating the ion density perturbation equation (2.38) with the equivalent expression for the trapped electrons and the Boltzmann distribution equation for the free flowing electron. This yields the dispersion relation,

$$\frac{\omega_{\star e}}{N_i}\left[\omega\left(1-\varepsilon_n\right)+\left(\eta_i-\frac{7}{3}+\frac{5}{3}\varepsilon_n\right)\omega_{Di}-k^2\rho_s^2\left(\omega-\omega_{\star iT}\right)\left(\frac{\omega}{\omega_{\star e}}+\frac{5}{3\tau}\varepsilon_n\right)\right]$$

$$=f_t\frac{\omega_{\star e}}{N_e}\left[\omega\left(1-\varepsilon_n\right)+\left(\eta_e-\frac{7}{3}+\frac{5}{3}\varepsilon_n\right)\omega_{De}\right]+1-f_t \tag{2.44}$$

where

$$N_j=\omega^2-\frac{10}{3}\omega\omega_{Dj}+\frac{5}{3}\omega_{Dj}^2,\quad j=i,e. \tag{2.45}$$

The denominator N_j acts as the resonant denominator in the dispersion relation of a two-stream instability. When $N_i < N_e$, the mode propagates in the ion direction (ITG mode), and $N_e < N_i$, the mode propagates in the electron diamagnetic direction (TEM). Equation (2.44) is a quadratic equation in the frequency ω. Accordingly, it can have two modes unstable at the same time. For ε_n of the order of 1 the modes are rather independent, propagating in opposite directions, and the dispersion relation can be well approximated by neglecting the part with larger N_j in equation (2.44). For large ε_n, modes are strongly coupled and the direction of propagation may change. Ignoring the trapped electron part with denominator N_e we obtain the stability threshold

$$L_{T_i} > L_B\left[\frac{20(1-f_t)}{9f_t}+\frac{f_t}{2(1-f_t)}\right]^{-1}. \tag{2.46}$$

If instead we take N_i large, we obtain the only way of isolating a trapped electron mode which can be driven only by compressibility and the electron temperature gradient. This was first done in [16]. Since this mode is obtained for $N_e \ll N_i$, it is due to a fluid resonance.

2.5 Gyrokinetic Equations

Till now in this chapter we have introduced the simplest description of plasma, the fluid description. Investigating the plasma microinstabilities we are making use also of a more advanced code which contains a gyrokinetic approach for describing the

tokamak plasma. That's why, we find useful to describe briefly the general features of this approach.

The gyrokinetic approach has been widely used in recent years to study low frequency microinstabilities in a magnetically confined plasma. The electrostatic gyrokinetic model was originally derived by Rutherford and Frieman [17] and Taylor and Hastie [18] for low frequency modes ($\omega \ll \omega_{ci}$). Since then, gyrokinetic theory has been significantly advanced and its importance for magnetized plasmas, especially for magnetic fusion, has been greatly appreciated. The gyrokinetic system was first extended to electromagnetic modes by Catto [19] using the guiding center coordinates [20] and implemented by Antonsen [21]. Nonlinear electrostatic gyrokinetic equations for small amplitude perturbations were derived by Frieman and Chen [22], Lee [24], Dubin [25] and Yang [26] using the Hamiltonian Lie perturbation method and by Hahm [27] using the phase-space Lagrangian perturbation method. Recently, Hahm [28] and Brizard [29]- [31] developed the nonlinear electromagnetic gyrokinetic system. Meanwhile, a gyrokinetic system valid for both long wavelength and short wavelength modes (without using the ballooning representation) was investigated by Qin [32]- [35]. The importance of Maxwell equations was later realized. Lee [24] first discovered the difference between the gyrocenter density and the particle density in the Poisson equation, which was further studied by Dubin [25]. The gyrokinetic effect in the Ampere's law was the investigated by Hahm [27]. More recently, Sugama [36] and Brizard [37] publishing the most complete and elegant gyrokinetic descriptions.

Here, we are going to present the nonlinear electromagnetic gyrokinetic Vlasov equation obtained by Brizard [38], based upon earlier gyrokinetic studies [28], [39], [24], [25], [22], [23].

The standard gyrokinetic ordering is invoked as follow:

$$\frac{\omega}{\omega_{ci}} \sim k_{||}\rho_i \sim \frac{e\phi}{T} \sim \frac{\delta B}{B} \sim \frac{F_1}{F_0} \sim \frac{\rho_i}{L} \sim \varepsilon \ll 1, \;\; k_\perp \rho_i \sim 1, \tag{2.47}$$

where ω is a characteristic frequency of the fluctuations, $k_{||}$ and $k_\perp$ are typical fluctuation wavenumbers parallel and perpendicular to the equilibrium magnetic field, ω_{ci} is the ion cyclotron frequency, $c_{si} = \sqrt{Ti/mi}$ is the ion thermal speed, and $\rho_i = c_{si}/\omega_{ci}$ is the thermal ion gyroradius. L is a typical equilibrium scale length, such as the density scale length $L_n = -\nabla(lnn_0)^{-1}$, the temperature scale length $L_T = -\nabla(lnT_0)^{-1}$, or the plasma minor radius a or major radius R. T and B are typical equilibrium temperatures and magnetic fields, and F_0 is the equilibrium distribution. F_1 is the fluctuating distribution function, ϕ is the electrostatic potential,

and δB is the fluctuating component of the magnetic field.

Gyrokinetics averages over the fast gyromotion of particles around a strong magnetic field, reducing the kinetic equation from three to two velocity space dimensions, and leaving the magnetic moment μ as a rigorously conserved quantity. The gyrokinetic ordering takes advantage of the spatial anisotropy created by the strong magnetic field. Parallel to the field, particles can stream freely, and fluctuating wavelengths are long, $k_{||}L \sim 1$. Perpendicular to the field, particle motion is strongly restricted, and wavelengths scale with the gyroradius $k_\perp \rho_i \sim 1$.

The fluctuating distribution function is ordered small compared to the equilibrium distribution, which, here, is taken as a Maxwellian. Nonetheless, perpendicular gradients of fluctuating quantities are the same order as perpendicular gradients of the equilibrium ($k_\perp F_1 \sim F_0/L$), and hence the perpendicular nonlinearities due to the $\vec{E} \times \vec{B}$ drift and field line bending are kept, while parallel nonlinearities are small, and are ordered out here.

The gyrokinetic Vlasov equation is derived from the particle-kinetic Vlasov equation (2.7). A gyrocenter space coordinates is obtained by applying two transformations on the particle phase-space coordinates $(\mathbf{x}', \mathbf{v}')$. The first transformation is a guiding-center phase-space transformation, which eliminates the gyroangle dependence due to equilibrium or unperturbed magnetic field and introduces the guiding-center gyromomentum as an adiabatic invariant. The second transformation is the gyrocenter phase-space transformation which eliminates the gyroangle dependence reintroduced by the electromagnetic field fluctuations. The adiabatic invariance of the guiding-center gyromomentum is destroyed by these electromagnetic fluctuations and a new expression for the gyromomentum adiabatic invariant is recovered with the gyrocenter gyromomentum, whose lowest-order term is the guiding-center gyromomentum while higher-order terms correspond to arbitrary powers in electromagnetic fluctuations amplitude.

The transformation from the particle phase-space coordinates $\mathbf{z}' \equiv (\mathbf{x}', \mathbf{v}')$ to the guiding-center phase-space coordinates $\vec{Z}_0 \equiv (\vec{X}_0, v_{||0}, \mu_0, \zeta_0)$ is given in terms of asymptotic expansions in the small parameter $\varepsilon_B = \rho_i / L_B$, where L_B is the length scale associated with the equilibrium magnetic non-uniformity. To lowest order in ε_B, we have

$$\begin{aligned} \vec{X}_0(\mathbf{x}', \mathbf{v}') &= \mathbf{x}' - \vec{\rho}_0, \\ v_{||0}(\mathbf{x}', \mathbf{v}') &= \vec{e}_{||} \cdot \mathbf{v}', \end{aligned}$$

$$
\begin{aligned}
\mu_0(\mathbf{x}', \mathbf{v}') &= mv_\perp^2/2\omega_{ci}, \\
\zeta_0(\mathbf{x}', \mathbf{v}') &= \tan^{-1}\left(\vec{1}\cdot\mathbf{v}'/\vec{2}\cdot\mathbf{v}\right)',
\end{aligned}
\tag{2.48}
$$

where $v_\perp \equiv |\vec{e}_{||} \times (\mathbf{v}' \times \vec{e}_{||})|$, $\vec{\rho}_0 \equiv \omega_{ci}^{-1}\vec{e}_{||} \times \vec{v}_\perp = \rho_\perp(\cos\zeta_0\vec{1} - \sin\zeta_0\vec{2})$ is the gyroangle-dependent gyroradius vector, and $(\vec{1}, \vec{2}, \vec{e}_{||})$ form a right-handed set of local unit vectors at $\mathbf{x}'$. The guiding-center dynamic equations are

$$
\begin{aligned}
\dot{\vec{X}}_0 &= v_{||0}\vec{e}_{||} + \frac{\vec{e}_{||}}{m\omega_{ci}} \times (\mu_0\omega_{ci}\nabla lnB + mv_{||0}^2\vec{e}_{||}\cdot\nabla\vec{e}_{||}), \\
\dot{v}_{||0} &= -(\mu_0\omega_{ci}/m)\vec{e}_{||}\cdot\nabla lnB, \\
\dot{\mu}_0 &= 0, \\
\dot{\zeta}_0 &= \omega_{ci},
\end{aligned}
\tag{2.49}
$$

where $\vec{e}_{||}$ and B are evaluated at the guiding-center position $\vec{X}_0$; $\vec{X}_0$ and $\dot{v}_{||0}$ are given to first order in ε_B while $\dot{\mu}_0$ and $\dot{\zeta}_0$ are given to lowest order in ε_B. In this presentation, we neglect effects due to an equilibrium electrostatic potential, ϕ_{eq}, and consequently there is no equilibrium $\vec{E} \times \vec{B}$ velocity or equilibrium parallel electric field $E_{||}$ in (2.49). These effects should realistically be included but they are omitted for the simplicity of the presentation. The Jacobian for the guiding-center transformation (2.48) is ω_{ci}/m to lowest order in ε_B.

The transformation for the guiding-center phase-space coordinates $\vec{Z}_0$ to the gyrocenter phase-space coordinates $\vec{Z} \equiv (\vec{X}, v_{||}, \mu, \zeta)$ is

$$
\begin{aligned}
\vec{X} &= \vec{X}_0 + \delta A_\perp \times \frac{\vec{e}_{||}}{B} - \frac{1}{m}\left(\frac{\vec{e}_{||}}{\omega_{ci}} \times \nabla_0\delta S + \vec{e}_{||}\frac{\partial\delta S}{\partial v_{||0}}\right), \\
v_{||} &= v_{||0} + \frac{e\delta\tilde{A}_{||}}{mc} + \frac{\vec{e}_{||}}{m}\cdot\nabla_0\delta S, \\
\mu &= \mu_0 + \frac{e}{c}\left(\delta\vec{A}_\perp \cdot \frac{\partial\vec{\rho}_0}{\partial\zeta_0}\right) + \frac{\partial\delta S}{\partial\zeta_0}, \\
\zeta &= \zeta_0 - \frac{e}{c}\left(\delta\vec{A}_\perp \cdot \frac{\partial\vec{\rho}_0}{\partial\mu_0}\right) - \frac{\partial\delta S}{\partial\mu_0},
\end{aligned}
\tag{2.50}
$$

and these expressions are correct to first order in perturbation field amplitude. The perturbed fields are denoted δ. The perturbation fields $(\delta\phi, \delta A_{||}, \delta A_\perp)$ are calculated to the particle position $\mathbf{x}' = \vec{X}_0 + \vec{\rho}_0$ and thus are gyroangle dependent through $\vec{\rho}_0$;

$\delta\tilde{A}_{||}$ denotes the gyroangle-dependent part of $\delta A_{||}$, $\delta\tilde{A}_{||} = \delta A_{||} - \langle \delta A_{||} \rangle$, where $\langle\ \rangle$ denotes gyroangle averaging. The perturbation field, $\delta S(\vec{X}_0, v_{||0}, \mu_0, \zeta_0, t)$, appearing in (2.50) is solution of $d\delta S/dt = e\delta\psi$, where $\delta\psi \equiv \delta\phi - \delta\vec{A} \cdot (v_{||0}\vec{e}_{||} + \omega_{ci}\vec{\rho}_0 \times \vec{e}_{||})/c$.

The gyrokinetic Vlasov equation is written in terms of gyrocenter phase-space coordinates $(\vec{X}, v_{||}, \mu, \zeta)$ as

$$\frac{\partial F}{\partial t} + \dot{\vec{X}} \cdot \nabla F + \dot{v}_{||}\frac{\partial F}{\partial v_{||}} = C(F), \tag{2.51}$$

where the gyrocenter distribution function in the gyrocenter phase-space coordinates F and the particle distribution function f are related by $F(\vec{Z}, t) \equiv f(\mathbf{z}'(\vec{Z}, t))$ or $f(\mathbf{z}', t) \equiv F(\vec{Z}(\mathbf{z}', t))$. Within the gyrokinetic ordering ($\omega \ll \omega_{ci}$), the gyrophase angle ζ is effectively averaged over, and does not appear explicitly ($\partial F/\partial\zeta = 0$). The gyrocenter magnetic moment $\mu = v_\perp^2/2B + \mathcal{O}(\varepsilon)$ is exactly conserved and is contained by the equations only as a parameter. A collision operator C(F) has been added to the right hand side.

Equation(2.51) is solved up to $\mathcal{O}(\varepsilon^2)$ taking into account the gyrokinetic ordering defined by (2.47). When ordering terms in the gyrokinetic equation, all frequencies are compared to ω_{ci}, and all lengths to ρ_i. Hence, $\partial F/\partial t \sim \omega F_1$ is $\mathcal{O}(\varepsilon^2)$, because $\partial F_0/\partial t = 0$, $F_1/F_0 \sim \varepsilon$ and $\omega/\omega_{ci} \sim \varepsilon$. Any gradient operator acting on F_0 or B is $\mathcal{O}(\varepsilon)$ because $\rho_i/L \sim \varepsilon$. A parallel gradient on F_1 is proportional to $\mathcal{O}(\varepsilon^2)$ because $k_{||}\rho_i \sim \varepsilon$. However, a perpendicular gradient acting on F_1 is $\mathcal{O}(\varepsilon)$ because $k_\perp\rho_i \sim 1$. Because ∇F is $\mathcal{O}(\varepsilon)$, $\dot{\vec{X}}$ is needed only to $\mathcal{O}(\varepsilon)$, while $\dot{v}_{||}$ must include terms up to $\mathcal{O}(\varepsilon^2)$.

The fluctuating magnetic field $\delta\vec{B}$ is described to lowest order in terms of a magnetic potential along the equilibrium field, $\delta\vec{B} = \nabla \times A_{||}\vec{e}_{||}$. The perturbation along the equilibrium field ($\delta B_{||}$) is small for $\beta \ll 1$, as can be seen from perpendicular force balance, and $\delta B_{||}$ is neglected here. A local kinetic analysis by Horton [40] has found $\delta B_{||}$ to be unimportant for β of the order of the MHD critical β_c (ideal MHD limit) or smaller. However, the toroidal kinetic code of Kotschenreuther [41] has included $\delta B_{||}$ and found it to be somewhat important for $\beta \sim \beta_c$, particularly at low aspect ratio [42]. The gyrocenter velocity is then given by

$$\dot{\vec{X}} = v_{||}(\vec{e}_{||} + \frac{\langle \delta\vec{B}_\perp \rangle}{B}) + \vec{v}_E + \vec{v}_d. \tag{2.52}$$

The first term on the right hand side represents free streaming along the total magnetic field. The second term is the gyroaveraged $\vec{E} \times \vec{B}$ drift velocity, $\vec{v}_E = \frac{c}{B}\vec{e}_{||} \times \nabla\langle\phi\rangle$. $\vec{v}_d$ is the combined curvature and ∇B is the drift velocity. In general,

$\vec{v}_d$ can be written as

$$\begin{aligned}\vec{v}_d &= \frac{v_{||}^2}{\omega_{ci}}\vec{e}_{||}\times(\vec{e}_{||}\cdot\nabla\vec{e}_{||})+\frac{\mu}{\omega_{ci}}\vec{e}_{||}\times\nabla B \\ &= \frac{v_{||}^2+\mu B}{\omega_{ci}B^2}\vec{e}_{||}\times\nabla B+\frac{v_{||}^2}{\omega_{ci}B^2}\vec{e}_{||}\times(\nabla\times\vec{B}\times\vec{B})\end{aligned} \tag{2.53}$$

Using the equilibrium relations $\nabla p=\frac{1}{c}\vec{J}\times\vec{B}$ and $\nabla\times\vec{B}=\frac{4\pi}{c}\vec{J}$, this can be written

$$\vec{v}_d=\frac{v_{||}^2+\mu B}{\omega_{ci}B^2}\vec{B}\times\nabla B+\frac{v_{||}^2}{\omega_{ci}B^2}\vec{e}_{||}\times\nabla p \tag{2.54}$$

The second term on the right is small for $\beta\ll 1$, and is neglected here for simplicity and to maintain consistency with neglecting $\delta B_{||}$. The definition

$$\vec{v}_d=\frac{v_{||}^2+\mu B}{\omega_{ci}B^2}\vec{B}\times\nabla B+\frac{v_{||}^2}{\omega_{ci}B^2}\vec{B}\times\nabla B \tag{2.55}$$

is used henceforth.
The gyrocenter parallel acceleration can be written as

$$\begin{aligned}\dot{v}_{||} &= -\frac{e}{mc}\frac{\partial\langle A_{||}\rangle}{\partial t}-\frac{e}{m}(\vec{e}_{||}+\frac{\langle\delta\vec{B}_\perp\rangle}{B})\cdot\nabla\langle\phi\rangle \\ &\quad -\mu(\vec{e}_{||}+\frac{\langle\delta\vec{B}_\perp\rangle}{B})\cdot\nabla B+v_{||}(\vec{e}_{||}\cdot\nabla\vec{e}_{||})\cdot\vec{v}_E\end{aligned} \tag{2.56}$$

The first two terms on the right hand side represent the total parallel electric field, which includes a magnetic induction term, $-\frac{1}{c}\frac{\partial\langle A_{||}\rangle}{\partial t}$, and an electrostatic term evaluated along the total magnetic field. The next term is the total mirror force, and the final term is important for phase space conservation, as shown in [Hahm 1988; Beer 1995].

Using the definition $\delta\vec{B}=\nabla\times A_{||}\vec{e}_{||}$, the term $\delta\vec{B}_\perp$ can be written as follows

$$\delta\vec{B}_\perp=\vec{e}_{||}\times(\delta\vec{B}\times\vec{e}_{||})=-\vec{e}_{||}\times\nabla A_{||}+\vec{e}_{||}\times\vec{e}_{||}\cdot\nabla\vec{e}_{||}A_{||}, \tag{2.57}$$

or upon gyroaveraging,

$$\langle\delta\vec{B}_\perp\rangle=-\vec{e}_{||}\times\nabla\langle A_{||}\rangle+\vec{e}_{||}\times\vec{e}_{||}\cdot\nabla\vec{e}_{||}A_{||}. \tag{2.58}$$

The second term on the right hand side is $\mathcal{O}(\varepsilon^2)$ and therefore, it does not enter into equation (2.51) to the required order.

The gyroangle averages are expressed in terms of a gyroaveraging operator J_0 as follows:

$$\langle \phi \rangle = J_0(\alpha)\phi, \quad \langle A_{||} \rangle = J_0(\alpha) A_{||}, \tag{2.59}$$

where α is the operator defined by

$$\alpha = -i\frac{\sqrt{2\mu B}}{\omega_{ci}}\nabla_\perp = \frac{\sqrt{2\mu B}}{c_{si}} k_\perp \rho_i.$$

The operator J_0 is simply a Bessel function in Fourier space

$$\begin{aligned} J_0(\alpha) &= \frac{1}{2\pi}\int_0^{2\pi} d\zeta \exp\left(i\alpha\cos\zeta\right) = \sum_{n=0}^{\infty} \frac{1}{(n!)^2}\left(\frac{i\alpha}{2}\right)^{2n} \\ &= \sum_{n=0}^{\infty} \frac{1}{(n!)^2}\left(\frac{\sqrt{2\mu B}}{2\omega_{ci}}\right)^{2n} \nabla_\perp^{2n}. \end{aligned} \tag{2.60}$$

In real space, J_0 is an operator which does not, in general, commute with other operators, and must be treated with care. It should be noted that J_0 operates only on the electrostatic potential ϕ and the parallel magnetic potential, $A_{||}$, in equation (2.51).

Defining the unit vector along the total magnetic field as $\tilde{\vec{e}}_{||} = \vec{e}_{||} + \frac{\langle \delta \vec{B}_\perp \rangle}{B}$, and the total parallel electric field, $\tilde{\vec{E}}_{||} = -\frac{1}{c}\frac{\partial}{\partial t} J_0 A_{||} - \tilde{\vec{e}}_{||} \cdot \nabla J_0 \phi$, the gyrokinetic equation can be written as

$$\frac{\partial F}{\partial t} + (v_{||}\tilde{\vec{e}}_{||} + \vec{v}_E + \vec{v}_d)\cdot\nabla F + \left[\frac{e}{m}\tilde{E}_{||} - \mu\tilde{\vec{e}}_{||}\cdot\nabla B + v_{||}(\vec{e}_{||}\cdot\nabla\vec{e}_{||})\cdot\vec{v}_E\right]\frac{\partial F}{\partial v_{||}} = C(F). \tag{2.61}$$

Chapter 3

Linear gyro-kinetic stability calculations of electron heat dominated plasmas in ASDEX Upgrade.

In this chapter gyro-kinetic stability calculations are compared with the experimental results of ASDEX Upgrade. For this purpose, the well established stability code GS2 is used. Our goal is to explain some of the observed phenomena and to determine which parameters (based on theoretical description) could influence the transport level. In this study, we will concentrate on the low density electron heat discharge.

3.1 Introduction

The anomalous electron heat transport in toroidal magnetic confinement devices has been studied experimentally by many people over a large period of time [43, 44], and is in fact the best documented of all transport channels. The reason for the good documentation is twofold: the electron temperature can be measured relatively easily with a high sampling rate using the electron cyclotron emission from the plasma, and localized heating of the electrons is possible using electron cyclotron resonant heating. The latter also allows for perturbative experiments in which the propagation of a heat wave is studied. This is a very powerful tool since it allows for the study of the derivative of the heat flux with respect to the temperature gradient, a quantity of primary importance in the understanding of heat transport. Most of the experiments are done under dominant electron heating, with relatively cold ions,

a regime on which we will also concentrate in this chapter.

All the experimental results can not be reviewed within the scope of this chapter. Below we will only mention some striking published observations, which play a role for the work presented here. A relatively old observation is that the electron temperature profile shape reacts weakly to the change in power or deposition radius of the electron heating [45, 46, 47, 48, 49, 50]. This phenomena is known as profile consistency [51], profile resilience or profile stiffness. This resilience, however, is known not to be absolute, i.e. the profile does show differences when comparing strong on and off axis heating [52]. Widely different mechanisms in terms of the underlying physics have been proposed in the literature, to explain this phenomena.

A nonlinear dependence of the heat flux on the gradient is experimentally demonstrated by the fact that the heat conduction coefficient calculated from the heat wave (χ^{HP}) in general exceeds the heat coefficient calculated from the steady state solution [53] (χ^{PB}). A graphical representation of this phenomena can, for instance, be found in Figure 1 of [43]. Obviously, a sufficiently strong nonlinear dependence of the heat flux on the temperature gradient can explain the profile resilience, since largely different heat fluxes can be generated by small changes in the gradient.

Of interest is also the reported off-diagonal terms in the transport matrix that link the electron heat flux to the density gradient [54] and the dependence of the incremental heat diffusion coefficient on the safety factor $\chi_{HP} \propto q^{1\ to\ 2}$ [55] and density $\chi_{HP} \propto n_e^{-1\ to\ 0}$ [56, 55, 57].

Despite the large amount of experimental investigations, the corresponding comparison with theory is somewhat more limited. Different models have been proposed and tested against the experiment [58, 59, 60]. In this chapter we try to explain some basic features of the observations using the theory of micro-instabilities. For this purpose we will use the well established gyro-kinetic code GS2 [41]. We stress here, that our calculations are based on linear theory. It is our believe that only nonlinear calculations could give precise answers on the heat flux in a fully developed nonlinear state. However, in many nonlinear simulations of core transport the heat flux is found to scale largely with the quasi-linear estimate leaving a weaker scaling with parameters not described by the linear theory. Also linear calculations can be done for many more cases, and are a necessary first step to approach the understanding of electron heat transport. Because of this shortcomings we discuss mainly scalings of the heat flux with the parameters and do not attempt to determine the absolute level. It turns out that we can explain several observed phenomena, but that not all the observed scalings are recovered.

Profile resilience has been explained in different ways. The explanation directly connected with micro-instabilities, that are thought to be the consequence of the anomalous transport, is the strong increase of the transport with $\nabla T_e/T_e = 1/L_{Te}$ above a threshold for the mode. In fact there is a large amount of experimental evidence for such a threshold [61, 62, 63]. If, under experimental conditions, the threshold can not be exceeded by a large amount the profile will more or less reflect the threshold of the mode and will be self similar. However, as stated before, the electron stiffness is far from absolute and the relatively constant factor R/L_{T_e} that is found in many experiments with central heating is, therefore, somewhat puzzling. It is important to note here that the transport does not only increase with R/L_{T_e} but also with temperature through the gyro-Bohm factor, i.e. $\chi_e \propto T_e^{3/2}$. A larger electron heating power, leads to a larger heat flux but also to a larger electron temperature. The latter makes that substantially more heat can be transported at the same R/L_{T_e}, and the profile can appear very stiff, whereas in reality it is not (this is explained in more detail in [52]).

Our calculations extend the work previously done on ASDEX Upgrade [60] using the diagonal transport coefficients of the quasi-linear fluid model known as the Weiland model [64]. This model could represent the data relatively well. It was found that under normal heating conditions one can exceed the threshold by a factor two to three. Good agreement was, however, only obtained in discharges with 0.8 to 1 MA plasma current, at lower current the model tends to under predict the transport. Furthermore, other work [65] has raised questions on the effect of collisions which are not properly accounted for in the version of the model used. In this chapter we will study this dependence. Also the gyro-kinetic model gives a more accurate description of the threshold and quasi-linear heat flux.

The chapter is structured as follows. In the next section we determine the dominant mode and vary the parameters that can influence this mode around a reference set, directly calculated from an ASDEX Upgrade discharge, in order to determine the main parameter dependences under the experimental relevant conditions. Section III presents a comparison between the gyro-kinetic results and two other well known models GLF23 and Weiland model. In Section IV we present a direct comparison between the experiments and calculations. In Section V we discuss the implications of the calculations for the interpretation of the experiments, and in Section VI we give the conclusions.

3.2 The trapped electron mode

The plasmas studied are low density Electron Cyclotron Resonant Heated (ECRH) L-mode discharges of the ASDEX Upgrade experiment. They are taken from a series of experiments with shot number #14793 until #14796, of which the steady state electron temperature profiles are shown in Fig.3.1.

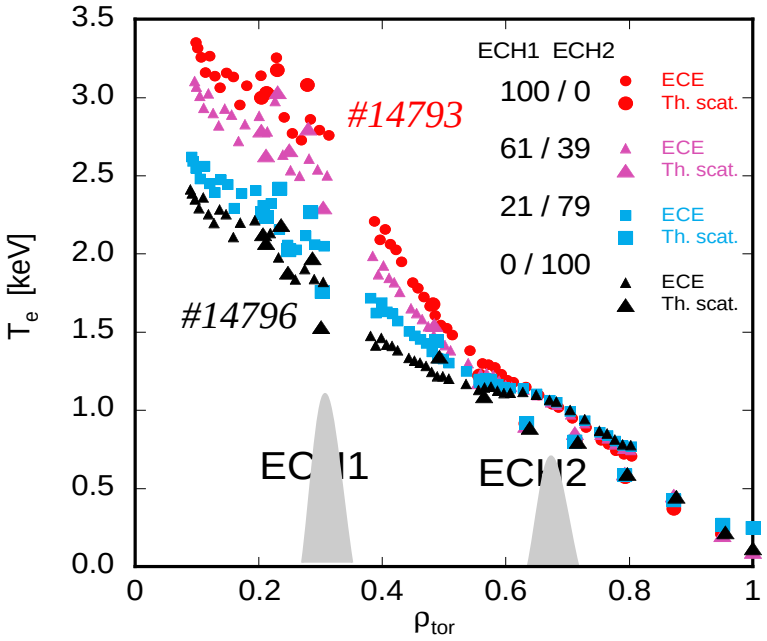

Figure 3.1: The electron temperature profiles for the different discharges in the series.

In this section we study the heat flux given by the micro-instabilities under experimental relevant conditions in order to determine their main dependences on the plasma parameters.

From the discharge #14793 (with on axis heating) a standard set of parameters, necessary for the stability analysis, has been calculated. All parameters are evaluated at the position $\rho_{tor} = 0.5$, and averaged over the time interval from 2.5 to 3.0 seconds. The standard set is given by: electron and ion density $n_e = n_i = 2.16\ 10^{19}$ m^{-3}, electron temperature $T_e = 1.5$ keV, ion temperature $T_i = 0.5$ keV, normalized inverse gradient lengths of the density, electron and ion temperature profile $R/L_{n_e} = 3.5$, $R/L_{T_e} = 7.9$, $R/L_{T_i} = 0$, safety factor $q = 1.57$, magnetic shear $\hat{s} = 1.07$, inverse aspect ratio $\varepsilon = r/R = 0.177$, and effective charge $Z_{eff} = 1$. The major radius of ASDEX Upgrade is $R = 1.65$ m and the magnetic field on axis in these discharges is 2.3 T. The gradient lengths given above are calculated using the

averaged midplane radius as radial coordinate, i.e. $r = (r_{out} - r_{in})/2$ where r_{out} (r_{in}) is the major radius of the outer (inner) crossing of the flux surface with the midplane. The off axis heated discharge had very similar parameters except for the lower normalized inverse gradient lengths. The accuracy of the different quantities are discussed in the next section where a direct comparison with the experiment is made. The calculations shown are done for circular geometry, whereas in reality the plasma is elongated, and has a low triangularity. The error made due to the approximation in the geometry, however, is small compared to the errors in the physics parameters.

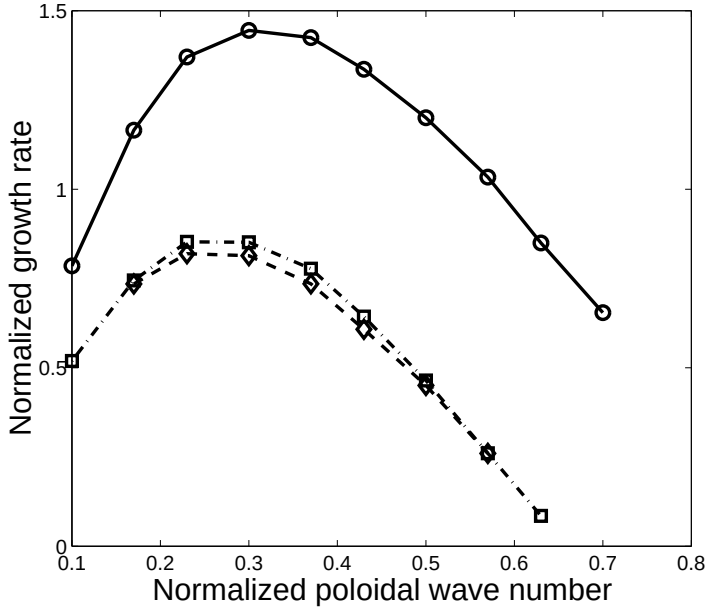

Figure 3.2: The normalized growth rate $\gamma R/v_{thi}$ as a function of the normalized poloidal wave number $k_\theta \rho_i$ for parameters of the standard set and the gradients of the electron temperature and density changed. Circles $R/L_{T_e} = 8$, $R_{L_n} = 3.5$, squares $R/L_{T_e} = 5$, $R_{L_n} = 3.5$, and diamonds $R/L_{T_e} = 8$, $R_{L_n} = 1.5$.

Figure 3.2 shows the normalized growth rate ($\gamma R/v_{thi}$) as a function of the normalized poloidal wave vector ($k_\theta \rho_i$). The ion thermal velocity and Larmor radius are used for normalization here. The parameters are that of the standard set with, however, the temperature and density gradient length changed (the values are given in the figure caption). The latter choice is motivated by the fact that these gradients have the largest influence on the mode as will be shown below. It can be seen that the maximum growth rate is obtained for $k_\theta \rho_i \approx 0.3$ in all cases.

The wavelength at which the maximum growth rate is obtained is insensitive to

the parameters of the simulation, with the exception of the electron temperature (for lower electron temperature the wave-number increases, Fig. 3.3). However, due to the design of the experiments the electron temperature does not vary much in the confinement region from shot to shot. Therefore, the results that will be shown below have all been calculated at constant $k_\theta \rho_i = 0.3$.

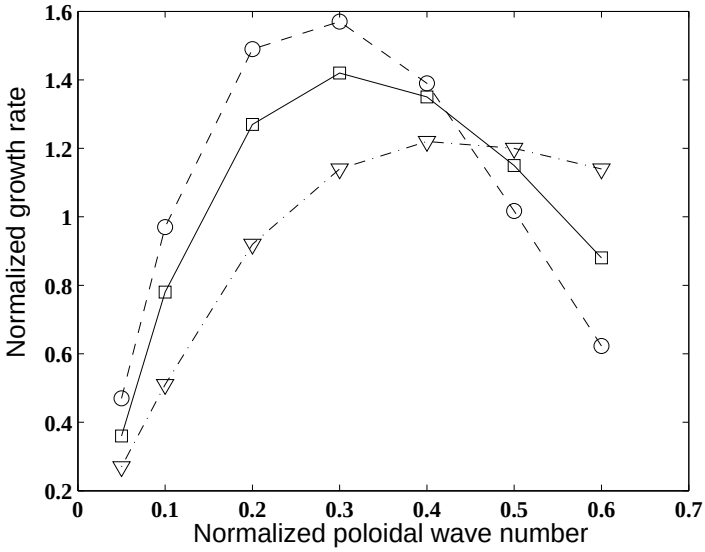

Figure 3.3: The normalized growth rate $\gamma R/v_{thi}$ as a function of the normalized poloidal wave number $k_\theta \rho_i$ for three different values of the electron temperature. Circles $T_e = 2$ keV, squares $T_e = 1.5$ keV, triangles $T_e = 1.0$ keV. All the other parameters are those of standard set.

The spectral range, as well as the real frequency which is in the electron diamagnetic direction, shows that the most unstable mode is a Trapped Electron Mode (TEM). This is further tested by increasing R/L_{Ti} as shown in Fig 3.4. It is known that at sufficient high R/L_{Ti} a transition to ion temperature gradient must occur. This transition occurs at $R/L_{Ti} \approx 7$ at which the frequency changes sign from the electron diamagnetic (positive) to ion diamagnetic (negative). Simulations at higher poloidal wave vectors show that the Electron Temperature Gradient mode (ETG) is stable in these discharges, which is related to the large electron to ion temperature ratio. This is further confirmed by the analytic formula for the threshold of the ETG [66] which gives $R/L_{crit} = 10.5$ for this case.

In the rest of this section the standard set of parameters is used, with one or two parameters being varied while the rest is kept constant. This is done in order to determine which of the parameters plays a dominant role in the TEM stability

under experimental relevant conditions.

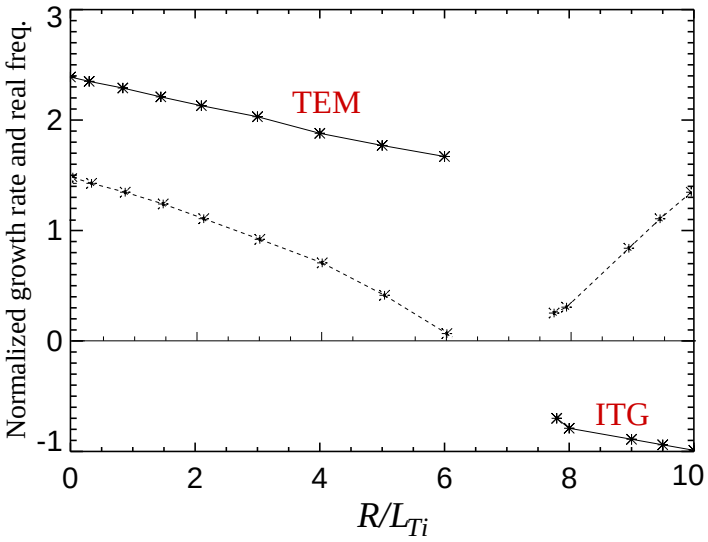

Figure 3.4: The normalized growth rate $\gamma R/v_{thi}$ (dashed line) and the normalized real frequency $\omega R/v_{thi}$ (full line) as a function of R/L_{Ti}.

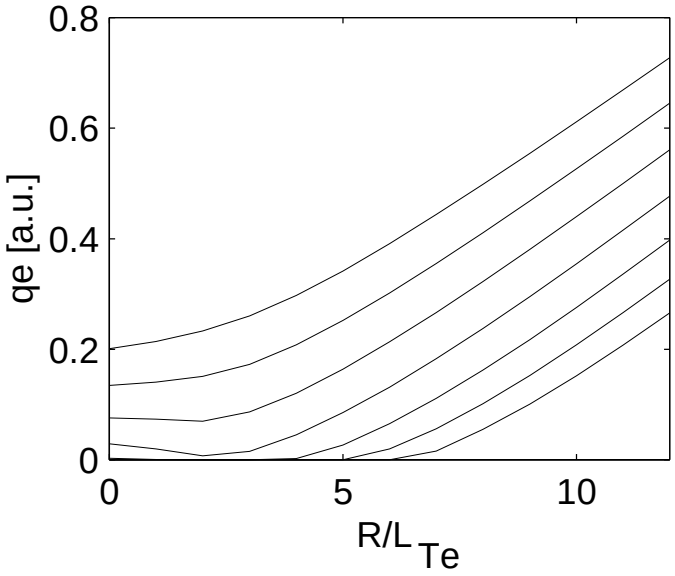

Figure 3.5: The quasi-linear heat flux in arbitrary units as a function of R/L_{Te} for different values of $R/L_n = (0, 1, 2, 3, 4, 5, 6)$. With increasing R/L_n the heat flux curve is shifted upward in the figure.

Figure 3.5 shows the quasi-linear heat flux of the mode as a function of R/L_{Te} for different values of R/L_{ne}. Since GS2 solves only the linear problem, it calculates

the electron heat flux normalized to $\langle|\phi|^2\rangle$, where ϕ is the electro-static potential. For the heat flux we then assume $\langle|\phi|^2\rangle \propto \gamma$, where γ is the growth rate of the most unstable mode, and the angle brackets denote the spatial average. This assumption is in agreement with the general mixing length estimate. Note that no wave vector is used here, since the calculations are done at fixed k_θ. The heat flux, thus obtained, is the quasi-linear heat flux except for an arbitrary scaling factor. The curves in the figure show the typical behaviour of the growth rate of the TEM. At sufficient high density gradient one finds two distinct regions. At zero temperature gradient length the mode is unstable due to the density gradient drive. In this region the mode becomes more stable when increasing the electron temperature gradient. In the second region at sufficient high electron temperature gradient the electron heat flux starts to increase linearly with the electron temperature gradient showing that the temperature gradient drive takes over. Nevertheless, also in this region the density gradient does part of the drive. Increasing the density gradient the curve of the heat flux is shifted upward as can be seen in Fig. 3.5. The density drive is well known from the theory on TEMs but is often ignored in the empirical description of the electron heat transport. These simulations show that it cannot be neglected under experimental relevant conditions. For sufficient steep density gradients the TEM is always unstable, i.e. does not show a threshold in R/L_{T_e}. It is worth noting too that all experimental observations made up to now on ASDEX Upgrade lie in the second region.

Figure 3.6 shows the electron heat flux as a function of R/L_{Te} for different values of the effective collisionality, the electron collision frequency (ν_e) normalized to the drift frequency (ω_{De})

$$\nu_{eff} = \frac{\nu_e}{\omega_{De}} \approx 0.1 \frac{n_e^\star Z_{eff}}{T_{ek}^2} \tag{3.1}$$

where $n_e^\star$ is the electron density in units of $10^{19}\ m^{-3}$, and T_{ek} is the electron temperature in units of keV. It can be seen that the electron collisions change the heat flux considerably. This is in line with previous observations on the influence of collisions on density transport [65]. Although the collision frequency normalized to the transit time is small and the electrons perform many bounces during one collision time, the collision frequency is not necessarily small against the frequency of the TEM, and can, hence, lead to a reduction of its growth rate.

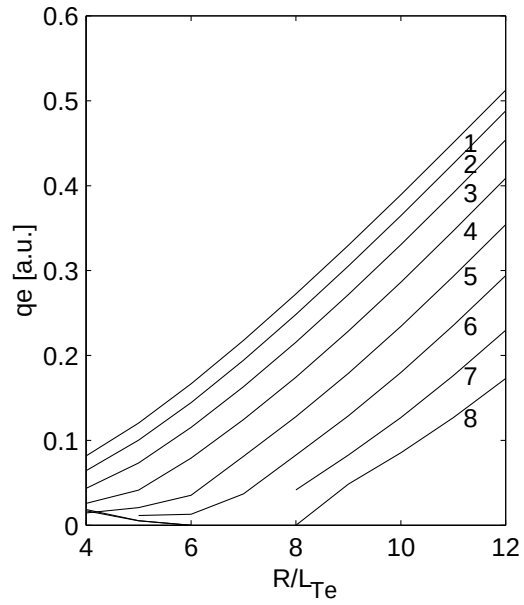

Figure 3.6: The quasi-linear heat flux in arbitrary units as a function of R/L_{Te} for different values of the collisionality $\nu_{eff} = (0.14, 0.26, 0.46, 0.83, 1.49, 2.67, 4.79, 8.60)$. The curves in the figure are numbered according to increased collisionality.

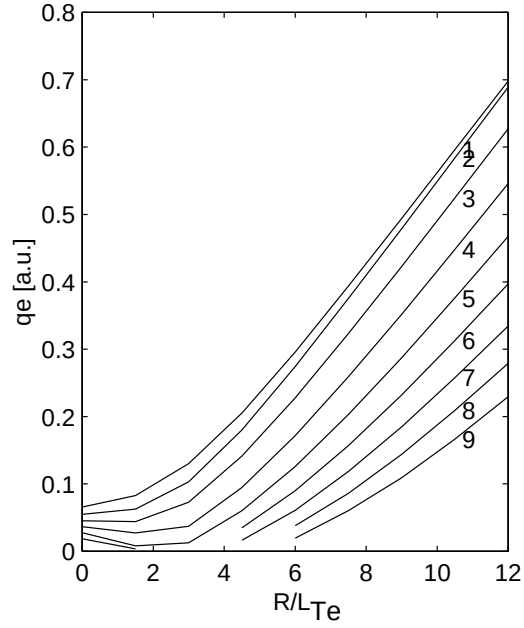

Figure 3.7: The quasi-linear heat flux in arbitrary units as a function of the magnetic shear $\hat{s} = (0.20, 0.43, 0.65, 0.88, 1.1, 1.33, 1.55, 1.78, 2.0)$. The curves in the figure have been numbered according to increasing shear.

The magnetic field topology enters the equations through the safety factor and magnetic shear. The heat flux as a function of R/L_{Te} is shown in figure 3.7 for different values of the magnetic shear. It can be seen that the magnetic shear has a stabilizing influence. Since the mode is a trapped electron mode, the parameters connected with the ions do not change the growth rate considerably. A scan on the ion temperature, ion temperature gradient length is shown in figures 3.8 and 3.4. Both quantities hardly change the growth rate of the mode (here calculated for $R/L_{Te} = 12$).

The ion temperature, Fig. 3.8, leads to a slight destabilization whereas its gradient, Fig. 3.4, is found to lead to a weak stabilization. The same effect has been found for the effective charge, which plays a role almost only through the collision frequency Fig 3.9, and electro-magnetic effects of the magnitude expected in these experiments Fig. 3.10.

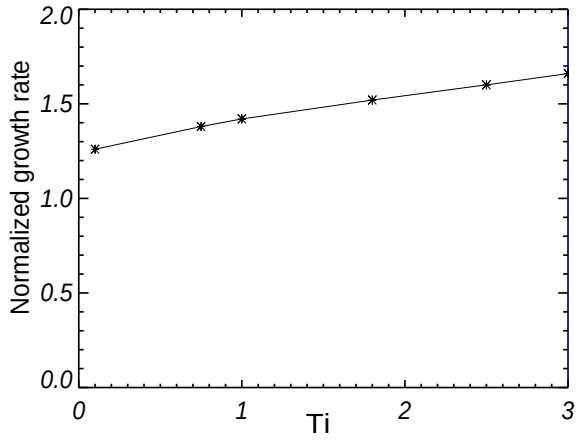

Figure 3.8: The normalized growth rate $\gamma R/v_{thi}$ as a function of the ion temperature T_i normalized to the standard value $T_i = 0.5$ keV.

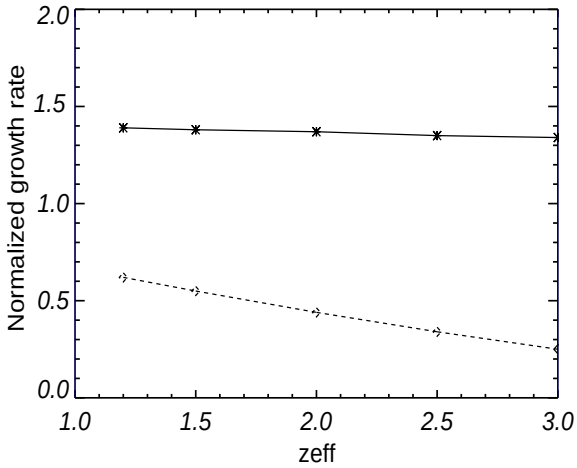

Figure 3.9: The normalized growth rate $\gamma R/v_{thi}$ as a function of Zeff. Without collisions (stars), with collisions (circles).

Figure 3.11 shows the dependence of the growth rate on the safety factor, which is found to be very small. It must be noted here that this dependence is in contrast to the observations mentioned in the introduction.

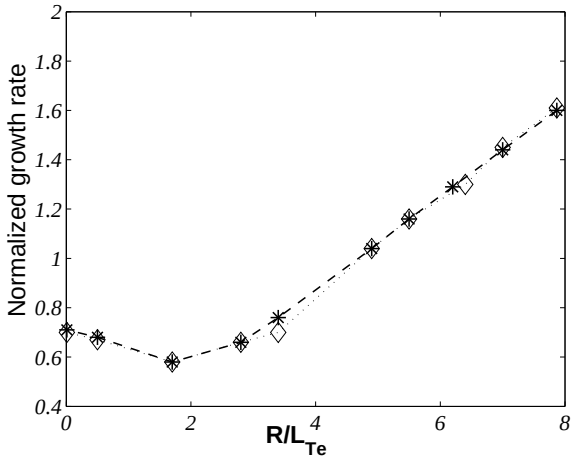

Figure 3.10: The normalized growth rate $\gamma R/v_{thi}$ vs R/L_{Te}. Without electromagnetic effects (stars), with electromagnetic effects (diamonds).

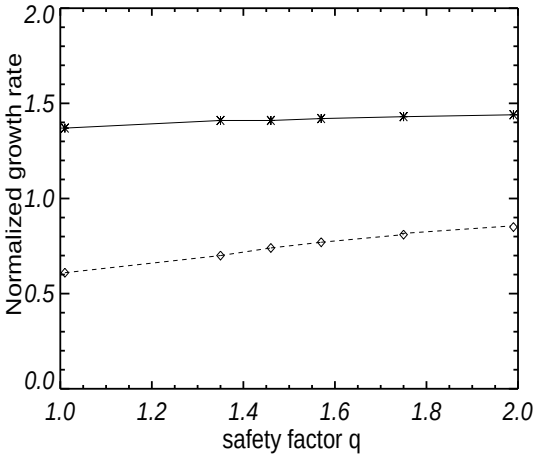

Figure 3.11: The normalized growth rate $\gamma R/v_{thi}$ vs the safety factor q. Without collisions (stars), with collisions (circles).

Generally, the transport coefficient is observed to increase with the safety factor to the power 1 to 2. It should be noted too that the discrepancy can not be explained over the magnetic shear dependence. The safety factor in experiments is increased through lowering the current, which enhances the shear in the confinement region, and should according to linear theory lead to a smaller growth rate, whereas a larger transport is observed in the experiments. One possible explanation could be that the density gradient, which is generally larger in low current plasmas gives more drive to the mode. This assumption, however, is not supported by the experimental data. The conclusion, therefore, is that the linear description is not complete. It was suggested [67] that the radial correlation length of the turbulence depends on the safety factor, an effect that is not reflected in the maximum growth rate. Non-linear simulations are needed to investigate this point.

3.3 Comparison with Weiland and GFL23 models

In order to consolidate the study of the dependence of the normalized growth rate $\gamma R/v_{thi}$ on different parameters two other theoretical transport models, the Weiland model [16] and the GLF23 model [68] have been considered. These two models are regularly applied for the heat transport modelling of tokamak plasmas and they adopt complementary approaches. In the following paragraphs we provide a general overview on the two models employed for our study.

3.3.1 The Weiland model

This is a fluid model based on ITG and TEM coupling. The most relevant approximations of the model are summarized as follows:

- The model uses the so-called strong ballooning approximation. This leads to a local dispersion relation with the quantities evaluated on the low field side.

- The closure of the fluid equation is obtained by taking the heat flux equal to the diamagnetic heat flux with isotropic temperature.

- In the version considered here (7 equations), electromagnetic effects are neglected. The ion parallel motion and shear effects are included, but their description is simplified.

- The background electrostatic field is assumed to be zero, except when considering the stabilizing term $\omega_{E\times B}$.

3.3.2 The GLF23 model

The GLF23 (Gyro-Landau Fluid) model is also based on the fluid equations [68]. However:

- The closure is different from that of the Weiland model. "The complex coefficients of these linear combinations [of the lower moments] are chosen to best fit the general kinetic plasma response function over the full range from small and large values in all the kinetic parameters: the gyroradius parameter $(k_\theta \rho_s)^2$; the parallel motion parameter $k_{||}c_s/\omega$; and the curvature drift parameter ω_D/ω_{ci}" ([69], pag. 3138).

- "The toroidal ion temperature gradient (ITG) mode, the collisionless to dissipative trapped electron drift modes, and the ideal magnetohydrodynamic (MHD) ballooning modes are included" ([68], pag. 2482).

- The model assumes a magnetic shear ($\hat{s}$) - Shafranov shift (α) stabilization. Landau damping is taken into account.

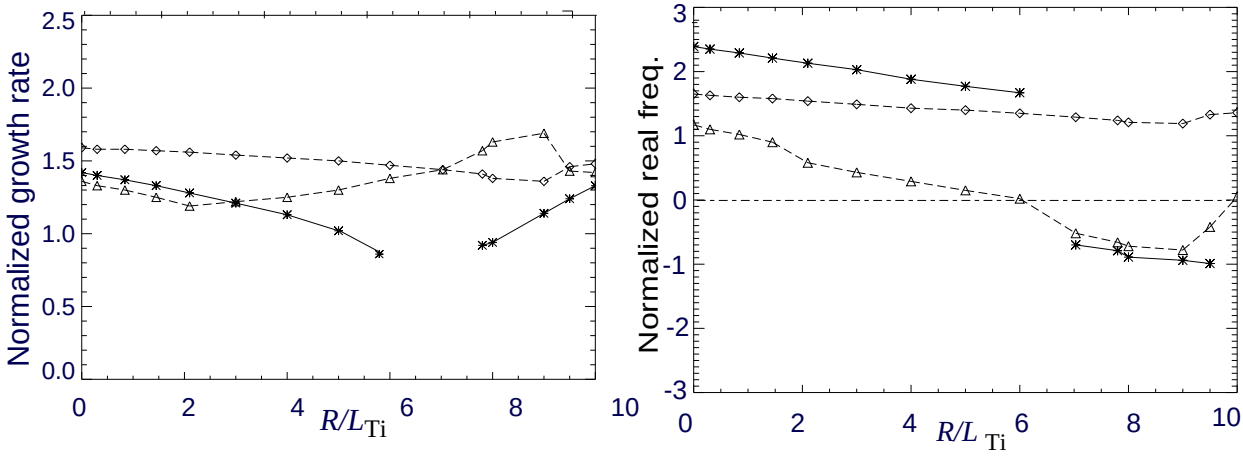

Figure 3.12: Comparison of GS2 model (stars) with Weiland model (diamonds) and GLF23 model (triangles): left: normalized growth rate vs R/L_{Ti}; right: normalized real frequency vs R/L_{Ti}.

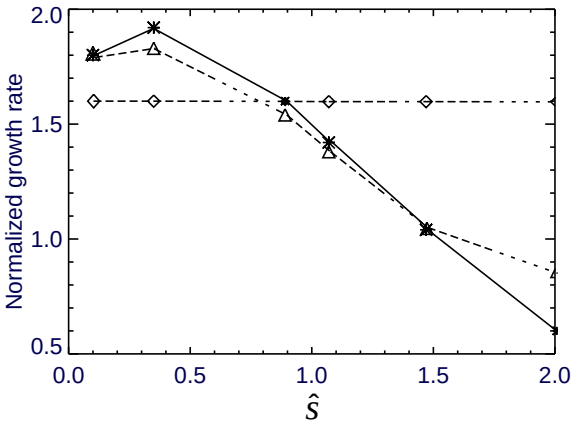

Figure 3.13: Normalized growth rate vs $\hat{s}$. Comparison between GS2 (stars), GLF23 (triangles) and Weiland (diamonds) models.

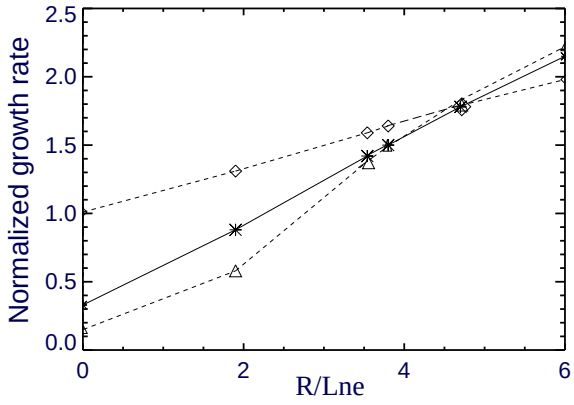

Figure 3.14: Normalized growth rate vs R/L_{ne}. Comparison between GS2 (stars), GLF23 (triangles) and Weiland (diamonds) models.

In this section the normalized growth rate ($\gamma R/v_{thi}$) and normalized frequency ($\omega R/v_{thi}$) of the three models will be compared. Again the standard set of parameters is used here and scans in all the relevant parameters have been made. The GS2 model is the most complete, and is thought to present the correct solution.

To test the transition from the TEM to ITG the ion temperature gradient has been varied with the results shown in Fig. (3.12). In the Weiland model no clear transition occurs, with the mode always rotating in the electron diamagnetic di-

rection. GLF23 on the other hand, behaves qualitatively correct. Nevertheless, frequency as well as the growth rate can show relatively large qualitative differences with GS2.

The well known stabilizing effect of the magnetic shear is also found in the GLF23, and is in very good qualitative agreement with GS2. The local approximations made in the Weiland model, however, almost completely eliminate the effect of the magnetic shear.

As shown in the previous section the density gradient has strong influence on the TEM. A comparison between the models for the growth rate is shown in Fig.3.14. It can be seen that for all models the growth rate increases as a function of R/L_n. The dependence is somewhat weaker for the Weiland mode.

In conclusion, the GLF23 model behaves qualitatively correct, and has a reasonable accuracy for the growth rate of the models. The Weiland model behaves less well.

3.4 Comparison with experiment

The ASDEX Upgrade tokamak (major radius R=1.65 m, minor radius a=0.5 m, elongation $\kappa \approx 1.6$) is equipped with an ECRH system consisting of four 140 GHz gyrotrons delivering each about 400 kW to the plasma. The scheme used is 2^{nd} harmonic X-mode which yields a narrow (about 3 cm) heating deposition profile with 100% single-pass absorption by the electrons only. Each of the four ECRH beams is injected into the plasma with an independent mirror launcher providing separate position steering of the deposition for each ECRH beam. The electron temperature is measured by the 60 channel Electron Cyclotron Emission heterodyne radiometer, which generally covers the whole plasma radius, with a distance between channels of 1 to 3 cm. It has a spatial resolution of about 1 cm for each channel and a bandwidth up to ≈ 32 kHz. The electron temperature is measured in addition by the Thomson scattering diagnostic with 16 radial channels, yielding a profile every 16 ms. These two diagnostics generally agree within $\pm 10\%$. The density profile is provided by Thomson scattering and by deconvolution of the interferometer.

The series of experiments with shot number #14793 until #14796, of which the steady state electron temperature profiles are shown in Fig. 3.1 were designed to test the electron stiffness and have been reported in [52]. The ECRH power was deposited at two locations, $\rho_1 \approx 0.35$ and $\rho_2 \approx 0.65$, with the respective intensities P_{ECRH1} and P_{ECRH2}. The powers were varied while keeping $P_{ECRH1} + P_{ECRH2}$ constant at about

1.3 MW which provides a constant edge temperature. In this way it was possible to separate the effect of the temperature and its gradient on the electron heat flux. The discharges were L modes in deuterium at low density, $\bar{n}_e = 2 \cdot 10^{19} m^{-3}$, to reduce the electron-ion energy transfer and provide good conditions to study the electron heat transport. A variation of $\nabla T_e/T_e$ by about a factor of 2 could be achieved in these experiments by varying the electron heat flux in the confinement region ($0.35 \leq \rho_{tor} \leq 0.65$) by one order of magnitude while keeping the heat flux at the plasma edge ($\rho_{tor} \geq 0.65$) constant.

The electron temperature and its gradient were obtained from the Electron Cyclotron Emission (ECE) diagnostic and has reasonably small error bars of around 10%. Density and its gradient are calculated from Thomson scattering with a sizeable error of 20%. The ion temperature is calculated from the neutral particle analyzer and is determined with an accuracy of ±20%. Its gradients is, therefore, not calculated and set to zero. The safety factor and magnetic shear are calculated from the equilibrium reconstruction, which however does not use internal q-profile measurements. Therefore, they have relatively large error bars (estimated to be around 20%). From the above it is clear that several quantities are quite inaccurately determined. However, most of the inaccurate quantities have a relatively weak influence on the growth rate, with the exception of the density gradient.

The comparison between the experimental data and the results from GS2 is carried out on the heat flux as follows. The experimental surface integrated heat flux q_e has been estimated by power balance at $\rho_t = 0.5$. Due to the low electron-ion coupling and to the well defined electron heating the values yielded by power balance are precise. The experimental results, shown in figure 3.15, indicated a clear increase of q_e with R/L_{Te} above a certain value of R/L_{Te}. The GS2 calculations have been done at the same radius taking into account the necessary experimental data. Because only the scaling and not the magnitude of the heat flux is determined, a scaling factor (1 free parameter, the same for all discharges) is chosen to overlay the experiment and the calculations. This calculated heat flux is also shown in figure 3.15.

The figure shows the results without collisions at the nominal experimental value of $R/L_{ne} = 3.5$, as well as the result with collisions for $R/L_{ne} = 3.7$. The latter value of R/L_{ne} makes the agreement between calculations and experiment slightly better and is well within the uncertainty of ±20% of R/L_{ne}. The agreement between the calculations and the experiments is surprisingly good considering the limitations of the modelling. As expected from the TEM stabilization by collisions, the points

without collisions are above those with collisions. (the slight increase of the density gradient has increased the growth rate and, therefore, works in the opposite direction as the collisions.) Of course an arbitrary scaling factor is used here, but the curve without collisions does not show a clear threshold, i.e. it can not be scaled on to the experimental results. We conclude that collisions are important in the description, especially when an accurate determination of the threshold is desired, and that they play a role even in relatively low density plasmas.

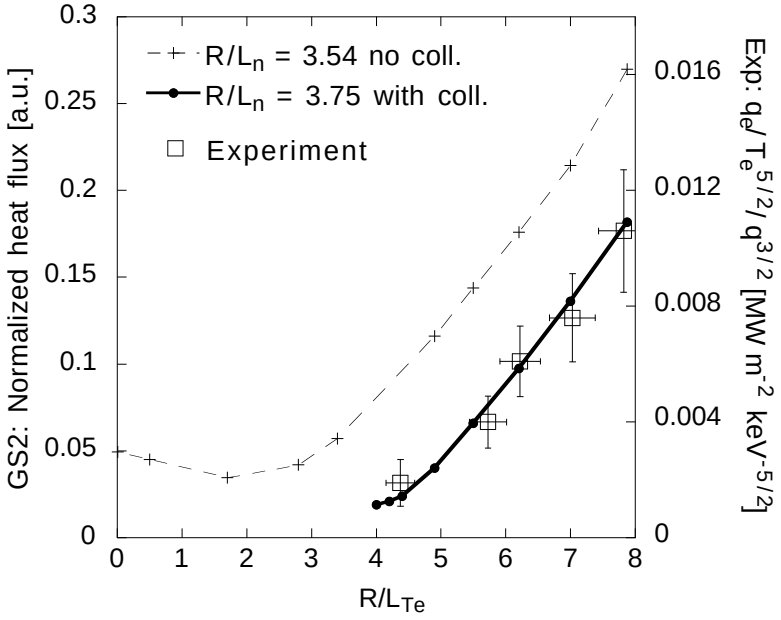

Figure 3.15: The electron temperature profiles for the different discharges in the series.

3.5 The empirical model

At this point it is useful to compare the results of the calculations with the empirical model proposed in [70] and extensively used in the literature [71, 52]

$$\chi_e = \chi_0 + \lambda T_e^{3/2} \left(\frac{1}{L_T} - \frac{1}{L_T}\bigg|_{crit} \right) H \left(\frac{1}{L_T} - \frac{1}{L_T}\bigg|_{crit} \right) \tag{3.2}$$

where H is the Heaviside function. The heat pulse diffusion coefficient, which determines the timescale for the propagation of the heat wave, can directly be derive from this equation to be

$$\chi_{HP} = \chi_e + \frac{\partial \chi_e}{\partial \nabla T} \nabla T = \chi_0 + \lambda T_e^{3/2} \left(\frac{2}{L_T} - \frac{1}{L_T}\bigg|_{crit} \right) \qquad 1/L_T > 1/L_{Tcrit} \quad (3.3)$$

This formula is often used to determine the parameters λ and L_{Tcrit} through a fit to the experimental data, allowing a direct comparison between the different experiments.

The formula indeed shows a strong resemblance with the calculations in this chapter. This, of course, because theoretical arguments were used to determine its functional form. There are nevertheless some differences worth noting. Obviously the form represents the electron heat transport in the region of sufficient high $\nabla T/T$. At low values of this quantity the mode can be entirely driven by the density gradient, and does not necessarily have a threshold. This is possibly not of such great importance since all experiments on ASDEX Upgrade, up to now, have been found to lie in the region of the parameters space in which the electron heat flux is strongly determined by $\nabla T/T$. Nevertheless, close to the threshold some differences can be expected.

Also for sufficient high electron temperature gradient the form of the heat transport suggested by our calculations is somewhat different from the empirical formula. From the figures above it can be seen that at sufficient large $\nabla T/T$ the heat flux increases linearly with $\nabla T/T$, whereas the empirical formula predicts a quadratic dependence (more accurately it has a linear as well as a quadratic contribution.) Although the data points agree well with the calculations, it turns out that the errors bar do not allow to distinguish between the two models.

3.6 Conclusion

In this chapter we have compared the experimentally observed electron heat transport with linear gyro kinetic stability calculations. The sensitivity scan around the parameters obtained from the experiment have revealed that the growth rate of the mode depends on several plasma parameters that are not usually considered when analyzing the experiments. Most clearly these are the density gradient and the collisionality. In the direct comparison of heat flux with the quasi-linear estimate a good agreement can only be obtained if these two effects are taken into account.

The direct comparison between the quasi-linear and experimentally observed heat flux shows a good agreement. It must be noted though that one free parameter (the saturation level of the turbulence) has been used in this comparison, i.e. one

can only compare the shapes of the curves. Also it must be noted that since the maximum linear growth rate and phase relation between temperature and potential fluctuation are used, the result is a quasi-linear result. Non linear effects such as the shift of the maximum amplitude in the spectrum towards larger scale lengths are not included.

The figure 3.15 explains many observations that have been made on the basis of empirical descriptions in the last decades. Both the experiments as well as the calculations show that a threshold for the TEM exists. The linear-offset relation of the heat flux also explains why the heat pulse propagates faster than what can be expected from the steady state heat conduction coefficient. Furthermore, the experiments can exceed the threshold by a factor two. The latter reflects a moderate stiffness of the electron channel. It must be noted here, that this is at least partly due to the relatively low electron temperature. Comparisons with the ion channel should be done carefully, because in many experiments in which the ion temperature profile is investigated, the ion temperature is larger. The effect of collisionality or density gradient might explain the coupling of the particle and electron heat channels as observed in the experiment, or the decrease of the heat pulse conductivity with increasing density, which are both mentioned in the introduction. Care is to be taken here though, because in general many parameters change simultaneously, and one would have to re-analyze the experiments using the results of the calculations presented in this chapter.

The normalized growth rate obtained from the gyro kinetic stability calculations have been also compared with Weiland and GLF23 models. A relative good agreement has been found between GS2 and GLF23 models, whereas the Weiland model performs less well (especially the shear dependence).

The comparison made with the empirical model have shown that the calculations presented in this chapter give in fact an easier functional form of the electron heat flux.

Despite the success of the comparison it should also be noted that not all properties can be explained. This is especially true for the dependence on the safety factor. It has been suggested that the widening of the spectrum in the non-linear state could account for such a dependence [67].

Chapter 4

Paraxial WKB method

4.1 Introduction

For solving the wave equation in the short-wavelength limit $k = L/\lambda \gg 1$, where L and λ are the typical inhomogeneity length and the wavelength of the medium under consideration, different asymptotic approaches are used in plasma physics. The ray method or geometrical optics is the most powerful and widespread in this sense. It uses an asymptotic expansion with respect to the small parameter k^{-1}. Further approach, which are based on asymptotic expansion with respect to small parameter $k^{-1/2}$ or $k^{-1/3}$, are available. Although these expansions results in more complicated description, they are able to reproduce wave characteristics that are not described in the ray method. In general, depending on the problem to be solved, the one or other type is more suitable and provides a better asymptotic approximation to the exact solution.

In spite of essential differences in various asymptotic expansions, the leading order for any of them results in description that is well known as the geometrical optics or the ray tracing. It is used in lots application of optics, seismology, physics of fluid and solids, quantum mechanics, plasma physics and many other fields [72], [73], [74]. The ray method uses an asymptotic expansion of the solution and reduces the wave equations to an infinite set of coupled equations for the successive terms of the expansion. The zero order therm is known as the *eikonal approach*. This order describes the phase behavior in space which is the most rapid variation of the wave field and it also gives rise to the ray or geometric-optics description. The first-order equation describes the field amplitude evolution along the ray trajectory, it has the important corollary that the *flux energy is directed along the rays*. In practice only the leading order equation and the consequence of the first order are mainly

used. This reduced approach is called the *ray tracing* or *geometrical optics method*. In many cases of practical interest this method provides the only possibility of obtaining a solution and for this reason it is widely used in plasma physic. However, in plasma (in contrast to conventional optics), use of the ray method is in most of the cases far from being really justified and sometimes clearly irrelevant. In fusion plasmas, geometrical optics fails very often even when the condition $\lambda \ll L$ is fulfilled with large margin. The reason for this failure is that this inequality provides only the necessary, but not sufficient, condition for applicability of geometrical optics. A breakdown of the applicability condition means that the diffraction phenomena, which are not taken into account by the geometrical optics, become significant.

The sufficient condition of applicability is known as Fresnel condition and in addition to $\lambda \ll L$, it imposes a limitation on width of the beam Λ. For instance, in homogeneous media the effect of diffraction can not be neglected if $\Lambda^2 \leq \lambda\ell$, where ℓ is the length of the propagation path. Hence, diffraction becomes important if ℓ is sufficiently large. If one takes $\ell \approx L$ (inhomogeneous media), diffraction effects are significant for $\Lambda \approx \sqrt{\lambda L}$.

In tokamak, even for highest frequency of electron cyclotron range, the Fresnel condition can be violated. The diffraction should be taken into account in the vicinity of focal points and caustics [75]. The diffraction could be also important in the lower-hybrid frequency range [76]. In case of the lower-hybrid wave the diffraction can be neglected only for the first wave pass along the minor radius. If complete absorbtion does not take place before the Fresnel condition breaks, then for the rest of the wave path in plasma, the field distribution is dominated by the diffraction phenomena. For ion cyclotron waves Fresnel condition is violated from the very beginning. In all cases, the violation results in wave energy flow not only along the ray tube, as in the ray approach, but also across the rays, causing wave packet and wave spectrum broadening.

The energy flow transverse to the rays appears also in the ray method, but only in higher-order terms of the asymptotic expansion. The higher order terms of the asymptotic expansion are very seldom used in practice because their complexity. Therefore, when the wave properties of propagation have to be included different asymptotic approaches are used. The wave properties of the propagating oscillations are studied as usual by the quasi-optic approach. The first approach was introduced more than 50 years ago as a parabolic equation technique by Fock and Leontovich [77]. The method was based on the reduction of the wave equation to an equation of Schrödinger type, being called parabolic equation. Another technique makes use

of a complex phase or eikonal [78]- [80] in order to get the set of (real) generalized wave equations in order to get diffraction effects. However, in this case also the final set of equations is a set of partially differential equations, thus losing one of the most attractive feature of the geometrical optics. Further advancement was made ([81], [82]) with the introduction of a new technique called *the paraxial Wentzel-Kramers-Brillouin (WKB)* or *beam tracing*.
Although based on the same physical assumptions as the method referred above, in the beam tracing approach Maxwell's equations are reduced to a set of first-order ordinary differential equations, thus recovering the most useful feature of geometrical optics. These equations give the evolution of the axis of the beam and a set of parameters connected with curvature of the phase front and with the amplitude profile. *The paraxial WKB* method includes the conventional ray tracing as a particular case, but it leads to a final set of equation which is different from that of some other methods. The approach combines the simplicity of ray tracing with description of the wave properties, diffraction and interference. The paraxial WKB method is also more suitable for numerical treatment due to the smaller number of equation that have to be solved in the paraxial WKB in comparison with the ray tracing method. Unlike the ray method, dealing with separate noninteracting rays, the paraxial WKB method treats entire wave packets of finite width and retains a description of the wave phenomena discarded in the ray method. This becomes possible because the paraxial WKB method incorporates nonlocal information on the refractive index in the vicinity of the central ray and enables one to judge the focusing and defocusing properties of the medium and thus the existence of the eigenfunctions in the neighborhood of the ray under examination.

4.2 Beam tracing method

4.2.1 Beam tracing equations

In the BT approach the solution of the wave equation for the electric field $\mathbf{E}$ is sought in the form

$$\mathbf{E}(\mathbf{r}) = e^{ik\bar{s}(\mathbf{r})}\left(\mathbf{a}(\mathbf{r}) - \frac{i}{k}\mathbf{c}(\mathbf{r})\right) = e^{ik[s(\mathbf{r})+i\phi(\mathbf{r})]}\left(\mathbf{a}(\mathbf{r}) - \frac{i}{k}\mathbf{c}(\mathbf{r})\right) \tag{4.1}$$

where the (supposed large) dimensionless parameter

$$k = \frac{L\omega}{c} \gg 1 \tag{4.2}$$

is introduced, L being the medium inhomogeneity scale, ω the wave frequency, and c the speed of light. The amplitude vector $\mathbf{a}$ and the *complex eikonal* $\bar{s}$ are functions of position $\mathbf{r}$. The phase of the wave $\bar{s}(\mathbf{r}) = s(\mathbf{r}) + i\phi(\mathbf{r})$ includes a real part, which has the same meaning as in the geometrical optics, and an imaginary part (*attenuation* function $\phi \geq 0$) connected with the description of the Gaussian field profile, in other words, with the transverse (with respect to the propagation direction) structure of the wave beam.

The underlying idea of the beam tracing method is that a wave beam is localized in the space around some axis, where the amplitude reaches its maximum, and, far away from the axis, the wave field is negligible. It is hence useless to know the wave field everywhere in space with the same accuracy, and Taylor expansion of the (complex) phase of the wave around the beam axis can be performed.

$$s(\mathbf{r}) = s_\alpha(\tau)\left[x^\alpha - q^\alpha(\tau)\right] + \frac{1}{2}s_{\alpha\beta}(\tau)\left[x^\alpha - q^\alpha(\tau)\right]\left[x^\beta - q^\beta(\tau)\right]$$

$$\phi(\mathbf{r}) = \frac{1}{2}\phi_{\alpha\beta}(\tau)\left[x^\alpha - q^\alpha(\tau)\right]\left[x^\beta - q^\beta(\tau)\right]$$

As in the geometrical optics, the short-wavelength limit condition equation (4.2) is supposed to hold. In addition, it is assumed that the beam width is ordered such that $\lambda \ll \Lambda \ll L$ (this is the case of typical experimental set-up). As was mentioned before, the diffraction effects become significant just in this limit.

The beam tracing equations are obtained by substituting equation (4.1) into the Maxwell's equation

$$\nabla \times (\nabla \times \mathbf{E}) - \frac{\omega^2}{c^2}\hat{\epsilon}\mathbf{E} = 0 \tag{4.3}$$

where $\nabla = \partial/\partial\mathbf{x}$, $\{\mathbf{x}\} = \{\mathbf{r}/L\}$ being a dimensionless laboratory, and $\hat{\epsilon}$ is the dielectric tensor. Similar to the geometrical optics, the case of weak absorbtion is considered and the dielectric tensor is considered in the form $\hat{\epsilon} = \hat{\epsilon}^H + ik^{-1}\hat{\epsilon}^A$ with $\hat{\epsilon}^H$ and $i\hat{\epsilon}^A$ being the Hermitian and an anti-Hermitian part respectively. Such representation artificially attributes the anti-Hermitian component to the second order of magnitude. From this substitution, a hierarchy of equation is obtained by grouping together terms containing the same power of k and equating them with zero. This gives in the lower and in the first order

$$\hat{\hat{\mathbf{L}}}\mathbf{a} = 0 \tag{4.4}$$

$$\hat{\hat{\mathbf{L}}}\mathbf{c} + \hat{\hat{M}}[\mathbf{a}] + \hat{\epsilon}^A\mathbf{a} = 0 \tag{4.5}$$

where the algebraic operator

$$\hat{\bar{\mathbf{L}}}\mathbf{e} \overset{def}{=} (\nabla\bar{s}\cdot\nabla\bar{s})\,\mathbf{e} - \nabla\bar{s}\,(\nabla\bar{\mathbf{s}}\cdot\mathbf{e}) - \hat{\epsilon}^{H}\mathbf{e} \tag{4.6}$$

and the differential operator

$$\hat{\bar{M}}\,[\mathbf{e}] \overset{def}{=} -\nabla\times(\nabla s\times\mathbf{e}) - \nabla s\times(\nabla\times\mathbf{e}) \tag{4.7}$$

are introduced. The obtained set of equations (4.4)-(4.5) is a linear algebraic system with respect to the unknown vectors $\mathbf{a}$ and $\mathbf{c}$.

4.2.2 Solvability condition

The solvability condition for equations (4.4) is

$$\bar{H} \overset{def}{=} det\left[\hat{\bar{\mathbf{L}}}\right] = 0. \tag{4.8}$$

It is useful to introduce the following notations:

$$\hat{\mathbf{L}}\mathbf{e} \overset{def}{=} (\nabla s\cdot\nabla s)\,\mathbf{e} - \nabla s\,(\nabla\mathbf{s}\cdot\mathbf{e}) - \hat{\epsilon}^{H}\mathbf{e},\;\; H \overset{def}{=} det\left[\hat{\mathbf{L}}\right] = 0 \tag{4.9}$$

where s is real, $\hat{L}$ is Hermitian and hence H is real. As is known, a real curve given by a set of equations

$$\frac{d\mathbf{x}}{d\tau} = \frac{\partial H}{\partial(\nabla s)},\;\; \frac{d(\nabla s)}{d\tau} = -\frac{\partial H}{\partial\mathbf{x}} \tag{4.10}$$

provides a solution to the equation $H(\nabla s,\mathbf{x}) = 0$. If $\phi\equiv 0$ then equation(4.8) is obviously satisfied along any solution of equations (4.10), while equation (4.1) is reduced to the conventional ray tracing. In what follows, we seek solution of the equation (4.8) with $\phi\neq 0$, but assume that, in the same point $\mathbf{x}_0$, $\phi(\mathbf{x}_0) = 0$. We take a solution of the equation (4.10) passing through the point $\mathbf{x}_0$. This characteristic will be called the *reference ray* and denoted by $\Re$.

The function ϕ, describing the Gaussian beam profile, is assumed now to have the form:

$$\phi = \frac{1}{2}\rho_{ij}(\tau)\,w^{i}w^{j} \tag{4.11}$$

Here and below, Einstein's summation is adopted and it is assumed that Latin indices take the values 1,2 and Greek indices values 1,2,3. A new reference frame, the *ray coordinates* system $\{\tau(\mathbf{x}), w^{1}(\mathbf{x}), w^{2}(\mathbf{x})\}$ can be introduced. We define it by requiring that $w^{j}(\mathbf{x})\,|_{\Re} = 0$. The coordinate τ is a parameter along the reference

ray. It can be assumed $\tau = \tau(s)$ and $s = s(\tau)$. The coordinate curve given by the equation $w^1(\mathbf{x}) = w^2(\mathbf{x}) = 0$ coincides with the reference ray $\Re$ and the relation

$$\nabla\phi \mid_{\Re} = 0 \tag{4.12}$$

is valid. It is immediately seen that, along the ray $\Re$, $\nabla\bar{s} = \nabla s$ and, therefore, $\bar{H} = H$. It follows that equation (4.8) is satisfied along the reference ray.

The quadratic form equation (4.11) is supposed to be positive definite, i.e, $\phi = 0$ if and only if $w^1 = w^2 = 0$. The function $e^{-k\phi}$ has its maximum on $\Re$, so that constitutes the "backbone" of the wave beam. It can be shown that

$$\left(w^1\right)^m \left(w^2\right)^n e^{(-1/2)k\rho_{ij}(s)w^i w^j} = \mathcal{O}\left(k^{-(m+n)/2}\right) \tag{4.13}$$

This means that in expanding any function containing the factor $exp(-k\phi)$ in powers of w^i around $w^1 = w^2 = 0$ only a few terms have to be retained, because the increasing in the power of w^i is equivalent to the transition to terms of higher order in $1/\sqrt{k}$. According to this, the ordering in half-integer powers of $1/k$ implied by equation equation (4.13) is employed to perform an expansion (*paraxial expansion*) of equation (4.8) around $\Re$.

An important remark has to be made here. After substitution of equation (4.1) in equation (4.3), those terms that contain the factor k^2 lead to equation (4.4) from which the beam tracing equation can be derived. From the terms containing the factor k, equation (4.5) results and it will be use to obtain the amplitude transport equation in the beam tracing approach.

It follows then that equation(4.4) has to be fulfilled with an accuracy of $\mathcal{O}(k)$. This means that is sufficient to replace equation (4.8) with $\bar{H} = \mathcal{O}(k)$, which in turn is equivalent to

$$\bar{H} \mid_{\Re} = 0 \tag{4.14}$$

$$\frac{\partial \bar{H}}{\partial w^i} \mid_{\Re} = 0 \tag{4.15}$$

$$\frac{\partial^2 \bar{H}}{\partial w^i \partial w^j} \mid_{\Re} = 0 \tag{4.16}$$

In order to achieve more compact equations, the following notation is introduced. The differentiation in respect to x^α is denoted by the Greek subscripts:

$$\bar{s}_\alpha \overset{def}{=} \frac{\partial \bar{s}}{\partial x_\alpha}, \quad \bar{s}_{\alpha\beta} \overset{def}{=} \frac{\partial^2 \bar{s}}{\partial x_\alpha \partial x_\beta} \tag{4.17}$$

while the total derivation in respect with x^α is indicated by the symbol ∂_α, so that for any function $f = f\left(\bar{s}_\beta\left(x^\alpha\right), x^\alpha\right)$,

$$\partial_\alpha f \stackrel{def}{=} \frac{\partial f}{\partial x_\alpha} + \frac{\partial f}{\partial \bar{s}_\beta}\bar{s}_{\alpha\beta} \tag{4.18}$$

From the relations

$$\partial_\alpha f = w^i_\alpha \frac{\partial f}{\partial w^i} + \tau_\alpha \frac{\partial f}{\partial \tau}, \quad \frac{\partial f}{\partial \tau} \mid_{\Re} = \frac{d}{d\tau}\left[f \mid_{\Re}\right] \tag{4.19}$$

along with equation(4.14), it follows

$$\partial_\alpha \bar{H} \mid_{\Re} = \left(w^i_\alpha \frac{\partial \bar{H}}{\partial w^i}\right) \mid_{\Re}, \tag{4.20}$$

$$\partial_{\alpha\beta} \bar{H} \mid_{\Re} = \left(w^i_\alpha w^j_\beta \frac{\partial^2 \bar{H}}{\partial w^i \partial w^j}\right) \mid_{\Re}, \tag{4.21}$$

Equations (4.14)-(4.16) then read

$$\bar{H} \mid_{\Re} = 0 \tag{4.22}$$

$$\partial_\alpha \bar{H} \mid_{\Re} = 0 \tag{4.23}$$

$$\partial_{\alpha\beta} \bar{H} \mid_{\Re} = 0 \tag{4.24}$$

It is understood from now on that all the quantities in the following equations have to be calculated on $\Re$. It has to be remarked that in the derivation equations (4.22)-(4.24) are a consequence of the paraxial expansion of equation (4.8) around the reference ray, or in the other words, of the ordering implied by equation (4.12). From the previous relations, one can derive a set of ordinary differential equations (beam tracing equations). Equations (4.22) and (4.23) give the equations for the reference ray $\Re$.

$$\frac{dq^\alpha}{d\tau} = \frac{\partial H}{\partial s_\alpha}, \quad \frac{ds_\alpha}{d\tau} = -\frac{\partial H}{\partial x^\alpha} \tag{4.25}$$

It has to be underline once again that on $\Re$ one has $\bar{s} = s$ and $\bar{H} = H$: this explain the notation of equation (4.24).

Equation (4.24) can be explicitly written as

$$\frac{d\bar{s}_{\alpha\beta}}{d\tau} + \frac{\partial^2 H}{\partial x^\alpha \partial x^\beta} + \frac{\partial^2 H}{\partial x^\beta \partial s_\gamma}\bar{s}_{\alpha\gamma} + \frac{\partial^2 H}{\partial x^\alpha \partial s_\gamma}\bar{s}_{\beta\gamma} + \frac{\partial^2 H}{\partial s_\gamma \partial s_\delta}\bar{s}_{\alpha\gamma}\bar{s}_{\beta\delta} = 0 \tag{4.26}$$

The real part of this complex unknown $s_{\alpha\beta}$ is related with the curvature of the phase front, while the imaginary part $\phi_{\alpha\beta} = \rho_{ik} w^i_\alpha w^j_\beta$ describes the beam profile. Equation (4.26) can be split into two real equations,

$$\frac{ds_{\alpha\beta}}{d\tau} + \frac{\partial^2 H}{\partial x^\alpha \partial x^\beta} + \frac{\partial^2 H}{\partial x^\beta \partial s_\gamma} s_{\alpha\gamma} + \frac{\partial^2 H}{\partial x^\alpha \partial s_\gamma} s_{\beta\gamma} + \frac{\partial^2 H}{\partial s_\gamma \partial s_\delta} s_{\alpha\gamma} s_{\beta\delta} = \frac{\partial^2 H}{\partial s_\gamma \partial s_\delta} \phi_{\alpha\gamma} \phi_{\beta\delta} \quad (4.27)$$

and

$$\frac{d\phi_{\alpha\beta}}{d\tau} + \left(\frac{\partial^2 H}{\partial x^\alpha \partial s_\gamma} + \frac{\partial^2 H}{\partial s_\gamma \partial s_\delta} s_{\alpha\delta} \right) \phi_{\beta\gamma} + \left(\frac{\partial^2 H}{\partial x^\beta \partial s_\gamma} + \frac{\partial^2 H}{\partial s_\gamma \partial s_\delta} s_{\beta\delta} \right) \phi_{\alpha\gamma} = 0 \quad (4.28)$$

An important remark is that the set of equations (4.27) and (4.28) formally includes nine equations for $s_{\alpha\beta}$ and nine for $\phi_{\alpha\beta}$ but they are not independent: the symmetry of $s_{\alpha\beta}$ and $\phi_{\alpha\beta}$ and the six constrains

$$s_{\alpha\beta} \frac{dx^\beta}{d\tau} + \frac{\partial H}{\partial x^\alpha} = 0 \quad (4.29)$$

$$\phi_{\alpha\beta} \frac{dx^\beta}{d\tau} = 0 \quad (4.30)$$

have to be taken into account. The first of these two equations is a consequence of the second equation (4.25) and the second one comes from

$$\frac{\partial w^i}{\partial \tau} = 0 = w^i_\alpha \frac{\partial H}{\partial s_\alpha} \quad (4.31)$$

4.2.3 Equation for the wave amplitude

The only quantity not defined yet in equation (4.1) is $a(\mathbf{r}) = A(\mathbf{r})\mathbf{e}$, with $\mathbf{e}^\star \cdot \mathbf{e} = 1$. A($\mathbf{r}$) is the wave amplitude and $\mathbf{e}$ is the polarization vector. We find the wave amplitude A($\mathbf{r}$) from a solvability condition for equation (4.5) in respect with the unknown vector $\mathbf{c}$. To find the solvability condition for the equation (4.5) Fredholm alternative is applied.
This yields

$$\mathbf{e}^\star \left\{ \hat{M}[\mathbf{a}] + \hat{\epsilon}^A \mathbf{a} \right\} = \mathbf{e}^\star \hat{M}[A\mathbf{e}] + A\mathbf{e}^\star \hat{\epsilon}^A \mathbf{e} = 0 \quad (4.32)$$

Using equation(4.7) one obtains

$$\mathbf{e}^\star \hat{M}[A\mathbf{e}] = A\mathbf{e}^\star \hat{M}[\mathbf{e}] + \mathbf{V} \cdot \nabla A, \quad (4.33)$$

where the contravariant components of vector $\mathbf{V}$are given by

$$V^{\alpha} = \mathbf{e}^{\star} L^{\alpha} \mathbf{e} = \mathbf{e}^{\star} \frac{\partial L}{\partial s^{\alpha}} \mathbf{e} = \frac{\partial H}{\partial s^{\alpha}} \tag{4.34}$$

The last relation in equation (4.34) follows from the equation $\hat{L}^{\alpha}\mathbf{e} + \hat{L}\mathbf{e}^{\alpha} = H^{\alpha}\mathbf{e} + H\mathbf{e}^{\alpha}$, which by virtue of $\mathbf{e}^{\star} \cdot \mathbf{e} = 1$ gives the identity

$$\mathbf{e}^{\star}\hat{L}^{\alpha}\mathbf{e} = -\mathbf{e}^{\star}\hat{L}\mathbf{e}^{\alpha} + H^{\alpha}\mathbf{e}^{\star} \cdot \mathbf{e} + H\mathbf{e}^{\star} \cdot \mathbf{e}^{\alpha} = H^{\alpha} - \mathbf{e}^{\star}H\mathbf{e}^{\alpha} + \mathbf{e}^{\star}\hat{L}\mathbf{e}^{\alpha} = H^{\alpha} \tag{4.35}$$

The equation for wave amplitude A($\mathbf{r}$) now reads

$$\mathbf{V} \cdot \nabla A + A\left\{\mathbf{e}^{\star}\hat{M}\left[\mathbf{e}\right] + \gamma\right\} = 0 \tag{4.36}$$

with γ determined by

$$\gamma = \mathbf{e}^{\star}\epsilon^{A}\mathbf{e}. \tag{4.37}$$

It is important to mention here that equations (4.32) and (4.36), are evaluated on the reference ray $\Re$ only. The equation (4.36), including the unknown function A, depend on the single variable τ. Making use of equation (4.25), we write equation (4.36) in the form

$$\frac{dA}{d\tau} + A\left\{\mathbf{e}^{\star}\hat{M}\left[\mathbf{e}\right] + \gamma\right\} = 0 \tag{4.38}$$

Another form of the equation(4.38) can be obtained by employing the property

$$\mathbf{e}^{\star}\hat{M}\left[\mathbf{e}\right] + \mathbf{e}\hat{M}\left[\mathbf{e}^{\star}\right] = \nabla \cdot \mathbf{V} \tag{4.39}$$

which can be proved by direct calculation. Combining equation (4.38) with its complex conjugate, one obtain the differential equation for the wave amplitude

$$\frac{d \mid \mathbf{A} \mid^2}{d\tau} + \mid \mathbf{A} \mid^2 \nabla \cdot \mathbf{V} = -2\gamma \mid \mathbf{A} \mid^2 \tag{4.40}$$

For numerical calculation, it could be useful to represent $\nabla \cdot \mathbf{V}$, making use of identity (4.2.34), which on the reference ray gives

$$\nabla \cdot \mathbf{V} = \frac{1}{\sqrt{g}} \frac{\partial}{\partial x^{\alpha}} \left(\sqrt{g} \frac{\partial H}{\partial s^{\alpha}}\right) = \frac{1}{\sqrt{g}} \frac{d\sqrt{g}}{d\tau} + \frac{\partial^2 H}{\partial q^{\alpha} \partial k_{\alpha}} + \frac{\partial^2 H}{\partial k_{\alpha} \partial k_{\alpha}} K_{\alpha\beta} \tag{4.41}$$

with $\sqrt{g}$ being the Jacobian of transformation from the Cartesian coordinates to the curvilinear coordinates $\{x^{\alpha}\}$.

Represented in the form associated with the energy conservation low, equation(4.40) becomes

$$\nabla \cdot \left(\mid \mathbf{A} \mid^2 \mathbf{V}\right) = -2\gamma \mid \mathbf{A} \mid^2 . \tag{4.42}$$

4.3 Ballooning Representation (BR)

4.3.1 Description of the method

From studies of simple configurations it has been known that some of the most persistent instabilities, in the investigation of the stability of a plasma confined by magnetic fields, are those with long wave length parallel to the magnetic field and short wave length perpendicular to it. (These characteristics minimize the stabilizing influence of the magnetic field). However, in toroidal magnetic field with shear (that is when the rotational transform varies from surface to surface) those characteristics conflict with the requirement that the perturbation be periodic in both toroidal and poloidal directions. The first problem in the investigation of stability was therefore that of reconciling long parallel wavelength, short perpendicular wave length and periodicity. One successful attempt for solving the periodicity difficulty was dealt with by using the "ballooning representation" method, described by Connor, Hastie and Taylor [83] and it was further developed by Dewar and Glasser for application to three-dimensional geometry .
In any axisymmetric system the calculation of linear drift wave eigenmodes can be reduced (after Fourier transform decomposition $\sim e^{in\zeta}$, ζ is the angle around the symmetry axis) to a two dimensional eigenvalue problem

$$\mathcal{L}(\vartheta, x)\phi(\vartheta, x) = \lambda\phi(\vartheta, x) \tag{4.43}$$

where ϑ represents the poloidal angle and x is the flux surface coordinate. The operator $\mathcal{L}$ is periodic in ϑ, $0 \leq \vartheta \leq 2\pi$ and ϕ must be periodic in ϑ and bounded in x.

Since drift waves are characterized by short perpendicular and long parallel wavelengths, a natural representation for the perturbed quantities would be in an eikonal form

$$\phi(\vartheta, x) = F(\vartheta, x)e^{inS(\vartheta,x)} \tag{4.44}$$

with the toroidal mode number n$\gg$1 and both $F(\vartheta, x)$ and $S(\vartheta, x)$ varying on the equilibrium scale. The long parallel wavelength requires $\vec{B} \cdot \nabla(\zeta + S) = 0$, but such a representation violates the periodicity constraints in the poloidal direction ϑ. Therefore, it was introduced the transformation

$$\phi(\vartheta, x) = \Sigma_m e^{-im\vartheta} \int_{-\infty}^{\infty} e^{im\eta}\hat{\phi}(\eta, x)d\eta \tag{4.45}$$

By direct substitution of the transformation (4.45) in (4.43) it can be seen that any $\hat{\phi}(\eta, x)$ which is a solution of

$$\mathcal{L}(\vartheta, x)\hat{\phi}(\vartheta, x) = \lambda\hat{\phi}(\vartheta, x) \tag{4.46}$$

in the infinite domain $-\infty < \eta < +\infty$ will generate a periodic solution $\phi(\vartheta, x)$ of (4.43) with the same eigenvalue. Actually, all the relevant periodic solutions of (4.43) can be obtained from the eigenfuntions of (4.46).

This takes the problem from the periodic domain $0 \leq \vartheta \leq 2\pi$ into the infinite domain $-\infty < \eta < +\infty$, with the same eigenvalue. The operator for this problem is the same with that in the real problem so that properties such as short perpendicular and long parallel wavelength retain their importance. The point of the transformation is that, because it does not have to be periodic, $\hat{\phi}(\eta, x)$ (unlike $\phi(\vartheta$,x)) can be represented in an eikonal form $F(\eta, x)e^{inS}$ with the amplitude $F(\eta, x)$ slowly varying compared to the phase function. The amplitude $F(\eta, x)$ can be calculated as an expansion in power of 1/n. The lowest order of the expansion F satisfies an ordinary differential equation in the η coordinate alone while variation of F with x is determined by higher order equation. In lowest order the oscillations of each magnetic surface are decoupled and a local eigenvalue is obtained. The lowest order theory therefore defines a local oscillation frequency and fixes the structure of the mode along the magnetic field. The lowest order theory does not determine the structure of the mode transverse to the magnetic surfaces. This transverse structure, and the relation of the local oscillation frequency to the true frequency, are determined in higher orders of the expansion. This higher order theory shows that unstable modes are localized in the vicinity of the surface with the smallest local eigenvalue, that the true eigenvalue is close to the lowest local eigenvalue and that the most unstable high n modes occur for $n \longrightarrow \infty$.

Although the higher order theory is necessary to complete the solution, this solution itself can be expressed entirely in terms of quantities calculated from the lower order theory. Consequently the lowest order theory alone is sufficient to determine the stability.

The ballooning transformation was initially developed for calculation of magneto hydrodynamic ballooning modes, being later applied also to the drift modes.

4.3.2 Relation of pWKB with the Ballooning Representation

The pWKB and ballooning representation solutions, even if they are different in some respect, they have many similar features. This similarity has fundamental basis. Both approaches search for the same solution in form of asymptotic expansion with respect of the same parameter $(\lambda/L)^{-1/2}$. Therefore they would coincide if they didn't use additional simplifications. Actually, the coincidence is not complete because both technics are aimed to deal with ordinary differential equations, but in order to achieve this goal, they omit different terms. The ballooning representation discard any radial variation in plasma parameters in the leading order. In the higher order, BR allows for a radial dependence ([84], [83]), but it is treated as a correction of order 1/n. The pWKB method is free of this assumption, but it has restriction due to the paraxial expansion.

A common simplified reduction of the BR approach, which allows one to treat equations similar with equation (4.4) analytically, is the so called strong ballooning limit ([84], [85]). This simplification is equivalent with the paraxial expansion in the variable ϑ. In this limit, if there is no radial dependence both approaches coincide. In the presence of a radial dependence, BR fails, while pWKB nevertheless provides a solution.

The higher orders of the BR scale the radial dependence of the wave field as 1/n. It is also good to mention here that this assumption is much more restrictive then the paraxial assumption, which requires slow variation of the equilibrium medium parameters rather than the perturbed wave field.

In particular, scaling radial field dependence as 1/n, limits the BR to the case $\bar{k_\rho}$=0. (Here $\bar{k_\rho}$ is understood as an average radial wave number of a mode.) A physical requirement is a vanishing radial component of the group velocity $v_{gr,\rho}$=0, rather then of the phase velocity k_ρ=0. If $v_{gr,\rho}$=0 occurs at $k_\rho \neq 0$, then such a mode can not be properly described by BR technique. The BR presumes $k_{||} = \mathcal{O}(n^{-1/2})$ and can therefore describe the eigenmodes with $k_{||} \approx 0$.

In comparison, pWKB does not involve any preliminary assumption concerning the wave number of the solution. The proper field dependence is obtained here as a result of a standard procedure. Moreover, the pWKB technique allows arbitrary spatial dependence (although slow enough). It can be applied directly to the general dispersion relation without any other simplification. pWKB fails is the plasma parameters vary to much on the width of the eigenmode. As a conclusion the two

approaches are complementary. Depending on the problem under consideration, one technique is more suitable than the other and should be used for the stability analysis.

4.4 Our Model

In Chapter 2 we have already introduced the ion temperature gradient (ITG) turbulence which is driven by density and temperature gradients. The mechanism that leads to ITG turbulence and one dispersion relation that describes it has been already introduced there. The dispersion relation derived in chapter 2 neglects an essential term, the term which includes the wave vector in the parallel direction $k_{||}$. In this section we solve again the wave equation for ITG mode, this time considering also $k_{||}$. The paraxial WKB or beam tracing method is used for this purpose. As it was already stressed, the beam tracing method has much larger applicability because it takes into account the wave phenomena not described by some other technics. Also, it reduces the full wave equation to a set of ordinary differential equations allowing efficient numerical methods.

4.4.1 Description of BT application to eigenmodes, stability analysis

In our case the beam tracing method is applied to the problem of plasma stability, an eigenvalue problem. This means that we face a boundary value problem.

A necessary condition to construct an eigenmode of a plasma resonator is the existence of a closed ray trajectory. All the trajectories passing through a selected point $\mathbf{r}_0$ with the coordinates $\mathbf{r}_0 = \{q_0^\alpha\}$ are considered. After a nonzero path in the medium, some of the trajectory return to the same point, obtaining in this way a closed ray. In the beam tracing method the eigenfunctions are constructed as patterns located in the vicinity of the closed ray trajectory.

Only stable trajectories give rise to eigenmodes. So that, we are interested only in those trajectories which, in the course of further propagation will repeat the same path as at the first loop. This requires that the ray in question starts at point $q^\alpha(\tau_0) = q_0^\alpha$ with the wave vector $\mathbf{k}_0 = \{k_\beta(\tau_0)\}$ such that

$$D(\mathbf{r}_0, \mathbf{k}_0, \omega_0) = 0 \tag{4.47}$$

and arrives at the same point with the same set of six quantities:

$$q^\alpha(\tau_1) = q^\alpha(\tau_0), \;\; k_\alpha(\tau_1) = k_\alpha(\tau_0) \tag{4.48}$$

with $\tau_1 \neq \tau_0$. Similar condition can be imposed on the quantities

$$\bar{s}_{\alpha\beta}(\tau_1) = \bar{s}_{\alpha\beta}(\tau_0) \tag{4.49}$$

and on the amplitude function

$$|A(\tau_1)| = |A(\tau_0)|. \tag{4.50}$$

If the last three equations, (4.48-4.50) are fulfilled then the wave amplitude $|\Phi(r)|$ in the vicinity of point $\mathbf{r}_0$ is exactly the same, regardless of whether it is calculated at $\tau = \tau_0$ or at $\tau = \tau_1$. The loop along the closed trajectory can be repeated arbitrary many times as long as the quantities q^α, k_α, $\bar{s}_{\alpha\beta}$, $|A|$ satisfy the first order differential equation. Additionally, in order to make the phase Φ of the field single value, we require also

$$\Phi(r)|_{r=\{q^\alpha(\tau_1)\}} = e^{is_0(\tau_1)+i\tilde{s}(\tau_1)}\Phi(r)|_{r=\{q^\alpha(\tau_0)\}} \tag{4.51}$$

Considering the correction $\tilde{s}(\tau_1) = O(\lambda/L)$ small one obtain the quantization condition

$$s_0(\tau_1) = \int_0^\tau k_\alpha \frac{\partial D}{\partial k_\alpha} d\tau = 2\pi n \tag{4.52}$$

where $n \gg 1$ is an integer number.

These equations show that the eigenmodes are localized in a small vicinity of the closed ray trajectory, which is called also the reference ray or the basis contour. The electric field decay exponentially, while the differences from the basis contour increases. The decay is due to the positive definiteness of the quadratic form ϕ. If the length of the decay is shorter than the distance from the basis contour to the resonator boundary, the boundary influence is exponentially small and can be neglected. No further boundary condition is needed in this case.

Because we are interested in the stability of eigenmodes in a toroidal device, the eigenmode can be thought of as a wave propagating in the toroidal direction. The eigenmode axis is purely toroidal while the mode amplitude exponentially decays both in radial and poloidal directions. The wave interaction with the plasma defines whether such a mode absorbs or releases energy.

4.4.2 Formulation of the problem

In order to proceed with our calculation the first thing to do is to write the set of equations that describes the ITG in a more convenient form for us. In fluid description, as we have already seen in the second chapter, the basic set of equations

necessary to describe the ITG turbulence consists of the ion continuity (2.32) and energy equations (2.34). Because we want to get a more complete description of the ITG mode, we are not going to do any simplification of the equations, so that deriving our beam tracing equations the term containing the parallel velocity is going to be kept in the continuity equation. After replacing equations (B.5) in the continuity equation (2.32) and the ion heat flux given by equation (2.35) in the energy equation (2.34) we get

- Continuity equation:

$$\hat{C}_{11}\frac{e\phi}{T_0} + \hat{C}_{12}\frac{\tilde{p}_i}{p_0} + \frac{\tilde{n}_i}{n_0}\frac{n_0}{n_i} = 0 \tag{4.53}$$

- Energy equation:

$$\hat{C}_{21}\frac{e\phi}{T_0} - \frac{T_i n_0}{T_0 n_i}\frac{\tilde{n}_i}{n_0} + \hat{C}_{24}\frac{\tilde{T}_i}{T_0} = 0 \tag{4.54}$$

where the differential operators $\hat{C}_{11}$, $\hat{C}_{12}$, $\hat{C}_{21}$ and $\hat{C}_{24}$ are written explicitly

- $\hat{C}_{11} = \{ -\frac{i}{\omega}\vec{v}_{\star 0}\cdot\nabla + \frac{i}{\omega}\vec{v}_{D0}\cdot\nabla - \frac{1}{n_i}\nabla_\perp\cdot\left[\frac{c_0^2 n_i}{\omega_{ci}^2}\nabla_\perp\right] + \frac{c_0^2}{\omega^2}\nabla_{||}^2 \}$
- $\hat{C}_{12} = \frac{n_0}{n_i}\{ \frac{i}{\omega}\vec{v}_{D0}\cdot\nabla - \nabla_\perp\cdot\left[\frac{c_0^2}{\omega_{ci}^2}\nabla_\perp\right] + \frac{c_0^2}{\omega^2}\nabla_{||}^2 \}$
- $\hat{C}_{21} = -\frac{3}{2}\frac{i}{\omega}\frac{T_i}{T_0}\left[\eta_i - \frac{2}{3}\right]\vec{v}_{\star 0}\cdot\nabla,\ \ \hat{C}_{24} = \left(\frac{3}{2} + \frac{5i}{2\omega}\vec{v}_{Di}\cdot\nabla\right)$

Here c_0, ρ_0, $\vec{v}_{D0}$, $\vec{v}_{Di}$, $\vec{v}_{\star 0}$, have been all introduced explicitly in the appendix B, equation (B.4).

In comparison with Chapter 2 where Boltzmann electrons were considered, here the perturbed density is approximated by non-adiabatic trapped electron response that we write as

- non-adiabatic behaviour:

$$\frac{T_0}{T_e}(1 - i\delta)\frac{e\phi}{T_0} - \frac{n_0}{n_i}\frac{\tilde{n}_i}{n_0} = 0 \tag{4.55}$$

$i\delta = i\epsilon^{3/2}(\omega_{\star e}\eta_e/\nu_{ei})$ with ν_{ei} being the electron-ion Coulomb collision frequency. We write also

- pressure perturbation:

$$\frac{\tilde{p}_i}{p_0} - \frac{T_i}{T_0}\frac{\tilde{n}_i}{n_0} - \frac{n_i}{n_0}\frac{\tilde{T}_i}{T_0} = 0 \tag{4.56}$$

In the above set of equations $p_0 = n_0 T_0$, $n_0 = const$ and $T_0 = const$ were introduced to make the calculations simpler.
Defining the dimensionless perturbations

$$\hat{\phi} = \frac{e\phi}{T_0},\ \hat{p}_i = \frac{\tilde{p}_i}{p_0},\ \hat{n}_i = \frac{\tilde{n}_i}{n_0},\ \hat{T}_i = \frac{\tilde{T}_i}{T_0},$$

the present set of equations (4.53-4.56) can be regarded as a homogeneous set of four differential equations for four unknowns, $\hat{\phi}$, $\hat{p}_i$, $\hat{n}_i$, $\hat{T}_i$. In the matrix form the wave equation that describe the ITG turbulence reads as:

$$\begin{pmatrix} \hat{C}_{11} & \hat{C}_{12} & \frac{n_0}{n_i} & 0 \\ \hat{C}_{21} & 0 & -\frac{n_0}{n_i} & \hat{C}_{24} \\ 0 & \frac{T_0 n_0}{T_i n_i} & -\frac{n_0}{n_i} & -\frac{T_0}{T_i} \\ \frac{T_0}{T_e} & 0 & -\frac{n_0}{n_i} & 0 \end{pmatrix} \begin{pmatrix} \hat{\phi} \\ \hat{p}_i \\ \hat{n}_i \\ \hat{T}_i \end{pmatrix} = 0 \tag{4.57}$$

The equation (4.57) is equivalent with the equation (4.3) from the general description of the pWKB approximation. In what follows, the technique described in the beginning of this chapter, the paraxial WKB approximation, is applied in order to reduce the equation (4.57) to a set of ordinary differential equations.

4.4.3 Beam tracing equations in case of ITG mode

We choose the solution of equation (4.57) in the form

$$\begin{pmatrix} \hat{\phi} \\ \hat{p}_i \\ \hat{n}_i \\ \hat{T}_i \end{pmatrix} = e^{ikS} \left[\overbrace{\begin{pmatrix} \phi_1 \\ p_1 \\ n_1 \\ T_1 \end{pmatrix}}^{X_1} - \frac{i}{k} \overbrace{\begin{pmatrix} \phi_2 \\ p_2 \\ n_2 \\ T_2 \end{pmatrix}}^{X_2} \right] \tag{4.58}$$

where k is the pWKB expansion parameter. On substitution of equation (4.58) in equation (4.57), one obtains

$$\mathcal{L}X_1 - \frac{i}{k}\mathcal{L}X_2 - \frac{i}{k}\mathcal{M}X_1 = 0 \tag{4.59}$$

If we define $\vec{k}(\vec{r}, t) = \nabla S$ the two matrices, $\mathcal{L}$ and $\mathcal{M}$, in the equation (4.59) are written as

$$\mathcal{L} = \begin{pmatrix} \left(\vec{K} + \vec{K}_\star - \vec{K}_D\right)\cdot\vec{\varkappa} & \frac{n_0}{n_i}\left(\vec{K} - \vec{K}_D\right)\cdot\vec{\varkappa} & n_0/n_i & 0 \\ \left(\frac{3}{2}\eta_i - 1\right)\vec{K}_{\star 0}\cdot\vec{\varkappa} & 0 & -n_0/n_i & \frac{T_0}{T_i}\left(\frac{3}{2} - \frac{5}{2}\vec{K}_{Di}\cdot\vec{\varkappa}\right) \\ 0 & T_0 n_0/T_i n_i & -n_0/n_i & -T_0/T_i \\ T_0/T_e & 0 & -n_0/n_i & 0 \end{pmatrix}. \tag{4.60}$$

with

$$\vec{\varkappa} = \frac{c_0\vec{k}}{\omega},\ \ \vec{K} = \frac{\omega^2}{\omega_{ci}^2}\vec{\varkappa}_\perp - \vec{\varkappa}_{||},\ \ \vec{K}_D = \frac{\vec{v}_{D0}}{c_0},\ \ \vec{K}_{Di} = \frac{\vec{v}_{Di}}{c_0},\ \ \vec{K}_\star = \frac{\vec{v}_{\star 0}}{c_0}$$

$$\mathcal{M} = \left(\frac{\partial\mathcal{L}}{\partial\vec{k}}\cdot\nabla\right) + \frac{c_0}{\omega}\left(\nabla\cdot\vec{K}\right)\begin{pmatrix} 1 & \frac{n_0}{n_i} & 0 & 0 \\ 0 & 0 & 0 & 0 \\ 0 & 0 & 0 & 0 \\ 0 & 0 & 0 & 0 \end{pmatrix} + \begin{pmatrix} \frac{c_0}{\omega}\vec{K}\cdot\frac{\nabla n_i}{n_i} & 0 & 0 & 0 \\ 0 & 0 & 0 & 0 \\ 0 & 0 & 0 & 0 \\ -\delta\frac{T_0}{T_e} & 0 & 0 & 0 \end{pmatrix} \tag{4.61}$$

The equation (4.59) is fulfilled with an accuracy of $\mathcal{O}(k^{-3/2})$ if coefficients at higher powers of k are equated with zero.

$$\mathcal{L}X_1 = 0 \tag{4.62}$$

$$\mathcal{L}X_2 + \mathcal{M}X_1 = 0 \tag{4.63}$$

As it could be noticed the equation (4.62) is an algebraic while the equation (4.63) is still a differential equation. A solution of the linear algebraic system (4.62) is determined to within a coefficient A and it is sought in the form

$$\overbrace{\begin{pmatrix} \phi_1 \\ p_1 \\ n_1 \\ T_1 \end{pmatrix}}^{X_1} = A\overbrace{\begin{pmatrix} \bar{\phi}_0 \\ \bar{p}_0 \\ \bar{n}_0 \\ \bar{T}_0 \end{pmatrix}}^{\mathbf{e}}, \tag{4.64}$$

where the vector $\mathbf{e}$ obeys the normalization condition $(\mathbf{e}^\star\cdot\mathbf{e})|_\Re = 1$.

Because of the axial symmetry, the toroidal wave number $k_\zeta = \partial s/\partial\zeta = n = const$. The equilibrium quantities $n_i(a)$, $T_i(a)$, $T_e(a)$ are all function only of the minor radius a.

The ray equation

The equation $\mathcal{L}\mathbf{e} = 0$ has non-zero solution if and only if det($\mathcal{L}$)=0. This writes

$$\mathcal{D} = det(\mathcal{L}) = \frac{(\Omega - 1)(\Omega + 2\alpha h_0)}{\Omega(1 + \frac{1}{\tau}) + \frac{\eta_i + 1}{\tau} + 2\alpha h_0(1 + \frac{1}{\tau}) + \frac{2\Omega}{3\tau} - \alpha} + 2h_0 + \rho_s^2 k_\perp^2 \Omega - \frac{c_s^2}{\omega_{\star e}^2}\frac{k_{||}^2}{\Omega} = 0 \tag{4.65}$$

$$\Omega = \frac{\omega}{\omega_{\star e}},\ \alpha = \frac{5}{3\tau},\ h_0 = L_n \frac{\tilde{k}_z}{\tilde{k}_\vartheta},$$

where $k_{||}$ and $k_\perp$ are parallel and perpendicular components of the wave vector; $\omega_{\star e}$, $\tilde{k}_z$ and $\tilde{k}_\vartheta$ are given in equations (B.5-B.7), appendix B. The above equation has to be evaluated on the reference ray and is solved together with the ray tracing equations

$$\frac{\partial \mathcal{D}}{\partial a} = \frac{\partial \mathcal{D}}{\partial \vartheta} = \frac{\partial \mathcal{D}}{\partial k_a} = \frac{\partial \mathcal{D}}{\partial k_\vartheta} = 0. \tag{4.66}$$

The set of five equations (4.65-4.66) defines five unknowns, $\bar{a}$, $\bar{\vartheta}$, $\bar{k}_a$, $\bar{k}_\vartheta$, ω, which describe a toroidally closed ray trajectory. The coordinates $\left\{\bar{a}, \bar{\vartheta}\right\}$, defining the radial and poloidal position of the closed toroidally symmetric ray trajectory, are found from the first two equations in set (4.66). The corresponding wave vectors $\left\{\bar{k}_a, \bar{k}_\vartheta\right\}$ are determined by the two remaining equations of (4.66), and the frequency ω by the dispersion relation (4.65). One assumption of the beam tracing method is small increment $Im\ \omega \ll Re\ \omega$, so that ω is considered real from now on. Even if in reality this is not so, we can do this assumption because from the experiments done in plasma core it was noticed that the values of the particle and heat transport coefficients above the threshold are not so large in comparison with the threshold values.

The equations (4.65-4.66) give only the necessary condition for the existence of an eigenmode. For a conclusive judgement on the mode existence and stability one has to consider higher order equations (4.27-4.28) which after the solution of equations (4.65-4.66) read as

$$F_1(\Psi) = \mathcal{D}_{aa} + 2\mathcal{D}_a^a \Psi_{aa} + 2\mathcal{D}_a^\vartheta \Psi_{a\vartheta} + \mathcal{D}^{aa}(\Psi_{aa})^2 + 2\mathcal{D}^{a\vartheta}\Psi_{aa}\Psi_{a\vartheta} + \mathcal{D}^{\vartheta\vartheta}(\Psi_{a\vartheta})^2 = 0.$$

$$\begin{aligned} F_2(\Psi) = \mathcal{D}_{a\vartheta} + \mathcal{D}_\vartheta^a \Psi_{aa} + \left(\mathcal{D}_a^a + \mathcal{D}_\vartheta^\vartheta\right)\Psi_{a\vartheta} + \mathcal{D}_a^\vartheta \Psi_{\vartheta\vartheta} + \mathcal{D}^{aa}\Psi_{aa}\Psi_{a\vartheta} + \mathcal{D}^{a\vartheta}(\Psi_{a\vartheta})^2 \\ + \mathcal{D}^{\vartheta\vartheta}\Psi_{a\vartheta}\Psi_{\vartheta\vartheta} + \mathcal{D}^{a\vartheta}\Psi_{aa}\Psi_{\vartheta\vartheta} = 0 \end{aligned} \tag{4.67}$$

$$F_3(\Psi) = \mathcal{D}_{\vartheta\vartheta} + 2\mathcal{D}_\vartheta^\vartheta \Psi_{\vartheta\vartheta} + 2\mathcal{D}_\vartheta^a \Psi_{a\vartheta} + \mathcal{D}^{aa}(\Psi_{a\vartheta})^2 + 2\mathcal{D}^{a\vartheta}\Psi_{a\vartheta}\Psi_{\vartheta\vartheta} + \mathcal{D}^{\vartheta\vartheta}(\Psi_{\vartheta\vartheta})^2 = 0.$$

$\Psi_{\alpha\beta} = K_{\alpha\beta} + i\phi_{\alpha\beta}$, where α, β=a, ϑ. $K_{\alpha\beta}$ and $\phi_{\alpha\beta}$ describe the curvature of the wave front and the width of the wave packet, respectively.

$$\mathcal{D}_\alpha = \frac{\partial \mathcal{D}}{\partial q^\alpha},\ \mathcal{D}^\alpha = \frac{\partial \mathcal{D}}{\partial k_\alpha},\ \mathcal{D}_{\alpha\beta} = \frac{\partial^2 \mathcal{D}}{\partial q^\alpha \partial q^\beta}, \mathcal{D}^\beta_\alpha = \frac{\partial^2 \mathcal{D}}{\partial q^\alpha \partial k_\beta},\ \mathcal{D}^{\alpha\beta} = \frac{\partial^2 \mathcal{D}}{\partial k_\alpha \partial k_\beta}$$

There are more possible solutions for the above set of equations.

Once a closed ray trajectory (a solution to equations (4.65-4.66)) is found, the question arises whether this closed ray trajectory is related to an eigenmode and, if so, whether this eigenmode is stable or not. First, not any arbitrary closed ray can lead to an eigenmode. A necessary condition for this is the stability of the closed ray trajectory, which is equivalent with: the quadratic form $\phi_{\alpha\beta} = Im\ \Psi_{\alpha\beta}$ must be positive definite. Second, as follows from the equation of energy conservation, the marginally stable mode can exits if the medium under consideration provides the necessary sink or source of energy.

With the solution of the system (4.67), the set of beam tracing equations is completed. The equations (4.65-4.66) represent a set of first-order algebraic equations. To this end, note that all terms in equation (4.67) are evaluated on the reference ray only. Therefore, all the partial derivative of $\mathcal{D}$, as well a the functions $\Psi_{\alpha\beta}$, are taken at $a = \bar{a}(\tau)$ which depends only on the argument τ.

Equation for the wave amplitude

The last step to be done in our calculation is to determine the wave amplitude A, which is the factor that appears in front of the polarization vectors $\mathbf{e}$ in equation (4.64). By applying Fredholm alternative the solvability condition for the equation (4.63) is

$$X_1^\star \cdot \mathcal{M}\left[X_1\right] = 0 \qquad or \qquad X_1 \cdot \mathcal{M}^\star\left[X_1^\star\right] = 0 \tag{4.68}$$

where the symbol " $\star$ " denotes the complex conjugate. Reminding that $X_1 = A\mathbf{e}$ and adding the two relations in equations (4.68), we are going to find a relation for the amplitude of the wave in the form

$$X_1^\star \cdot \mathcal{M}\left[X_1\right] + X_1 \cdot \mathcal{M}^\star\left[X_1^\star\right] = \left(A^\star \mathbf{e}^\star \mathcal{M}_\nabla\left[A\right]\mathbf{e} + A\mathbf{e}\mathcal{M}^\star_\nabla\left[A^\star\right]\mathbf{e}^\star\right) +$$

$$A^\star A\left(\mathbf{e}^\star \mathcal{M}_\nabla\left[\mathbf{e}\right] + \mathbf{e}\mathcal{M}^\star_\nabla\left[\mathbf{e}^\star\right]\right) + A^\star A\left(\mathbf{e}^\star \tilde{\mathcal{M}}\mathbf{e} + \mathbf{e}\tilde{\mathcal{M}}^\star\mathbf{e}^\star\right) \tag{4.69}$$

We have to remind the reader that the equation (4.69) has to be evaluated only on the reference ray $\Re$. This means that the terms in equation (4.69), including the

unknown function A, depend on the single variable τ. Evaluating all the terms in the above equation, we get another form of transport equation.

$$\frac{d}{d\tau}|A|^2 + \gamma|A|^2 = 0$$

$$\gamma = \{\ \mathcal{D}_a^a + \mathcal{D}_\vartheta^\vartheta + \mathcal{D}^{aa}K_{aa} + 2\mathcal{D}^{a\vartheta}K_{a\vartheta} + \mathcal{D}^{\vartheta\vartheta}K_{\vartheta\vartheta} - 2\delta\frac{T_0}{T_e}\bar{\Phi}_0\bar{T}_0 -$$

$$2\frac{c_0^2}{\omega_{ci}^2}\frac{1}{L_n}\left(k_a g^{aa} + k_\vartheta g^{a\vartheta}\right)\left[\bar{\Phi}_0^2 + \frac{n_0}{n_i}\bar{\Phi}_0\bar{p}_0\right] + 2\frac{n_0}{n_i}\frac{c_0^2}{\omega\omega_{ci}}\frac{1}{L_n}\frac{\tilde{B}}{\sqrt{g}}\bar{\Phi}_0\bar{p}_0 + 5\frac{c_0^2}{\omega\omega_{ci}}\frac{1}{L_{Ti}}\frac{\tilde{B}}{\sqrt{g}}\bar{p}_0\bar{T}_0$$

$$-2\frac{c_0^2}{\omega\omega_{ci}}\left[\bar{\Phi}_0^2 + \frac{n_0}{n_i}\bar{\Phi}_0\bar{p}_0\right]\tilde{C} + 2\frac{c_0^2}{\omega\omega_{ci}}\frac{1}{L_n}\left[\bar{\Phi}_0^2 + \left(\frac{3}{2}\eta_i - 1\right)\bar{\Phi}_0\bar{p}_0\right]\tilde{D} - 5\bar{p}_0\bar{T}_0\frac{c_0^2}{\omega\omega_{ci}}\tilde{C}\ \} = 0 \tag{4.70}$$

where $g^{\alpha\beta}$ $(\alpha, \beta{=}a, \vartheta)$ are the components of the fundamental contravariant fundamental tensor, g is the inverse of the determinant of the matrix $g^{\alpha\beta}$, $\tilde{A} = \partial_a R$ and $\tilde{B} = \partial_\theta R$, all these quantities are given explicitly in appendix B;

$$\tilde{C} = \frac{\left(-\tilde{A}aR\partial_\vartheta d + \tilde{B}Rd + \tilde{B}aR\partial_a d\right)}{(aRd)^2},\quad \tilde{D} = \frac{\tilde{B}d + R\partial_\vartheta d}{aRd^2},$$

4.4.4 ITG eigenmodes in a rotating tokamak plasma

Experimental and theoretical investigation in the last decade have shown the importance of plasma rotation in the confinement of tokamak plasma. Both poloidal and toroidal plasma rotations have been observed in various tokamaks. Usually the poloidal plasma rotation is associated with the $\vec{E}\times\vec{B}$ drift, induced by a strong inhomogeneous radial electric field E_r whereas the toroidal plasma rotation is attributed to external sources.

In the theory of ITG mode, effects of toroidal [86]-[88] and poloidal [89]-[91] rotation was first introduced separately and then together [92]-[95] in a shear slab geometry. The effects of flow were found to be rather subtle, being stabilizing in some parameter ranges and destabilizing in others. However, for fairly strong toroidal and poloidal flow shear there is a general tend of stabilization. The effects of velocity curvature and magnetic field curvature were later realized to be very important. The toroidal magnetic field curvature has been taken fully into account in nonlinear simulation of ITG mode turbulence using the strong ballooning approximation and both poloidal and toroidal flows in a kinetic model [88]. However in [88], the effect of flow shear has been implemented in a rather heuristic way in simulations by making

the substitution $\gamma_L \rightarrow \gamma_L - \gamma_E$, where γ_L is the linear growth rate in the absence of flow shear and γ_E is the shearing rate. Thus complete stabilization is expected is

$$\gamma_E \geq \gamma_{Lmax}$$

In [96] has been shown that the linear effects may be sufficient for an effective stabilization of the ITG mode reactive instability in the presence of shear plasma poloidal and toroidal rotation. In contrast to the ordinary drift mode for which a velocity curvature of the poloidal rotation is a decisive stabilization factor, for a reactively unstable ITG mode a velocity shear becomes more important.

Due to their importance, the poloidal and toroidal rotations have been included also in our ITG fluid model. The difference with the previous calculation done in the beginning of this section, is that now the total ion velocity writes as:

$$\vec{v} = \vec{v}_0 + \vec{v}_i$$

where $\vec{v}_0 = v_{0\vartheta}\nabla a \times \nabla\zeta + v_{0\zeta}\nabla\zeta$ is the background plasma velocity flow and $\vec{v}_i$ is the perturbed velocity considered already in our calculations. By introducing the background velocity component in our fluid model, the partial derivative in respect with the time from the fluid $\partial/\partial t$ is replaced by $\partial/\partial t + \vec{v}_0 \cdot \vec{k}$. The fluid equations that describe the ITG mode when the background velocity flow is considered are given in the appendix.

The dispersion relation results in:

$$\frac{(\Omega - \frac{\vec{v}_0\cdot\vec{k}}{\omega_{\star e}} - 1)(\Omega - \frac{\vec{v}_0\cdot\vec{k}}{\omega_{\star e}} + \frac{5}{3}\frac{2h_0}{\tau})}{(\Omega - \frac{\vec{v}_0\cdot\vec{k}}{\omega_{\star e}})(1 + \frac{1}{\tau}) + \frac{\eta_i+1}{\tau} + 2\alpha h_0(1 + \frac{1}{\tau}) - \alpha + \frac{2\Omega}{3\tau}} + 2h_0 +$$

$$\rho_s^2 k_\perp^2 (\Omega - \frac{\vec{v}_0 \cdot \vec{k}}{\omega_{\star e}}) - \left(\frac{c_e k_{||}}{\omega_{\star e}}\right)^2 \frac{1}{(\Omega - \frac{\vec{v}_0\cdot\vec{k}}{\omega_{\star e}})} + \frac{c_e k_{||}\rho_s}{\omega_{\star e}} \frac{(\vec{e}_{||} \times \nabla v_{||0}) \cdot \vec{k}}{(\Omega - \frac{\vec{v}_0\cdot\vec{k}}{\omega_{\star e}})} = 0 \qquad (4.71)$$

As could be noticed from equation 4.71 in the absence of plasma rotation the dispersion relation for the ITG mode in the pWKB approximation is given by equation 4.65.

4.5 Summary

In order to solve the wave equation in the short wavelength limit different asymptotic approaches have been used. One of the most famous technique is the WKB

method. A modification of the WKB approach, the paraxial WKB or the beam tracing method (BT), is introduced in this chapter. In pWKB approach the plasma microinstabilities can be thought as waves propagating in the toroidal direction, while the interaction with the a plasma defines whether such a wave absorbs or release energy. The pWKB is closely related with the ballooning representation because both of them use the same asymptotic expansion. This method can provide solution in many cases of interest where the BR fails.

The pWKB technique has been employed to formulate the model of the toroidal ion temperature gradient driven instability. Calculations including plasma rotations have been also performed. The resulting equation are obtained in a fluid limit, the parallel ion dynamics being also included.

Chapter 5

Results and discussions

In the previous chapter we have introduced the paraxial WKB approximation method and we have found the set of ordinary differential equations that have to be solved in case of ITG turbulence. As discussed in the previous chapter, three successive steps have to be done in order to find the short-wavelength eigenmodes.

- finding the closed ray trajectory, equations (4.65-4.66).
- assessment of its stability by solving equation (4.67).
- evolution of the growth rate, equation (4.70).

Because of the quite complicated dependence of the BT equations (4.65, 4.66, 4.67) on the coordinates and on wave vectors, the solutions of these equations in a general tokamak geometry requires a numerical treatment. This can be performed in a straightforward way, since we have to do with a set of algebraic equations, as already stressed. The code which solves the set of BT equation (4.65, 4.66, 4.67) is written in C programming language. The iterative Newton method is used to solve the systems of BT equations.

The beam tracing equations are solved for plasma parameters of ASDEX-Upgrade tokamak. Typical values are $R_0 = 1.65$ m, $a_M = 0.50$ m, $B_0 = 3.0$ T.

5.1 ITG mode

The dependence of the growth rate and the real frequency, which describe the ITG turbulence, on different parameters has been already studied by many other authors.

To validate the results of our calculations different scans are carried out, similar with those computed with some other fluid codes. We are going to observe the

common features of different results and to underline what BT model brings new. One model used for our comparison is that of Guo & Weiland [85]. As have been already mentioned in chapter 3, Weiland model is one of the most popular in transport modelling. Therefore, comparison with it and studying its limitation is needed.

In order to do easier the comparison between our model and Guo & Weiland, is useful to overview briefly their features.

First of all, we emphasize that the both approaches employ two essential assumptions: (i) wavelength and (ii) eigenmode width are smaller in comparison with all plasma parameters inhomogeneity lengths. The former one follows from inequality $\omega_{ci}/\omega \gg 1$ and is always fulfilled with a large margin. The second is more restrictive. First, it implies that the radial mode extension is small in comparison with the radial inhomogeneity length. This is usual well justified. Second, the mode should be poloidally localized so that its angular size is smaller than π. This limit is called "strong ballooning approximation" [Weiland]. If this is not true, then the results discussed in this section are inapplicable.

The validity of the strong ballooning approximation can be checked in both approaches compared below. The beam tracing provides an evaluation of the mode width as part of the solution and thus enables the validation of the applicability as a part of the solving procedure. On the other hand, the ballooning formalism, allows to relax the strong ballooning approximation, and treat mode of arbitrary poloidal extension. However, such a treatment requires solving differential equation and therefore is much more time consuming.

5.1.1 BT (beam tracing) model

The beam tracing model does not involve any further approximations. It deals with the dispersion relation

$$\begin{aligned}\mathcal{D} &= \Omega^3\left[1+b_\theta\tau(1+\alpha)\right]-\Omega^2\left[1-4\alpha\varepsilon_n-2\varepsilon_n-b_\theta\tau\Gamma\right]\\ &-\Omega\left[2\alpha\varepsilon_n-2\Gamma\varepsilon_n+\frac{c_s^2}{\omega_{\star e}^2}k_{||}^2(1+\alpha)\right]-\frac{c_s^2}{\omega_{\star e}^2}k_{||}^2\Gamma=0,\end{aligned} \tag{5.1}$$

where $\Omega = \omega/\omega_{\star e}$, $b_\theta\tau = (\rho_s k_\perp)^2$, $\tau = T_e/T_i$, $k_\perp^2 = k^2 - k_{||}^2$, $\alpha = 5/3\tau$, $\eta_i = n_e\nabla T_e/(T_e\nabla n_e)$, $\epsilon_n = n_e/(\nabla n_e R_0)$ and $\Gamma = \frac{\eta_i+1}{\tau} - \alpha + 2\alpha\varepsilon_n(1+\frac{1}{\tau})$.

Arbitrary radial dependence of the parameters is allowed in equation (5.1). Eigenmode position in the poloidal cross-section is defined by the set of algebraic equations

$$\partial\mathcal{D}/\partial\vartheta = \partial\mathcal{D}/\partial a = \partial\mathcal{D}/\partial k_\vartheta = \partial\mathcal{D}/\partial k_a = \mathcal{D} = 0. \tag{5.2}$$

This makes 5 algebraic equation with 5 unknowns $\{\omega, a, \vartheta, k_a, k_\vartheta\}$. The eigenmode extension and the growth rate can be defined making use of higher order equations equation (4.67). In a special case, when equation (5.2) does not have real solution the procedure discussed in Appendix E should be applied.

5.1.2 Guo & Weiland approach

Extensively used transport model known as the Weiland model [Guo & Weiland] is based on the ballooning representation. This representation can be obtained from the dispersion relation (5.1) where

1. the wave vector component $k_{||}$ is replaced with the differential operator $-i\nabla_{||}$,
2. the component $k_\perp$ whenever it appears is replaced with k_θ (thus implying $k_a = 0$),
3. k_θ is defined by the condition $b_\theta = \rho_s^2 k_\theta^2/\tau = 0.1$,
4. k_ϕ is implicitly defined by the condition $k_{||} \approx 0$,
5. the eigenmode is centered at the mid-plane $\vartheta = 0$,
6. the radial dependence is neglected in all plasma parameters except for the safety factor q where it is approximated by the linear dependence.

   The problem is now formulated as a boundary value problem for this differential equation with proper boundary conditions. Further simplification can be obtained by fitting the poloidal dependence by a parabola (strong ballooning approximation) and finally replacing the eigenvalue problem by the solvability condition for the fundamental mode:

$$\begin{aligned}\Omega^2\left[1 + b_\theta\tau(1+\alpha)\right] \;&-\; \Omega\left[1 - 4\varepsilon_n\alpha - 2\varepsilon_n - b_\theta\tau\Gamma - i\frac{\varepsilon_n\hat{s}}{q}(1+\alpha)\right] \\ &-\; \left[2\alpha\varepsilon_n - 2\Gamma\varepsilon_n + i\frac{\varepsilon_n\hat{s}}{q}\Gamma\right] = 0\end{aligned} \tag{5.3}$$

This equation can be viewed as a combination of the 1st and 2nd orders of the beam tracing technique. The only unknown in the equation (5.3) is the complex frequency $\omega + i\gamma$.

Unlike the beam tracing the wave-vector components are prescribed by the set of conditions listed above. For this reason, in the Weiland model b_θ is an independent input parameter while in BT approach the quality k_θ, and consequently b_θ, is a result of solving equation (5.2). Variation of the parameter b_θ in the BT model can be achieved by varying the external parameter k_ϕ related to the toroidal wavenumber n.

Another difference is that, in Weiland model, the eigenmode can be located at any radial position in the plasma mid-plane (plane of the up-down symmetry.) In order to impose the same property in the BT model the two first equation in equation (5.2) were omitted. Finally, it should be noted that due to the limitation of the Guo & Weiland model no background plasma rotation was included and that the comparison was limited to the case of circular geometry.

After all these simplifications the plasma parameters ε_n, η_i, τ, q, $\hat{s}$ can be considered as an independent input. Eigenmode characteristics calculated in this way will be compared for both approaches.

5.2 Dependence of ITG model on different parameters in the two models

Guo & Weiland and the simplified BT models have been used to derive the frequency and growth rate of the ITG mode. The Guo & Weiland results have been reported in [85].

Using the BT model, considering the set of parameters as in [85] ($s = \tau = 1.0$, $\eta_i = 8.0$, q=2.0), we have computed the un-normalized, figures (5.1) and the normalized, figure (5.2), growth rates of ITG mode, as a function of b_θ. Different values of ϵ_n are considered. The values of b_θ are obtained by making a scan in the toroidal wave number n.

In case of the un-normalized growth rates, figure (5.1), can be noticed that for any given value of ϵ_n the growth rate reaches its maximum at $b_\theta \approx 0.2$. When the normalized growth rates are considered, figure (5.2), for any given ε_n, the normalized growth rate is decreasing with increasing b_θ. Because of interest are the un-normalized values of the growth rates, we can say that, for the set of parameters considered in [85], the BT model finds the most unstable mode at $b_\theta \approx 0.2$.

The first comparison between the two models is illustrated in figure (5.3). The figure contains the normalized frequencies and growth rates vs ϵ_n, in Guo & Weiland model and BT model. In case of BT model two different values of the parameter b_θ were selected from figure (5.2): $b_\theta = 0.1$ (the same as considered in Weiland model) and $b_\theta = 0.22$ (the value that was found above to correspond to the most unstable mode).

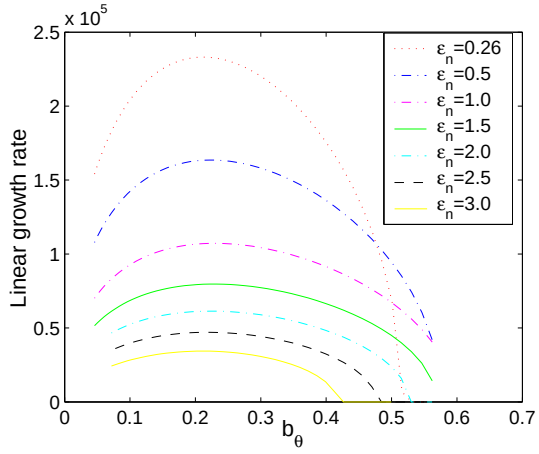

Figure 5.1: Linear growth rate vs b_θ in our model. $s = \tau = 1.0$, $\eta_i = 8.0$, q=2.0..

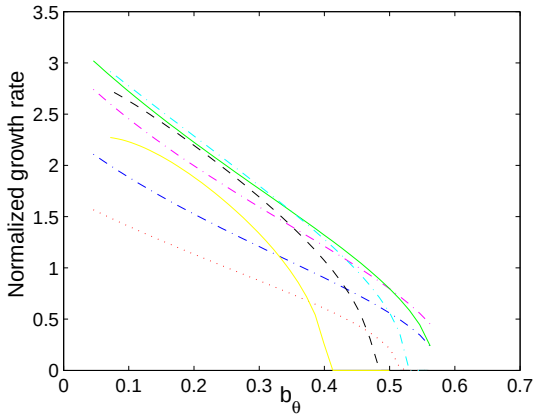

Figure 5.2: Normalized growth rate vs b_θ in our model. $s = \tau = 1.0$, $\eta_i = 8.0$, q=2.0..

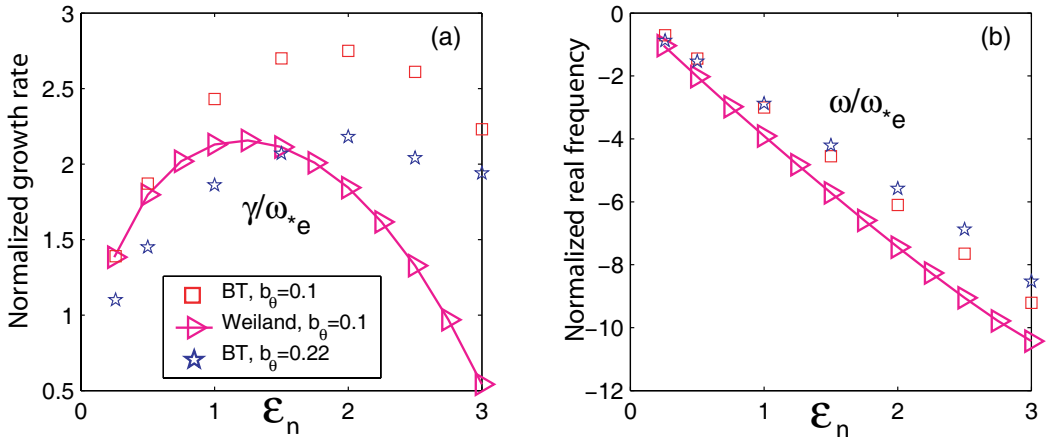

Figure 5.3: Normalized growth rate and real eigenfrequency as function of ε_n. Comparison of our model $b_\theta = 0.1$ (squares) and $b_\theta = 0.22$ (pentagons) with Weiland model $b_\theta = 0.1$ (triangles). The parameters are $s = \tau = 1.0$, $\eta_i = 8.0$, q=2.0.

Both, the qualitative and the quantitative comparison between the two models

are done. Qualitatively, there is a good agreement between the two models. The normalized growth rate has a maximum as a function of ε_n, figure (5.3a). The real frequency is found in both models to be negative. This result is expected because we deal with the ion temperature gradient mode. The real frequency increases linearly from low values at smaller ϵ_n to around $10\omega_{\star e}$ at the larger ϵ_n.

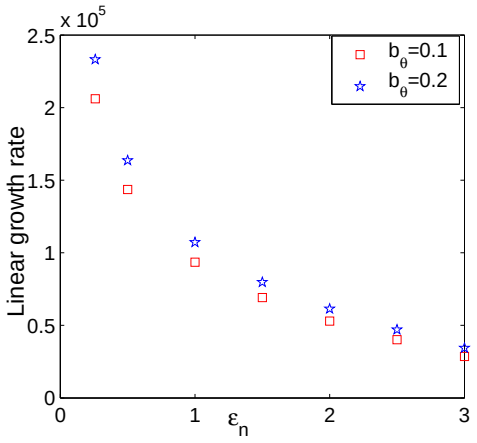

Figure 5.4: Linear growth rate of ε_n in BT model: $b_\theta = 0.1$ (squares) and $b_\theta = 0.22$ (pentagons). The parameters are $s = \tau = 1.0$, $\eta_i = 8.0$, q=2.0.

Quantitatively, in BT model the maximum of the normalized growth rate is shifted to a larger value of ε_n. The mode corresponding to $b_\theta = 0.22$, in BT model is in relative good agreement with Guo & Weiland model. As regards the real frequency, there exists a good agreement between all the situations considered.

From figure (5.3a) one could get the feeling that in the BT model, the mode corresponding to $b_\theta = 0.1$ (squares) is more unstable that the mode corresponding to $b_\theta = 0.22$ (stars). It is useful to mentioned once again that figure 5.3(a) contains the normalized values of the growth rates. To judge correct which of the two modes is more unstable the un-normalized growth rates have to be considered. The un-normalized growth rates are included in figure (5.4). In this way, can be noticed that for each given ε_n, the mode corresponding to $b_\theta = 0.22$ is more unstable that the mode corresponding to $b_\theta = 0.1$.

5.2.1 T_e variation

The previous comparison was realized for the electron temperature $T_e = T_i = 1.0$ keV. Let us now study the dependence of the growth rate and real frequency on

temperature, using the BT model. For this purpose four different temperatures are considered: $T_e = 0.1$ keV, $T_e = 0.5$ keV, $T_e = 1.0$ keV, $T_e = 10$ keV.

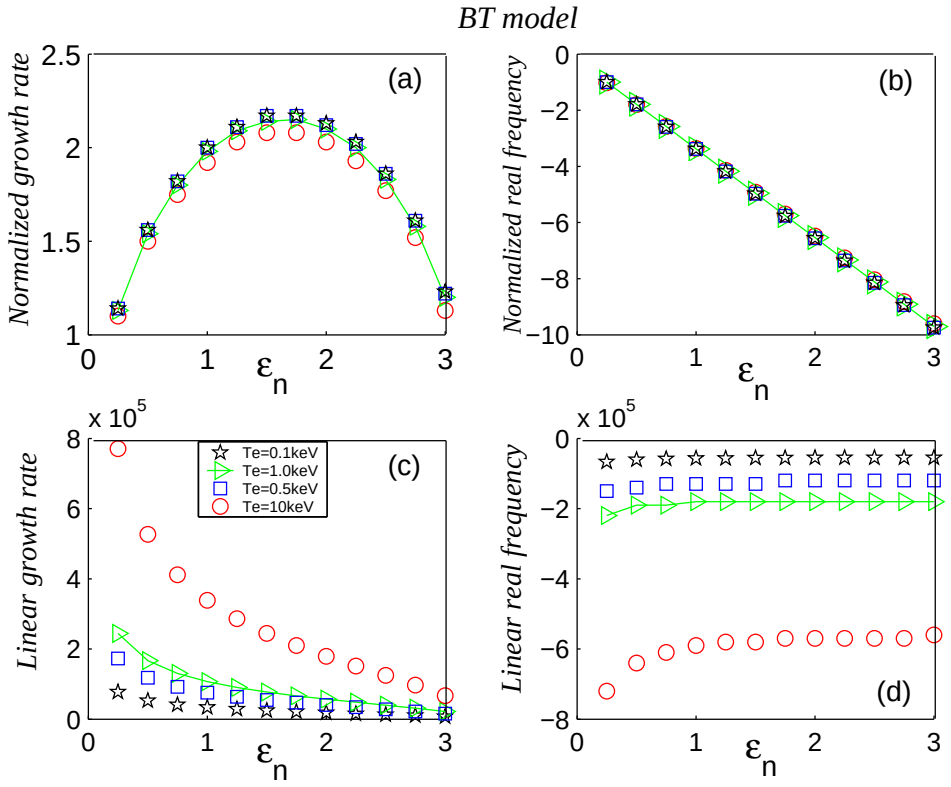

Figure 5.5: (a)Normalized growth rate (b) normalized real frequencies (c) Linear growth rate γ (d) real frequencies ω, corresponding to the most unstable mode, vs ε_n for different temperatures. In all $s = \tau = 1.0$, $\eta_i = 8.0$, $q = 2.0$.

In the above plot only the most unstable mode was selected. It can be noticed that both, the normalized growth rate and real frequency, do not depend at all on the temperature.

While in Guo & Weiland model the electron and ion temperature appear only in the combination $\tau = T_e/T_i$, in the BT model the dependence on the electron temperature is still kept explicitly in the term $\rho_s k_\perp$. So that we are expecting that in this case the eigenfunctions are going to depend on T_e. Figures (5.5c) and (5.5d), depict the linear growth rate and real frequency corresponding to the considered temperatures versus ε_n. The real frequency, ω, depends on T_e as $\omega_{\star e}$. For the dependence of the growth rate on T_e another dependence comes into play $\rightarrow b_\theta = (\rho_s k_\perp)^2$.

For a given temperature the mode is found to be stabilized with increasing ε_n. On

the contrary, for a given value of ε_n, the higher the temperature the more unstable is the mode. It is also found that the value of b_θ corresponding to the most unstable mode is almost constant when the temperature is increased from 0.1 to 10.0 keV.

5.2.2 $\tau = T_e/T_i$ variation

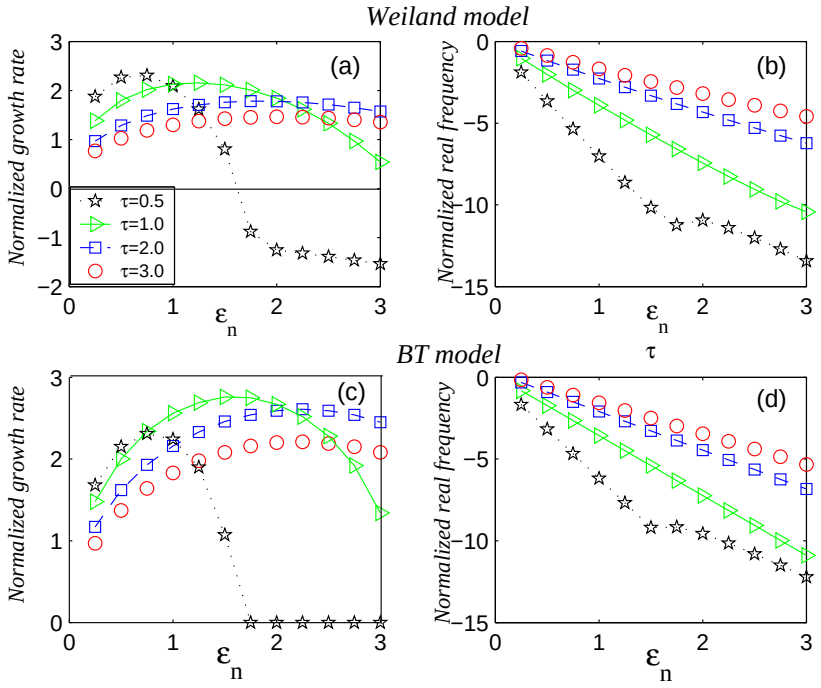

Figure 5.6: (a) Normalized growth rate Weiland model, (b) real eigenfrequencies Weiland, (c) Normalize growth rate in our model, (d) real frequencies in our model, vs ε_n for different values of τ. $s = 1.0$, $\eta_i = 8.0$, q=2.0.

The stability of the ITG mode is also determined by the dimensionless parameter $\tau = Te/T_i$. The destabilizing effect of T_e/T_i on ITG modes is already known from the literature [97], [98]. Figure (5.6) shows the comparison between the normalized growth rate and real frequencies, corresponding to Guo & Weiland 5.6(a,b) and BT 5.6(c,d) models, for different values of τ. It has to be mentioned that the plots that include Guo& Weiland model are not a result of these thesis. They are done using the dispersion relation (5.3), which is a result of [85], and are used here only for comparison with our model. In case of BT model only the most unstable modes have been selected. A very good qualitative agreement is found between the two models. At $\tau = 0.5$ the ITG mode is found to become stable for values of $\varepsilon_n > 1.5$. In order to study how the mode behaves with the increasing parameter τ the linear

growth rate is plotted using BT model in figures (5.7) and (5.8). For each given value of τ, the stabilizing effect of ϵ_n is again found. Figure (5.8) shows the linear growth rate versus τ, for $\varepsilon_n = 1.5$. The destabilizing effect of τ is obvious.

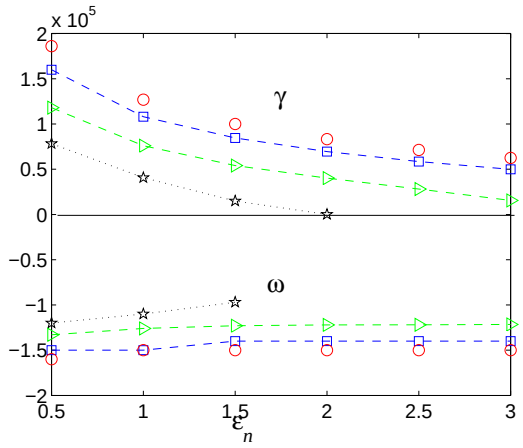

Figure 5.7: Linear growth rate vs ε_n for different values of τ in BT model. $s = 1.0$, $\eta_i = 8.0$, q=2.0. $\tau = 0.5$ (stars), $\tau = 1.0$ (triangles), $\tau = 2.0$ (squares), $\tau = 3.0$ (circles).

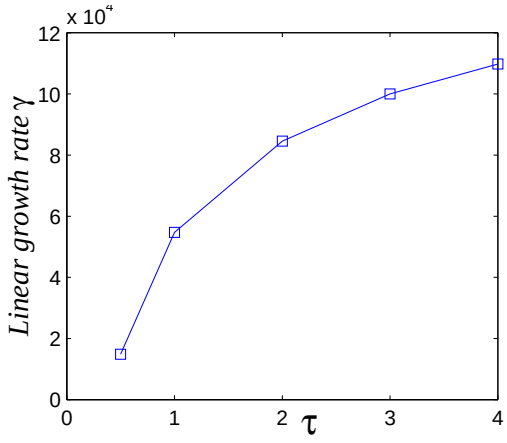

Figure 5.8: Linear growth rate vs τ in our model. $s = 1.0$, $\eta_i = 8.0$, q=2.0, $\varepsilon_n = 1.5$.

5.2.3 q variation

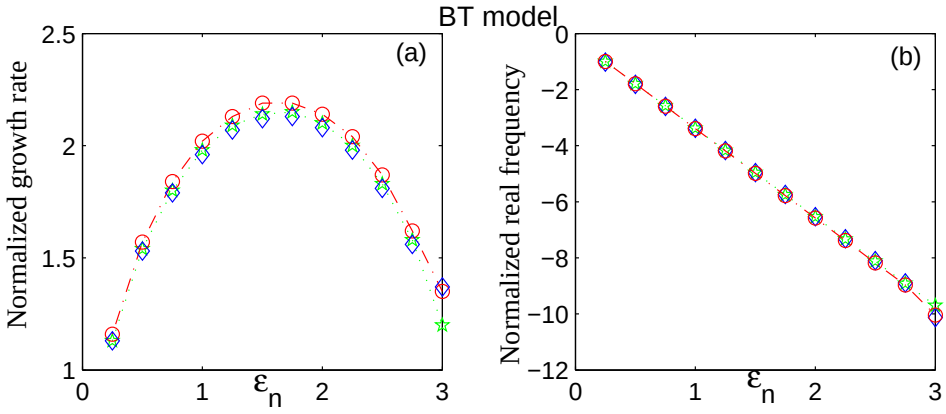

Figure 5.9: (a) Normalized growth rate and (b) real frequency corresponding to the most unstable mode in BT model, for different values of the safety factor q (q=2 (stars), q=6 (circles), q=10 (diamonds)). $s = \tau = 1.0$, $\eta_i = 8.0$, $T_e = 1.0$ keV.

It is useful to study also the dependence on the safety factor. In BT model, the safety factor appears in the expression of $k_{||}$. In this comparison with Guo & Weiland model is the only quantity which is still keeping the dependence on the minor radius.

To study how the ITG mode depends on the safety factor three values of q are considered: $q = 2$, $q = 6$, $q = 10$. Figure (5.9) shows the behaviour of the normalized growth rate and real frequency as a function of the parameter ε_n. It is found that BT model depends very weakly on the safety factor q, which in the core plasma ranges from 1 to 4. This is in agreement with Guo & Weiland model [85].

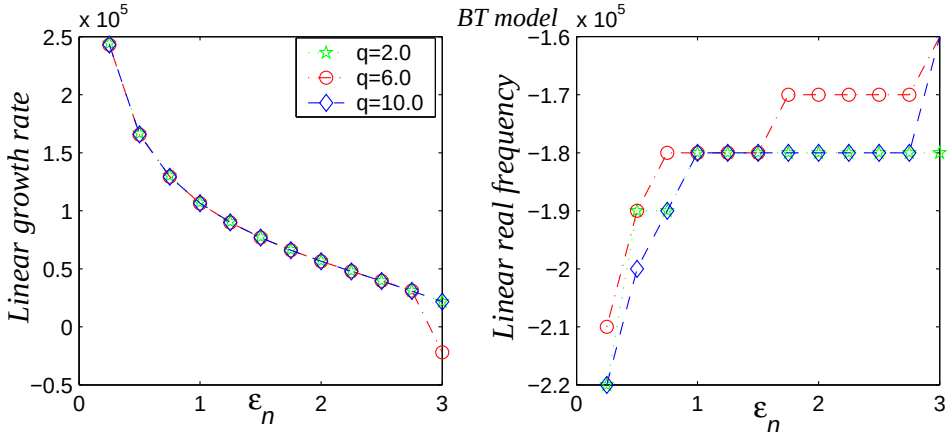

Figure 5.10: Linear growth rate γ (positive) and real frequencies ω (negative), corresponding to the most unstable mode, vs ε_n for different values of q. $s = \tau = 1.0$, $\eta_i = 8.0$, $T_e = 1.0$.

Because the normalization is done in respect to ω_{*e}, which does not depend on q, is expected that the values of linear growth rate and real frequency, figure (5.10), do not depend also on q.

5.2.4 η_i variation

As discussed in Chapter 2, the parameter $\eta_i = L_{ni}/L_{Ti}$ plays a significant role in the ITG stability. Both of them, the ion temperature gradient and the density gradient influence the threshold stability of the ITG turbulence.

Figure (5.11) shows growth rate and real frequency (normalized to electron diamagnetic frequency) as a function of ε_n for seven different values of η_i. Results from both models are presented again: Guo & Weiland figure (5.11a,b) and BT model (5.11c,d). For each given η_i there exists a threshold in ε_n above which the mode destabilizes. Because $\eta_i/\varepsilon_n = R/L_{Ti}$, one can also say that there exists a threshold

in R/L_{Ti} above which the mode is destabilizing.

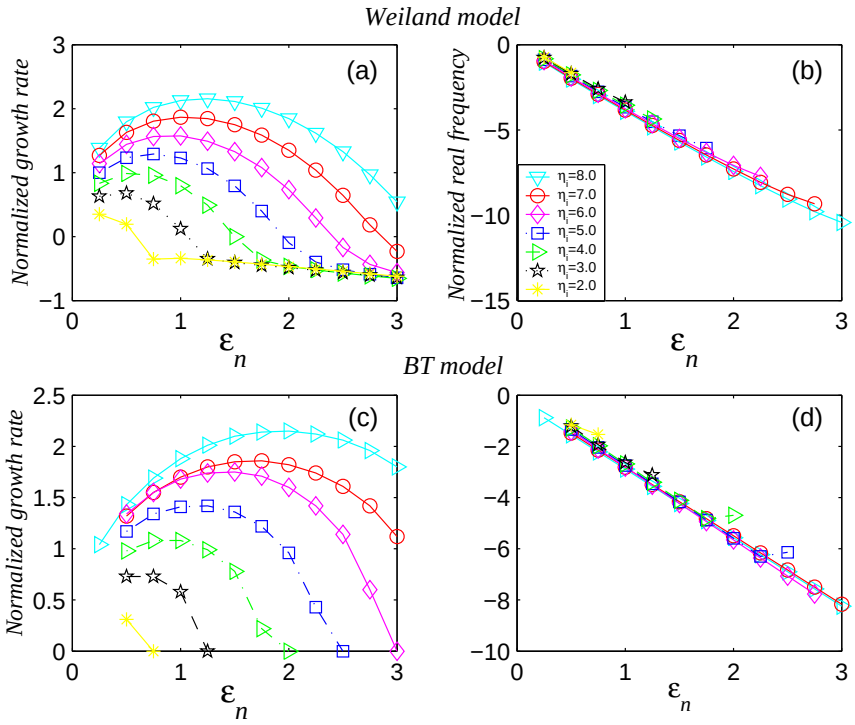

Figure 5.11: (a) Normalized growth rate Weiland model, (b) real frequencies Weiland model, (c) normalized growth rate BT model, (d) real frequencies BT model, vs ε_n for different values of η_i. $s = \tau = 1.0$, $q = 2.0$, $T_e = 1.0$.

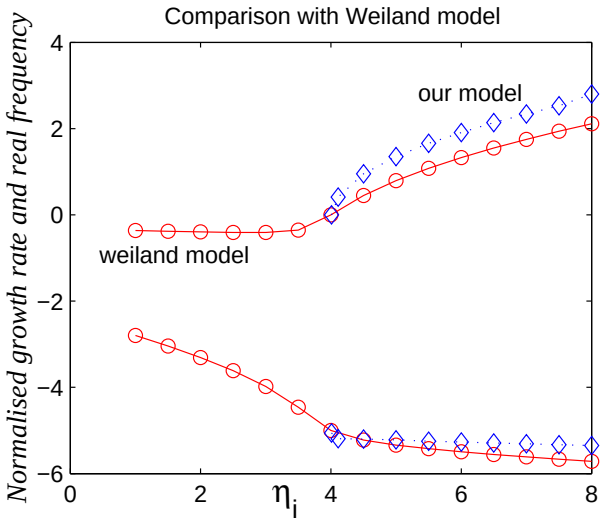

Figure 5.12: Normalized growth rate γ (positive) and real frequencies ω (negative), vs η_i. $n = 40$, $s = \tau = 1.0$, $q = 2.0$, $\varepsilon_n = 1.5$.

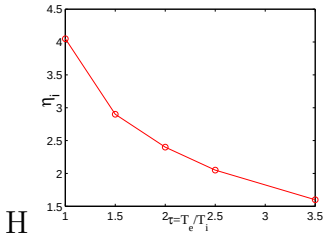

Figure 5.14: The threshold in η_i vs τ. s=1.0, q=2.0.

The value of the real frequency increases linearly from low values at the lower η_i threshold to around $8\omega_{\star e}$ at the upper η_i threshold.

The value of the threshold in R/L_{Ti} can be better noticed looking to the next figure (5.12). A comparison of the two models is done. Fixing $\varepsilon_n = 1.5$, η_i is varied between 1.0 and 8.0. For small values of η_i both models found the mode to be stable. For the considered set of parameters, when η_i becomes larger than 4.0 the ITG mode is destabilized. This correspond to a threshold $R/L_{Ti} = \eta_i/\varepsilon_n = 2.66$.

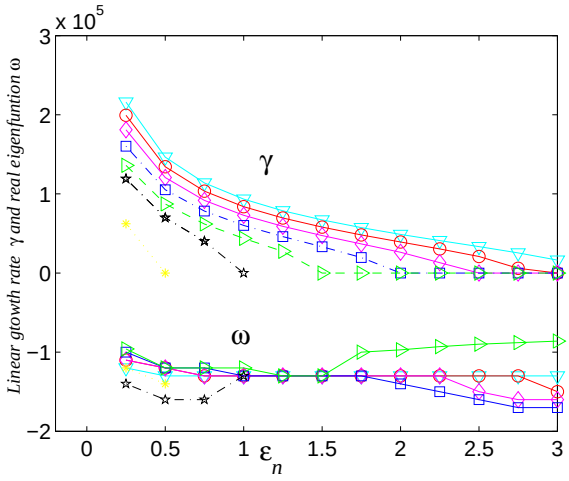

Figure 5.13: Linear growth rate γ (positive) and real frequencies ω (negative), corresponding to the most unstable mode, vs ε_n for different values of η_i ($\eta_i = 8.0$ - ciel, $\eta_i = 7.0$ - red, $\eta_i = 6.0$ - pink, $\eta_i = 5.0$ - blue, $\eta_i = 4.0$ - green, $\eta_i = 3.0$ - black, $\eta_i = 2.0$ - yellow). $s = \tau = 1.0$, $q = 2.0$, $T_e = 1.0$.

The linear growth rate and real eigenfrequency are shown in figure (5.13). It can be noticed there that the larger is R/L_{Ti} the more unstable becomes the mode. This behaviour is expected since the ITG turbulence is known to be driven by temperature gradients. In figure (5.14) can be seen that the threshold in η_i is different for different value of τ: at larger values of τ the mode becomes unstable for lower values of η_i.

5.2.5 Dependence on the toroidal wave number

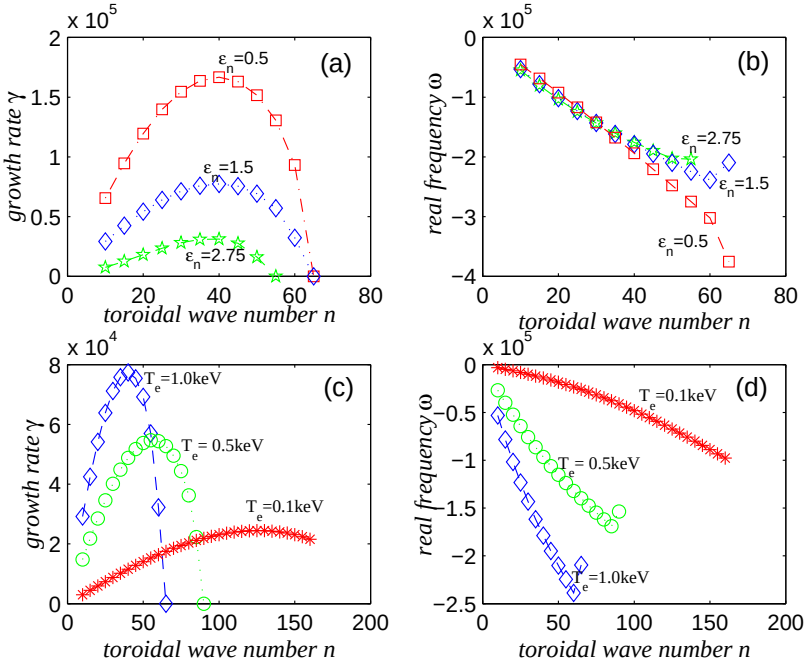

Figure 5.15: (a) and (b) Linear growth rate γ, and the real frequency ω along the toroidal wave number n for three different values of ε_n, $T_e = 1.0$ keV, $\eta_i = 8.0$, $s = \tau = 1.0$, $q = 2$. (c) and (d) Linear growth rate γ and the real frequency ω along the toroidal wave number n for three different values of T_e, $\varepsilon_n = 1.5$, $\eta_i = 8.0$, $s = \tau = 1.0$, $q = 2$.

The calculations done till now with the BT model, depending on different parameters, the most unstable mode correspond to different value of the toroidal wave number. All the calculation done have some common features. The linear growth rate has a maximum as a function of the toroidal wave number, figures (5.15a) and (5.15c). The modulus of the real eigenfrequency is increasing linearly with increasing toroidal wave number, figures (5.15b) and (5.15d). This dependence is similar to that of the normalized growth rate and real frequency on ε_n. In our calculations, values of the toroidal wave number was varied n from 10 up to 200.

The stabilizing effect of ε_n obtained before appears again in figure (5.15a) (for flatter density profiles, larger values of ε_n, the mode is stabilized). It is found that the value of the toroidal wave number corresponding to the most unstable mode is not changed by the flattering of the density profile.

In contrast with previous case, the value of the toroidal wave number corresponding to the most unstable mode depends on the temperature, figure (5.15c). At small

temperatures, values of the toroidal wave number larger than 100 correspond to the most unstable mode. This value is decreasing with the increasing temperature. The parameter $b_\theta = 0.22$ is found to correspond to the most unstable mode for all considered temperatures.

5.3 The solution of the full set of beam tracing equations

Up to now we have shown the results obtained using a "simplified" beam tracing model. This was done in order to make possible the comparison with Gue & Weiland model. In the previous section the radial dependence was neglected solving only four beam tracing equations, from the set of five.

In what follows we are going to extend our discussion to the case of global calculations, when the full set of beam tracing equation is solved. The radial extend of the microinstability is computed together with the poloidal and radial wave numbers, the poloidal angle and the frequency.

As mentioned in the beginning of this chapter, the BT approach allows arbitrary radial dependence of all the profiles: the density, the ion and electron temperatures, the safety factor.

5.3.1 Exponential like profiles

In this section we use profiles proposed in [101].

$$\begin{aligned} n(s)/n_0 &= \exp\left(\frac{a_M \Delta s_N}{L_{0N}} \tanh \frac{s-s_0}{\Delta s_N}\right) \\ T(s)/T_0 &= \exp\left(\frac{a_M \Delta s_T}{L_{0T}} \tanh \frac{s-s_0}{\Delta s_T}\right) \end{aligned} \tag{5.4}$$

where n_0 and T_0 are on-axis values of the density and temperature, $s = a/a_M$, a_M the minor radius, is the normalize radius variable, $\Delta s_{N,T}$ the radial width over which these profiles varies. The characteristics length $L_{N,T}$ has minimum at $s = s_0$ and given by $L_{0N,T}$. For the safety factor, a four order polynomial is considered:

$$q(s) = q_0 + c_1 s^2 + c_2 s^3 + c_3 s^4, \tag{5.5}$$

where c_1, c_2 and c_3 are constants that can be changed. This choice, allows one, for instance, to fix safety factor on axis q_0 and on the edge $q_s(1)$ as well as its value $q_s(s_0)$ and shear $\hat{s}(s_0)$ at an intermediate point s_0.

Considering profiles of this kind, the mode tends to localize at $s = s_0$. So that, by choosing an appropriate value of the parameter s_0, one can somehow decide the radial position where the mode occurs.

5.3.2 Toroidal wave number scan, benchmarking with gyrokinetic calculations.

To validate the global BT model, a toroidal wave number scan was carried out, similar to the one previously computed in [101], with a nonlinear gyrokinetic code. The above profiles are used for density, temperature and safety factor. A deuterium plasma is considered. The magnetic geometry is chosen with $B_0 = 3.7$ T, $R_0 = 2.58$ m, $a_M = 0.92$ m, $q = 1.2 + 9.6s^3$. For the density profile we have chosen: $L_{0N} = 0.74$ m, Δs_N=0.26, $s_0 = 0.315$. Temperature profiles are identical for electrons and ions, with $T_0 = 1.3$ keV, $L_{0T} = 0.19$ m, $\Delta s_T = 0.26$ and $s_0 = 0.315$. These profiles are identical with those used in [101].

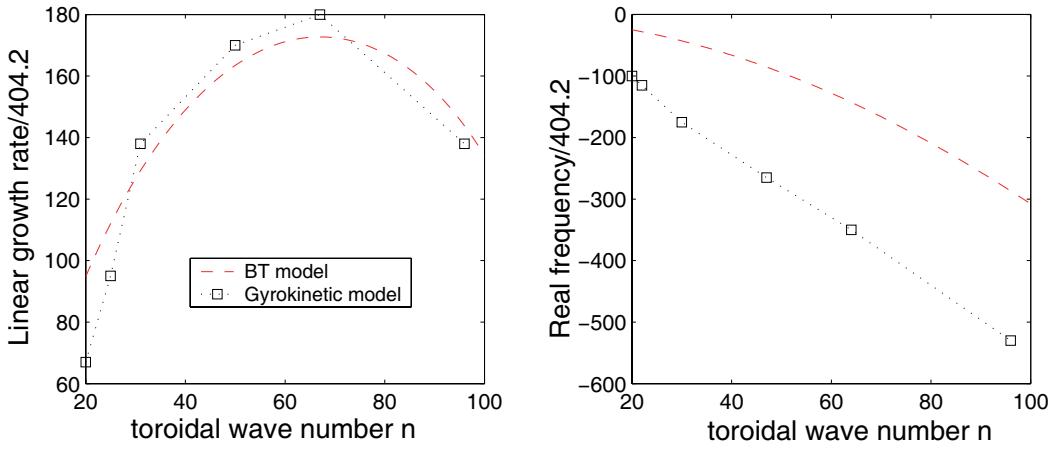

Figure 5.16: Growth rate and real frequency along a toroidal wave number scan. The nonadiabatic responce of electrons is not taken into account. The results obtained with the BT model are plotted with red color. Results of a gyrokinetic code for each value of n are plotted with squares.

Figure (5.16) shows the growth rate and the real frequency, as a function of the toroidal wave number n for both the BT model for the linear gyrokinetic code. All frequencies are normalized in respect with $\omega_{norm} = T_{i0}/eB_0a^2 = 404.2s^{-1}$. Values up to $n \sim 100$ have been computed. These plots shows good agreement through most of the scan. A shift in the real frequency may be explained taking into account that

the BT model is based on a two-fluid approximation, while the other code includes a gyrokinetic model.

Non-circular flux surfaces: dependence on the Shafranov shift and on the elongation.

Most present-day and future tokamaks have shaped equilibria and a small aspect ratio. Therefore is useful to perform simulations employing a shaped tokamak equilibria. The flux surface shape is specified by Shafranov shift, Δ and elongation, λ, via

$$\begin{aligned} R &= R_0 + \Delta(a) + a\cos\vartheta \\ z &= \lambda(a) a \sin\vartheta. \end{aligned}$$

Both, the Shafranov shift and the elongation are allowed to have radial dependence:

$$\begin{aligned} \Delta(a) &= \Delta_0 + (a/a_M)^2(\Delta_a - \Delta_0), \\ \lambda(a) &= \lambda_0 + (a/a_M)^2(\lambda_a - \lambda_0), \end{aligned}$$

where values with index '0' are values considered on-axis and values with index 'a' are values considered at the edge. To study the dependence of the mode on Shafranov shift and on the elongation the same profiles as above have been used.

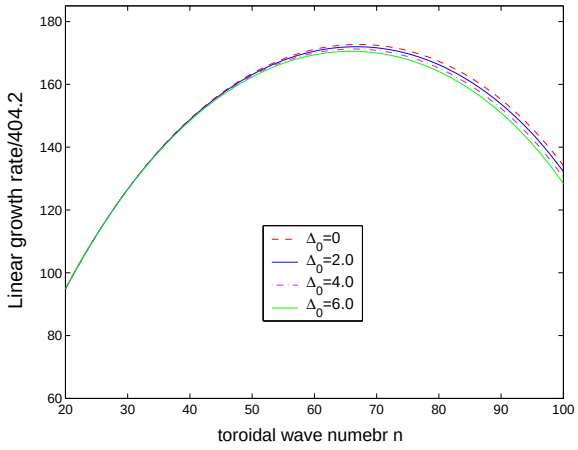

Figure 5.17: The dependence of the growth rate on the toroidal wave number for different values of Δ_0.

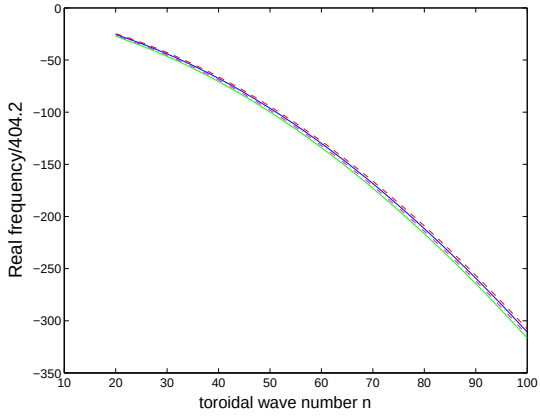

Figure 5.18: The real frequency vs. toroidal wave number, for different values of Δ_0.

First the dependence of the growth rate of the mode on the Shafranov shift has been studied. Figure (5.17) emphasizes the linear growth rate as a function the

toroidal wave number. Each curve in this plot corresponds to a different value of the Shafranov shift Δ_0. For the considered set of parameters, for each different value of Δ_0, the mode has a maximum at $n = 67$. At small values of the toroidal wave number the growth rate of the mode does not depend at all on the Shafranov shift. Increasing n, the mode is stabilizing with the increasing Δ_0. One can say that in this case, the increasing of the Shafranov shift slightly stabilizes the ITG mode. The modulus of the real frequency, figure (5.18) increases linearly with the increasing toroidal wave number and remains almost unchanged when Shafranov shift is included in the calculations.

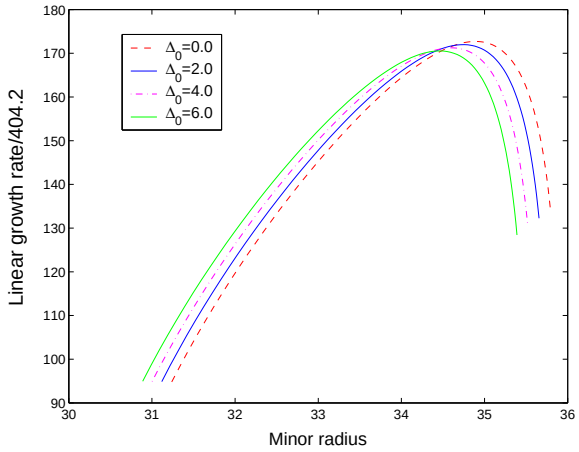

Figure 5.19: The growth rate vs. radial dependence (which is a solution of the beam tracing equations), for different values of Δ_0.

The full set of beam tracing equations is solved here, so that for each toroidal wave number one gets the radial position where the mode is localized. Figure (5.19) shows the linear growth rate vs. the corresponding radial position. For all Δ_0 considered, the radial position where the maximum growth rate occurs is almost the same. The localization of the mode at this radius is a consequence of how the parameter s_0 have been chosen.

The next step is to study the dependence on the elongation. Figure (5.20) shows the dependence of the growth rate on the toroidal wave number when different values of λ_0 are considered. It is noticed that the value of the toroidal wave number corresponding to the maximum growth rate is not the same. Figure (5.21) shows that, for all considered λ_0, the most unstable mode tends to localized at the same radial position, this being again a consequence of how the parameter s_0 was fixed. Both figures, (5.20) and (5.21), respectively, show that the impact of the elongation

λ on the most unstable mode is rather weak.

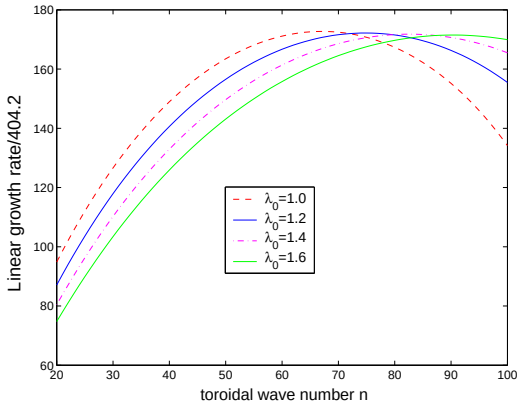

Figure 5.20: The dependence of the growth rate on the toroidal wave number for different values of λ_0.

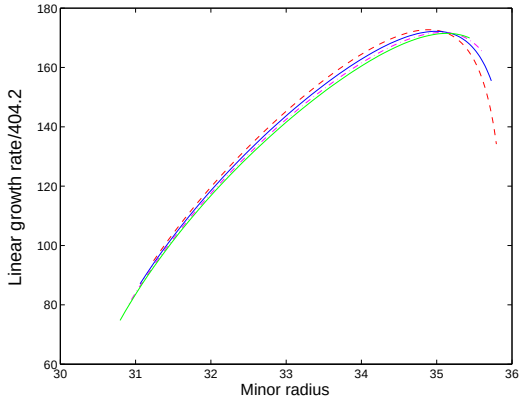

Figure 5.21: The growth rate vs. radial dependence (which is a solution of the beam tracing equations), for different values of λ_0.

Dependence on the magnetic shear

A very important quantity is the magnetic shear parameter $\hat{s} \equiv (r/q)(dq/dr)$. It is known that magnetic shear has a stabilizing effect on many microinstabilities, including ITG, ETG and TEM modes. Therefore, increasing in the magnetic shear is expected to lead to a large decreasing of the growth rate.

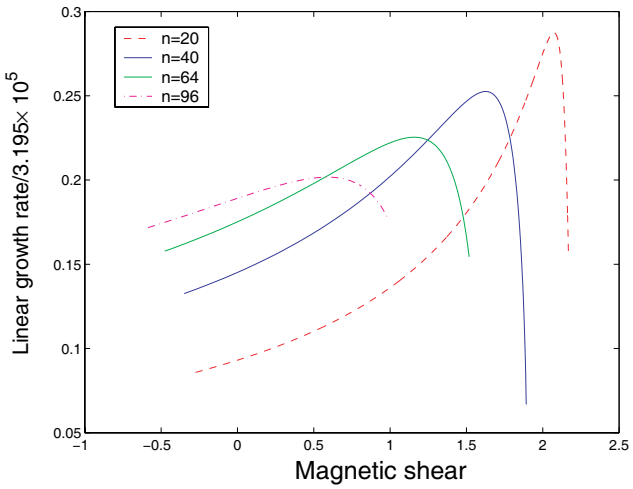

Figure 5.22: Growth rate as a function of the magnetic shear for different values of the toroidal wave number.

In order to vary the magnetic shear, the safety factor profile is changed. Figure

(5.22) shows the variation of the growth rate with the magnetic shear. Values of the toroidal wave number from 20 to 96 are considered. Negative magnetic shear is also considered. For each given toroidal wave number, the growth rate is stabilizing at large values of the magnetic shear. For negative magnetic shear the mode is found again to stabilize. The values of the magnetic shear where the linear growth rates reach their maximum is different for different values of n.

5.3.3 The transport

In this section we shall study the ion heat transport coefficients χ_i included by the ion temperature gradient mode. Different parameters effect on the transport have been studied mixing length estimation of χ_{imix} and the quasi-linear formula of χ_{iqs}, which was first derived in [102].

$$\chi_{imix} = \gamma/k_\perp^2 \tag{5.6}$$

$$\chi_{iqs} = \frac{1}{\eta_i}\left(\eta_i - \frac{2}{3} - \frac{20}{9\tau}\epsilon_n\right)\frac{\gamma^3/k_\perp^2}{\left(\omega_2 - \frac{5}{3}\omega_{Di}\right)^2 + \gamma^2} \tag{5.7}$$

where $k_\perp^2 = k_\theta^2(1 + s^2\langle\theta^2\rangle)$ with $\langle\theta^2\rangle = 0.5/\Phi_{\theta\theta}$.

In figure (5.23) is shown the scaling of the transport coefficient with the parameter $b_\theta = (k_\theta\rho_s)^2$, different values of the Shafranov shift being considered. When b_θ goes from 0.03 and 0.4, the transport is found to decrease. Here the effect of the mode width is important. With the increasing value of the toroidal wave number the width of the mode is decreasing in both, radial and poloidal directions, figures (5.24&5.25).

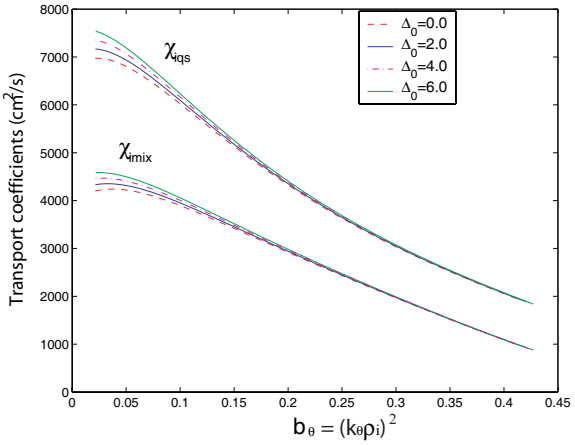

Figure 5.23: The variation of the transport coefficients with $b_\theta = (k_\theta\rho_s)^2$. Different values of the Shafranov shift are considered.

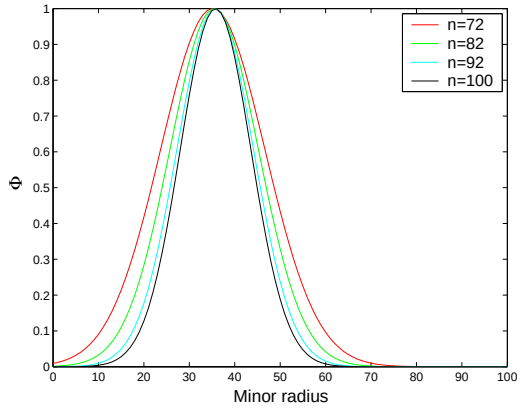

Figure 5.24: Radial profile of eigenfunction.

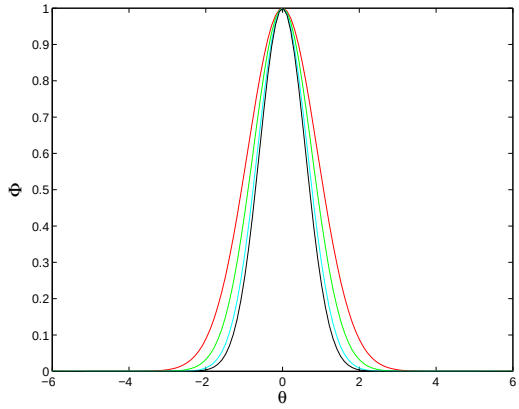

Figure 5.25: Poloidal profile of eigenfunction.

At small values of the parameter b_θ (small values of the toroidal wave number), the transport coefficients have a small increase with the increasing Shafranov shift. No difference appear at large value of the toroidal wave number.

On the other hand, figure (5.26), the elongation have a large impact on the transport coefficients. At small values of the parameter b_θ, increasing the elongation, a large decrease of the transport coefficients is noticed.

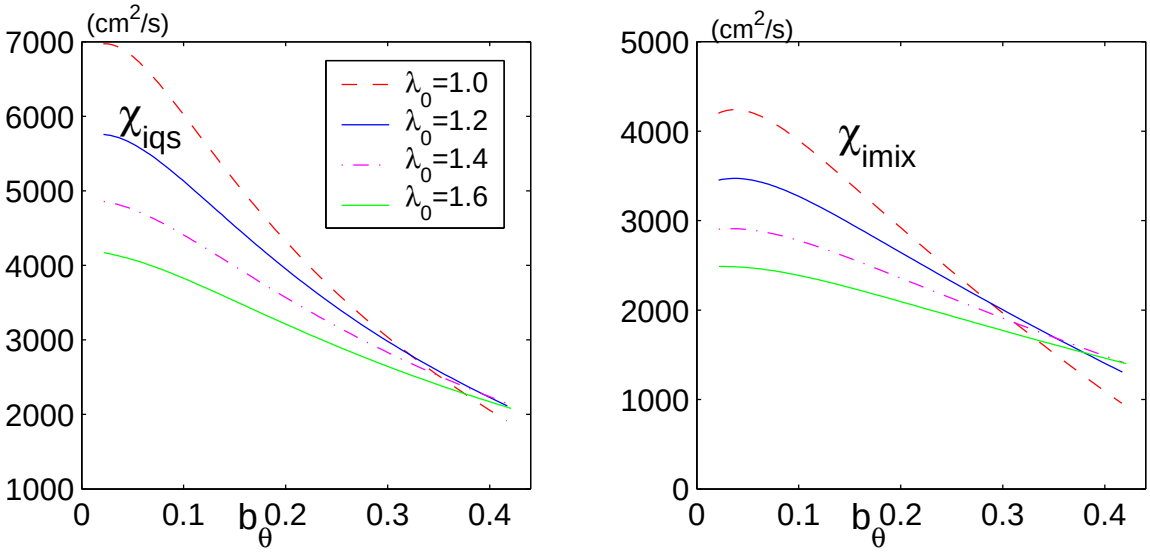

Figure 5.26: The variation of the transport coefficients with the elongation.

In the same time, the impact of the magnetic shear on the transport is found to be very important. As can be noticed in figure (5.27), large and negative values of the magnetic shear are reducing the transport significantly. In the figure mentioned

above, four different values of the toroidal wave number are considered. The decrease of the transport with the increasing toroidal wave number is also noticed.

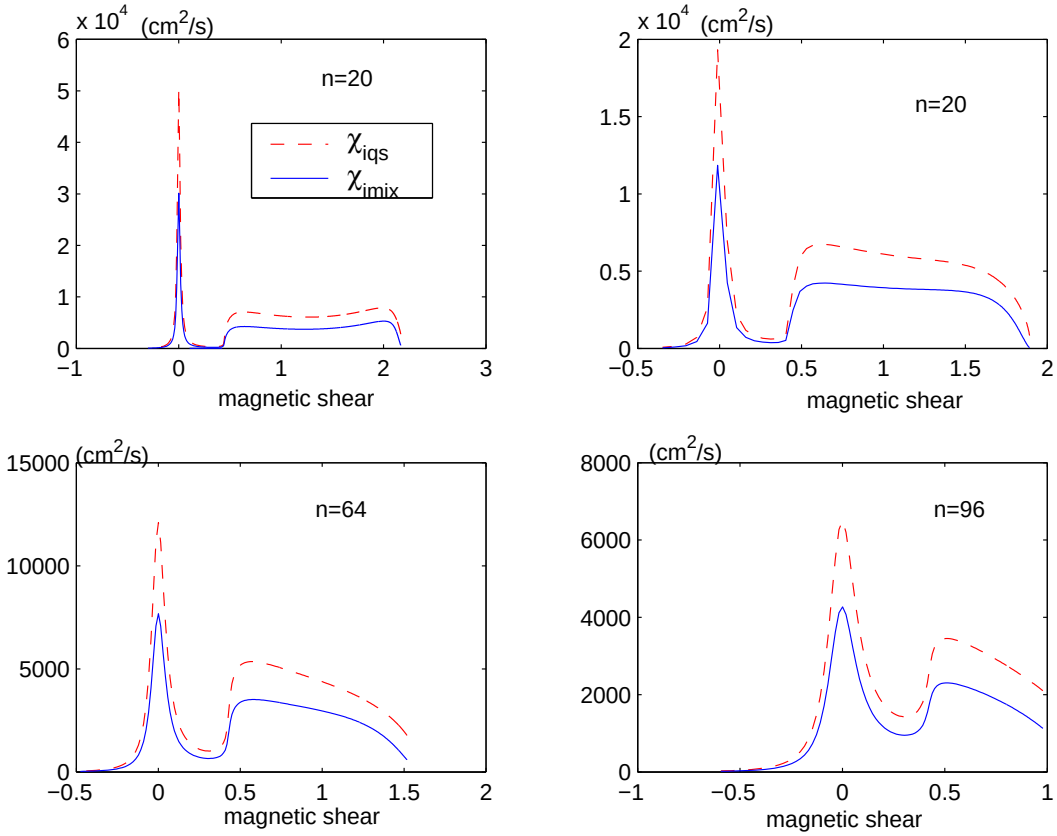

Figure 5.27: The variation of the transport coefficients with magnetic shear.

5.4 Summary

In this chapter the solution of the equations that describe the ITG turbulence is presented. By using the pWKB method the set of equations that describe the ITG mode is reduced to a set of algebraic equations easy to be solved by numerically treatment.

In the first step, the dependence of the growth rate of the ITG mode, computed with the BT model, is compared with results obtained with Guo and Weiland model. Studying the dependence of the mode on different parameters good agreement have been found between the two models. Parameters as ion temperature gradient length, density gradient length, $\tau = T_e/T_i$, have been found to have an large impact on the growth rate of the ion temperature mode.

Results from the full set of BT equations are also shown. The BT model reasonably reproduces results obtained with a much more complicated and time consuming code, a non-linear gyrokinetic code. Our model can be easily extended to arbitrary geometry so that dependence on the Shafranov shift and on the elongation has been also studied. The increasing in both of them, Shafranov shift and elongation, is found to have a slightly stabilizing effect on the linear growth rate of the ITG driven instabilities. The well known stabilizing effect of the magnetic shear is also found.

The scaling of the transport coefficients with different parameters has been also studied. The toroidal wave number, the elongation and the magnetic shear have been found to have a a large impact on the transport coefficients.

Chapter 6

Summary & Conclusions

Nowadays is commonly accepted that the anomalous transport is due to microinstabilities driven by temperature and density gradients. Two of the most important microinstabilities that appear in tokamak plasma, ion temperature gradient and electron temperature gradient driven turbulence, have been studied in this thesis.

Paraxial WKB technique. The main task of this work has been to apply a novel asymptotic approach in the study of microinstabilities that appear in tokamak plasma. This approach, called the paraxial WKB method, is different of all the other techniques that have been used till now to solve eigenvalue problems in the short wavelength limit ($\lambda \ll L$).

In this thesis, implementing the pWKB method, a new technique for solving the eigenvalue problem of the electrostatic ion temperature gradient microinstability in a tokamak geometry, has been obtained. The ITG modes can be thought as eigenmodes, while the interaction with plasma defines whether such a wave absorbs or releases energy.

In the first step, the model equations that describe the ITG instability in this new approach have been derived. The resulting equations have been obtained in a fluid limit which includes also the parallel ion dynamics. A hierarchy of three sets of algebraic equations have to be solved in this method. The first set, eqs. (4.65-4.66), is the conventional Hamiltonian system of geometrical optics, formulated in terms of the dispersion function as a Hamiltonian. It is decoupled from the other two sets and therefore, it can be solved independently. This allows to find the basic contour (the eigenmode position in the poloidal cross-section) and to judge about the existence and stability of the mode. Once the contour is found the second set of equations, eq.(4.67), comes into play. It involves second derivatives of the dispersion

function and provides information on the transverse structure of the mode. Finally, the third equation (4.70) should be involved if the first set (4.65-4.66) predicts the marginal stability. To all these equations we are going to refer as the BT model. In this new technique, apart from the common ansatz ($\lambda \ll L$), only two simplifying assumptions are done: a small variation of the medium characteristics on the mode width ($\Lambda \ll L$) and small increments $Im(\omega) \ll Re(\omega)$. Unlike the usually used ballooning representation, arbitrary radial dependence for the plasma parameters (density, temperature, safety factor, magnetic and rotational shear) and arbitrary geometry are allowed.

To solve the pWKB sets of equation that describe the ITG mode requires a numerical solution. So that, the second step in this thesis has been to write an eigenvalue code. Once the solution is found, one gets a complete set of information about the mode: frequency of the mode, radial and poloidal location of the mode, plasma parameters at that location (i.e temperature, density, safety factor, magnetic shear), wave vectors of the mode, width of the mode in both radial and poloidal direction (which give the relevance of the solution). If the solution is valid one can compute also the growth rate of the mode. A big advantage of this method is that the routine is very fast and can be easily included in transport codes.

In order to validate our approximation, comparison with an extensively used transport model, Weiland model, have been performed. Both models, BT and Weiland, are based on the same physics, the ion temperature gradient driven instability. In Weiland model, unlike the beam tracing, the wave-vector components are prescribed. Another difference is that, in Weiland model, the radial position of the eigenmodes cannot be assessed. In order to impose the same property in the BT model the two first equation in equation (4.66) were omitted. Finally, it should be noted that due to the limitation of the Weiland model the comparison was limited to the case of circular geometry. The normalized growth rates computed with both codes have been compared. Good agreement between the two models has been found, when the dependence of the normalized growth rate on different plasma parameters has been studied. The same dependence on parameters (i.e. ion temperature gradient length, density gradient length, $\tau = T_e/T_i$) as found in Weiland model, has been obtained also using our model. The parameters mentioned before are known to have a large impact on the growth rate of the ion temperature instability. In all the scans that were done using Weiland model, the parameter b_θ is included as an independent input parameter. In the BT approach, this parameter is a result of the calculations, so that one can derive the value of b_θ which corresponds to the most

unstable mode.

Comparison with results presented in [101] has been also done. There, a global gyrokinetic code is used to study the ion temperature gradient instability. Figure (5.16) shows a relatively good agreement between the results computed with the two models. The difference that appears can be explain because our model is done in a fluid limit, while the other results are obtained with a gyrokinetic model. Our calculations are at least three orders faster than those presented in [101] (i.e while in the gyrokinetic calculations it takes at least few hours to calculate one point, in our code this process takes a few seconds). In our new approach arbitrary geometry can be used so that the dependence of ITG growth rate on the Shafranov shift and on the elongation was also studied. The increasing in the Shafranov shift and in the elongation has been noticed to have a slightly stabilizing effect on the linear growth rate of the ITG driven instabilities. The well known stabilizing effect of the magnetic shear has been also found. Using our new code, the dependence of the transport coefficients on plasma parameters was studied. The transport has been found to decrease with the increasing of the toroidal wave number (increasing of the parameter b_θ). In the same time the magnetic shear is noticed to have a large impact on the transport coefficients. For negative and large values of the magnetic shear the transport coefficients become very small.

In conclusion, a new capable technique for analyzing the ion temperature gradient instability in plasma physics has been created. The technique is well suited for numerical implementation. The results obtained using this technique reproduces results computed with much more complicated and time consuming codes.

GS2 simulations. In the second part of this thesis, the experimentally observed electron heat transport has been compared with linear gyro kinetic stability calculations. The sensitivity scan around the parameters obtained from the experiment have revealed that the growth rate of the mode depends on several plasma parameters that are not usually considered when analyzing the experiments. Most clearly these are the density gradient and the collisionality. In the direct comparison of heat flux with the quasi-linear estimate a good agreement can only be obtained if these two effects are taken into account.

Many experimentally observed phenomena can be explained on the basis of the presented calculations. Both the experiments as well as the calculations show that a threshold for the TEM exists. Care is to be taken here though, because in gen-

eral many parameters change simultaneously, and one would have to re-analyze the experiments using the results of the calculations presented here.

The normalized growth rate obtained from the gyro kinetic stability calculations have been also compared with Weiland and GLF23 models. A relative good agreement has been found between GS2 and GLF23 models, whereas the Weiland model performs less well (especially the shear dependence). The comparison made with the empirical model have shown that the calculations presented in this thesis give in fact an easier functional form of the electron heat flux.

Despite the success of the comparison it should also be noted that not all properties can be explained. This is especially true for the dependence on the safety factor. It has been suggested that the widening of the spectrum in the non-linear state could account for such a dependence [67].

Bibliography

[1] J. Wesson, Tokamaks, Clarendon Press, Oxford, (1987)

[2] ITER Physics Basis, Nuclear Fusion **39** 2175 (1999)

[3] Y. Koide et al., Physical Review Letter **72** 3662 (1994)

[4] A. G. Peeters et al., 18th IAEA Fusion Energy Conference (Sorrento, 2000), IAEA-CN-77-EXP5/06

[5] T. S. Hahm, K. H. Burrell, Physics of Plasmas **2** 1648 (1995)

[6] V. M. Babič and V. S. Buldyrev, Short-Wavelength Diffraction Theory: Assimptotic Methods, Spinger series of wave phenomena (Springer Verlag, Berlin), **4**, (1991)

[7] S. I. Braginskii, Transport Process in a Plasma, Review of Plasma Physics, M. A. Leontovich (ed.), Consultants Bureau, **1** 205-311 (1965)

[8] J.B. Taylor, Phys. Plasma and Controlled Fusion Research **2** 323, International Atomic Energy Agency, Vienna (1977)

[9] Francis F. Chen. Introduction to plasma physics. Plenum Press, New York, 2^{nd} edition 563 (1978)

[10] J. Weiland, Collective modes in inhomogeneous plasma, IOP Publishing Ltd, (2000)

[11] B.B. Kadomtsev and O.P. Pogutse, Dissipative, trapped particle instability in a dense plasma, Sov.Phys.Doklady, **14(5)** 470 (1969)

[12] Chuan Sheng Liu, Temperature Gradient Instability in Axisymmetric Systems, Phys. Fluids, **12(7)** 1489 (1969)

[13] F. Wagner and U. Stroth, Plasma Phys. Control. Fusion **35** 1321 (1993)

[14] L. I. Rudakov and R. Z. Sagdeev, Dokl. Akad. Nauk SSR **138** 581 (1961)

[15] B. Coppi, M. N. Rosenbluth and R. Z. Sagdeev, Phys. Fluids, vol. **10** 582 (1967)

[16] J. Weiland , A. Jarmén and H. Normand Nucl. Fusion **29** 1810 (1989)

[17] P.H. Rutherford and E.A. Frieman, Phy. Fluids **11** 569 (1968)

[18] J.B. Taylor and R.J Hastie, Phys. Plasmas **10** 479 (1968)

[19] P.J Catto, W.M. Tang, and D.E. Baldwin, Phys. Plasmas **23** 693 (1981)

[20] P.J. Catto, Phys. Plasmas **20** 556 (1978)

[21] T.M Antonsen and B. Lane, Phys. Fluids **23** 1205 (1980)

[22] E.A. Frieman and L. Chen, Phys. Fluids **26** 502 (1982)

[23] P.J. Catto, and K. T. Tang, Phys. Fluids 20 (1977) 396.

[24] W.W. Lee, Phys. Fluids **26** 556 (1983)

[25] D.H.E. Dubin, J.A. Krommes, C. Oberman, and W.W. Lee, Phys. Fluids **26** 3524 (1983)

[26] S.C. Yang and D.I. Choi, Phys. Lett. A **108** 25 (1985)

[27] T.S. Hahm, W.W. Lee and A. Brizard, Phys. Fluids **31** 1940 (1988)

[28] T.S. Hahm, Phys. Fluids **31** 2670 (1988)

[29] A.J. Brizard, J. Plasma Phys. **41** 541 (1989)

[30] A.J. Brizard, Phys. Fluids B **1** 1381 (1989)

[31] A.J. Brizard, Ph.D. Dissertation, (Princeton University, 1990)

[32] H. Qin, W.M. Tang, and R. Rewoldt, Phys. Plasmas **5** 1035 (1998)

[33] H. Qin, Ph. D. Dissertation (Princeton University) (1998)

[34] H. Qin, W.M. Tang, W. Lee, and G. Rewoldt, Phys. Plasmas **6** 1575 (1999)

[35] H. Qin, W.M. Tang, and G. Rewoldt, Comput. Phys. Commun. (in press)

[36] H. Sugama, Phys. Plasmas **7** 466 (2000)

[37] A.J. Brizard, Phys. Plasmas **7** 4816 (2000)

[38] A.J. Brizard, Phys. Fluids B **4** 1213 (1992)

[39] A.J. Brizard, J. Plasma Phys. **41** 541 (1988)

[40] W. Horton, J. Sendlak, D.-I. Choi, and B. Hong, Phys. Fluids **28** 3050 (1985)

[41] M. Kotschenreuther, G. Rewoldt, and W. M. Tang, Comp. Phys. Commun. **88** 128 (1995)

[42] Kotschenreuther, M. (1998). Private communication.

[43] N.J. Lopes Cardozo, Plasma Phys. Contr. Nucl. Fusion **37** 799 (1995)

[44] F. Ryter et al., Plasma Phys. Contr. Fusion **43** A323 (2001)

[45] R. Goldston et al., Plasma Phys. Contr. Fus. Res., Proc. 11^{th} IAEA Conf. Kyoto 1986, **3** 75 (1987)

[46] V. Alikaev et al., Plasma Phys. Contr. Fus. Res., Proc. 11^{th} IAEA Conf. Kyoto 1986, **3** 111 (1987)

[47] F. Wagner et al., Phys. Rev. Lett. **56** 2187 (1989)

[48] G. Taylor et al., Nucl. Fusion **34** 121 (1989)

[49] T.C. Luce et al., Phys. Rev. Lett. **68** 52 (1992)

[50] W. Suttrop et al., Plasma Phys. Contr. Fusion **39** 2051 (1997)

[51] B. Coppi, Comments Plasma Phys. Cont. Fusion **5** 261 (1980)

[52] F. Ryter et al., Nucl. Fusion **43** 1396 (2003)

[53] B.J.D. Tubbing, N.J. Lopes Cardozo, M.J. van der Wiel, Nucl. Fusion **27** 1843 (1987)

[54] J.C.M. DeHaas et al., Nucl. Fusion **31** 1261 (1991)

[55] D.L. Brower et al., Phys. Rev. Lett. **65** 337 (1990) and Phys. Rev. Lett. **67** 200 (1990)

[56] N.J. Lopes Cardozo, J.C.M. DeHaas Nucl. Fusion **30** 521 (1990)

[57] Y. Takase et al., Nucl. Fusion **32** 2246 (1992)

[58] J.W. Conner, Plasma Phys. Contr. Fusion **37** A119 (1995)

[59] J.A. Konings et al., Nucl. Fusion **37** 199 (1997)

[60] G. Tardini, A.G. Peeters, G.V. Pereverzev, F. Ryter, J. Stober, Nucl. Fusion **42** 258 (2002)

[61] F. Ryter et al., Phys. Rev. Lett. **86** 2325 (2001)

[62] F. Ryter et al., Phys. Rev. Lett. **86** 5498 (2001)

[63] G.T. Hoang, Phys. Rev. Lett. **87** 125001 (2001)

[64] J. Weiland, A.B. Jarmen, H. Nordman, Nucl. Fusion **29** 1810 (1989)

[65] C. Angioni et al., Phys. Rev. Lett. **90** 205003 (2003)

[66] F. Jenko, W. Dorland, G.M. Hammett, Phys. Plasmas **8** 4096 (2001)

[67] X. Garbet, *private communications*

[68] R. E.Waltz et al., Phys. Plasmas **4** 2482 (1997)

[69] R. E. Waltz et al., Physics of Fluids **B 4** 3138 (1992)

[70] F. Imbeaux, X. Garbet, Plasma Phys. Contr. Fusion **44** 1425 (2002)

[71] P. Mantica et al., Plasma Phys. Contr. Fusion **44** (2002) 2185

[72] Yu.A.Kravtsov and Yu.I.Orlov, Geometrical Optics of Inhomogeneous Media, Springer Series of Wave Phenomena, **6** Springer-Verlag, (1990)

[73] I.B Bernstein and L. Friedland, in: Handbook of Plasma Physics, (eds), M.N. Rosenbluth and R.Z. Sagdeev, **1** (1983)

[74] M. Brambilla and A. Cardinali, Plasma Psysics **24** 1187 (1982)

[75] E. Mazzacato, Phys. Fluids, **B1** 1855 (1989)

[76] G.V. Pereverzev, Proceedings of the 20th European Physical Society 26-30 July 1993 (European Physical Society, Petit-Lancy, 1993), **17C** p.III-885

[77] V.A. Fock, Electrodynamic Diffraction and Propagation Problem, Pergamon, (1965)

[78] S. Choudhary and L.B. Fesel, IEEE Trans. Antennas Propag, **AP21** 827 (1973)

[79] S. Nowak, A.Orefice, Phys. Fluid, **B5** 1993 (1945)

[80] A. G. Peeters, Phys. Plasma, 4386 (1996)

[81] G.V. Pereverzev, in: B.B. Kadomtsev (Ed.), Paraxial WKB Solution of a Scalar Wave Equation. In: Review of Plasma Physics, **19**, Consultant Bureau, New York, 1 (1996)

[82] G.V. Pereverzev, Phys. Plasma **5** 3529 (1998)

[83] J.W. Conner,R.J. Hastie, and J.B. Taylor, Proc.R.Soc.London,Ser.A, 365 1 (1979)

[84] R.J. Hastie, K.W. Hesketh, and J.B. Taylor, Nucl. Fusion **19** 1223 (1979)

[85] S.C. Guo and J. Weiland, Nucl.Fusion **37** 1095 (1997)

[86] P.I. Catto, M.N. Rosenbluth and C.S. Liu, Phys. Fluids **16** 1719 (1973)

[87] M. Artun, W. M. Tang and G.Rewolt, Phys. Plasmas **2** 3384 (1995)

[88] R.E. Waltz, G.D.Kerbel, J. Milovich and G.M. Hammet, Phys. Plamsas **2** 2408 (1995)

[89] N. Mattor and P.H. Diamond, Phys. Fluids **31** 1180 (1988)

[90] G.M. Staebler and R.M. Dominguez, Nucl. Fusion **31** 1891 (1991)

[91] S. Hamaguchi and W. Horton, Phys. Fluids B **4** 319 (1992)

[92] F.L. Waelbroeck, T. M. Antonsen, Jr., P.N. Guzdar and A.B. Hassam, Phys. Fluids B **4**, 2441 (1992)

[93] M. Artun and W.M. Tang, Phys. Fluids B **4** 1102 (1992)

[94] J.G. Dong and W. Horton, Phsy. Fluids B **5** 1581 (1993)

[95] L. Bai, A. Fukuyama and M. Uchida, Phys. Plasmas **5** 989 (1998)

[96] T.A. Davydova and J. Weiland, Phys. Plasmas **7** 243 (2000)

[97] F. Romanelli, Phys. Fluids **B1** 1018 (1989)

[98] X. Q. Xu and M.N Rosenbluth, Phys. Fluids **B3** 627 (1991)

[99] A.G. Peeters , Phys. Plasma **5** 763 (1997)

[100] L. Friedman and I.B. Bernstein, Phys. Review A **22** 1680 (1980)

[101] S. Brunner, M. Fivaz, T.M. Tran, and J. Vaclavik, Phys. Palasmas **5** 3929 (1998)

[102] R.J Goldston, Plasma Phys. Control Fusion **26** 87 (1984)

Appendix A

Abreviation

	Heating and diagnostics systems
EC(R)H	Electron Cyclotron (Resonance) Heating
	Experimental devices
ASDEX	Axis-Symmetric Divertor Experiment
	Physics abbreviations
MHD	MagnetoHydroDynamics
ITG	Ion Temperature Gradient
ETG	Electron Temperature Gradient
TEM	Trapped Electron Mode
χ^e	Heat transport coefficient from Power Balance, perturbative analysis
ρ_{tor}	Toroidal flux coordinate
	Transport code and models
GS2	Gyrokinetic code
GLF23	Gyro Landau Fluid (from 2 dimensions and 3 dimensions simulations)

Appendix B

Useful relations

In the thesis, we use:

The geometry:

$$\begin{aligned} x &= Rcos\zeta; \\ y &= Rsin\zeta; \\ z &= a\lambda(a)sin\vartheta; \\ R &= R_0 + \Delta(a) + \left(cos\vartheta - \delta(a)sin^2\vartheta\right); \end{aligned} \tag{B.1}$$

Here $R_0 = 165$ cm is the major radius, ϑ and ζ are the poloidal and the toroidal angles. $\Delta(a)$, $\delta(a)$ and $\lambda(a)$ represent the Shafranov shift, the triangularity, respectively, the elongation.

The covariant basis vectors in toroidal coordinates are given by:

$$\begin{aligned} \vec{e}_a &= \left\{\left(\Delta' + cos\vartheta - (a\delta)' sin^2\vartheta\right) cos\zeta, \left(\Delta' + cos\vartheta - (a\delta)' sin^2\vartheta\right) sin\zeta, (a\lambda)' sin\vartheta\right\} \\ \vec{e}_\vartheta &= \left\{-asin\vartheta\left(1 + 2\delta cos\vartheta\right) cos\zeta, -asin\vartheta\left(1 + 2\delta cos\vartheta\right) sin\zeta, a\lambda cos\vartheta\right\} \\ \vec{e}_\zeta &= \left\{-Rsin\zeta, Rcos\zeta, 0\right\} \end{aligned} \tag{B.2}$$

and the associated reciprocal basis vectors:

$$\begin{aligned} \nabla a &= \frac{1}{d}\left\{\lambda cos\vartheta cos\zeta, \lambda cos\vartheta sin\zeta, sin\vartheta\left(1 + 2\delta cos\vartheta\right)\right\} \\ \nabla\vartheta &= \frac{1}{ad}\left\{-(a\lambda)' cos\vartheta sin\zeta, -(a\lambda)' sin\vartheta sin\zeta, \Delta' + cos\vartheta - (a\delta)' sin^2\vartheta\right\} \\ \nabla\zeta &= \frac{1}{R}\left\{-sin\zeta, cos\zeta, 0\right\} \end{aligned}$$

Metrix:

$$
\begin{aligned}
g^{aa} &= \frac{1}{d^2}\left[\lambda^2 cos^2\vartheta + sin^2\vartheta\left(1+2\delta cos\vartheta\right)^2\right] \\
g^{a\vartheta} &= \frac{1}{ad^2}\left[-\left(a\lambda\right)'\lambda sin\vartheta cos\vartheta + \left(\Delta' + cos\vartheta - \left(a\delta\right)' sin^2\vartheta\right) sin\vartheta\left(1+2\delta cos\vartheta\right)\right] \\
g^{\vartheta\vartheta} &= \frac{1}{a^2d^2}\left\{\left[\left(a\lambda\right)'\right]^2 sin^2\vartheta + \left(\Delta' + cos\vartheta - \left(a\delta\right)' sin^2\vartheta\right)^2\right\} \\
g^{\zeta\zeta} &= \frac{1}{R^2} \\
d &= \left(\Delta' + cos\vartheta - \left(a\delta\right)' sin^2\vartheta\right)\lambda cos\vartheta + sin^2\vartheta\left(1+2\delta cos\vartheta\right)\left(a\lambda\right)', \quad \sqrt{g} = adR
\end{aligned}
\tag{B.3}
$$

Definitions:

$$
\begin{aligned}
\vec{v}_E &= \frac{\vec{e}_{||}\times\nabla\phi}{B}, \quad \vec{v}_{\star i} = c\frac{\vec{e}_{||}\times\nabla p_i}{en_iB}, \quad \vec{v}_{||} = -i\frac{c_0^2}{\omega}\vec{e}_{||}\cdot\nabla\left[\frac{e\phi}{T_0} + \frac{1}{T_0 n_e}\tilde{p}_i\right]\vec{e}_{||} \\
\vec{v}_{\pi i} &= \frac{\vec{e}_{||}\times\nabla\cdot\pi_i}{en_iB}, \quad \vec{v}_{pi} = \frac{1}{B\omega_{ci}}\left[\frac{\partial}{\partial t}\vec{E} + \left(\vec{v}_i\cdot\nabla\right)\vec{E}\right] \quad c_0 = \sqrt{\frac{T_0}{m_i}}, \quad \rho_0 = \frac{c_0}{\omega_{ci}} \\
\vec{v}_{Di} &= \frac{2cT_i}{eB}\frac{\vec{e}_{||}\times\nabla B}{B}, \quad \vec{v}_{D0} = \frac{2cT_0}{eB}\frac{\vec{e}_{||}\times\nabla B}{B}, \quad \vec{v}_{\star 0} = cT_0\frac{\vec{e}_{||}\times\nabla n_i}{en_iB}
\end{aligned}
\tag{B.4}
$$

$$
\begin{aligned}
\nabla\cdot\left[n_i\left(\vec{v}_{\pi i} + \vec{v}_{pi}\right)\right] &= \nabla\cdot\left[\frac{n_i}{\omega_{ci}}\frac{\partial}{\partial t}\left(\vec{e}_{||}\times\vec{v}_i\right)\right] = i\omega\rho_0^2\nabla_\perp\cdot\left[n_i\nabla_\perp\frac{e\phi}{T_0} + \nabla_\perp\frac{\tilde{p}_i}{T_0}\right] \\
\nabla\cdot\left(n_i\vec{v}_{||}\right) &= -i\frac{c_0^2}{\omega}\nabla\cdot\left[n_i\nabla_{||}\frac{e\phi}{T_0}\right] - i\frac{c_0^2}{T_0\omega}\nabla\cdot\left[\nabla_{||}\tilde{p}_i\right] \\
\nabla\cdot\left(n_i\vec{v}_{\star i}\right) &= \frac{1}{T_0}\vec{v}_{D0}\cdot\nabla\tilde{p}_i \\
\vec{v}_E\cdot\nabla n_i &= -n_i\vec{v}_{\star 0}\cdot\nabla\frac{e\phi}{T_0}, \\
n_i\nabla\cdot\vec{v}_E &= n_i\vec{v}_{D0}\cdot\nabla\frac{e\phi}{T_0},
\end{aligned}
\tag{B.5}
$$

$$
\begin{aligned}
\omega_{Di,0} &= -2\frac{c_{i,0}^2}{\omega_{ci}}\tilde{k}_z, \quad \omega_{\star i,0} = -\frac{c_{i,0}^2}{\omega_{ci}}\frac{1}{L_n}\tilde{k}_\vartheta, \quad \omega_{\star e} = \frac{c_e^2}{\omega_{ci}}\frac{1}{L_n}\tilde{k}_\vartheta \\
\frac{\omega_{Di,0}}{\omega_{\star e}} &= -\frac{2T_{i,0}}{T_e}\frac{\tilde{k}_z L_n}{\tilde{k}_\vartheta}, \quad \frac{\omega_{\star 0}}{\omega_{\star e}} = -\frac{T_0}{T_e}, \quad L_{Te} = -\frac{T_e}{T_e'}, \quad L_{ne} = -\frac{n_e}{n_e'}
\end{aligned}
\tag{B.6}
$$

where

$$
\begin{aligned}
\tilde{k}_z &= \left\{\tilde{A}\frac{k_\vartheta}{\sqrt{g}} - \tilde{B}\frac{k_a}{\sqrt{g}} + \tilde{A}\Theta k_\zeta g^{aa} g^{\zeta\zeta} + \tilde{B}\Theta k_\zeta g^{a\vartheta} g^{\zeta\zeta}\right\}, \; \tilde{k}_\vartheta = \left(\frac{k_\vartheta}{ad} + \frac{\Theta k_\zeta g^{aa}}{R}\right), \\
k_\perp^2 &= \left[k_a^2 g^{aa} + k_\vartheta^2 g^{\vartheta\vartheta} + 2k_a k_\vartheta g^{a\vartheta} + k_\zeta^2 g^{\zeta\zeta}\right], \; k_{||}^2 = \frac{I^2}{B^2}\left[k_\zeta - \frac{\Theta}{\sqrt{g}}k_\vartheta\right]^2 \\
\tilde{A} &= \Delta' + \left(cos\vartheta - (\delta a)' \, sin^2\vartheta\right), \quad \tilde{B} = -asin\vartheta\,(1 + 2\delta cos\vartheta)
\end{aligned}
\tag{B.7}
$$

Appendix C

Derivation of the wave amplitude equation

In the fourth chapter (section 4.4.3) the amplitude equation was introduced. Only the final result has been related there, so that here we are going to give some more details concerning that calculation. As have been already said, in order to determine the amplitude equation, one starts from the equation

$$\mathcal{L}X_2 + \mathcal{M}X_1 = 0 \tag{C.1}$$

with $\mathcal{L}$ and $\mathcal{M}$ given by the equations (4.60) and (4.61), and X_1 is given in the equation (4.64). The first term in the expression of the matrix $\mathcal{M}$, in equation (4.61), writes explicitly:

$$\frac{\partial L}{\partial \vec{k}} = \frac{\omega}{c_0}\frac{\partial L}{\partial \nabla S} = \begin{pmatrix} \left(2\vec{K} + \vec{K}_\star - \vec{K}_D\right) & \frac{n_0}{n_i}\left(2\vec{K} - \vec{K}_D\right) & 0 & 0 \\ \left(\frac{3}{2}\eta_i - 1\right)\vec{K}_{\star 0} & 0 & 0 & -\frac{5}{2}\frac{T_0}{T_i}\vec{K}_{Di} \\ 0 & 0 & 0 & 0 \\ 0 & 0 & 0 & 0 \end{pmatrix} \tag{C.2}$$

By applying Fredholm alternative, one find that the equation (C.1) has solution if and only if

$$X_1^\star \cdot \mathcal{M}\left[X_1\right] = 0 \qquad or \qquad X_1 \cdot \mathcal{M}^\star\left[X_1^\star\right] = 0 \tag{C.3}$$

In order to get an equation for the wave amplitude, the two relations in the above equation are added, so that one get the equation 4.69. Let us evaluate one by one the terms that appear in equation 4.69:

1)

$$A^{\star}e^{\star}M_{\nabla}\left[A\right]e+AeM_{\nabla}^{\star}\left[A^{\star}\right]e^{\star}=A^{\star}e^{\star}\left(\frac{\partial\mathcal{L}}{\partial\nabla S}\cdot\nabla A\right)e+Ae\left(\frac{\partial\mathcal{L}^{\star}}{\partial\nabla S}\cdot\nabla A^{\star}\right)e^{\star}$$

The contravariant components of the group velocity V are given by (see the proof at the end of this appendix):

$$\vec{V}=H^{\alpha}=\mathbf{e}^{\star}\frac{\partial L}{\partial\nabla S}\mathbf{e}=e_{i}e^{j}\frac{\partial L_{j}^{i}}{\partial\vec{k}}$$

where $\vec{k}=\nabla S$ and $k_{\alpha}=S_{\alpha}$. The equation (**??**) can be written in the form:

$$A^{\star}e^{\star}M_{\nabla}\left[A\right]e+AeM_{\nabla}^{\star}\left[A^{\star}\right]e^{\star}=A^{\star}V\cdot\nabla A+AV^{\star}\cdot\nabla A^{\star}\tag{C.4}$$

The group velocity V is real, so that in the above relation we have $V^{\star}$=V.

2)

$$\begin{aligned}AA^{\star}\left(e^{\star}M_{\nabla}\left[e\right]+eM_{\nabla}^{\star}\left[e^{\star}\right]\right)=AA^{\star}\left(\right.&\nabla\cdot V-2\frac{c_{0}}{\omega}\nabla\cdot\vec{K}\left[\bar{\Phi}_{0}^{2}+\frac{n_{0}}{n_{i}}\bar{\Phi}_{0}\bar{p}_{0}\right]-\\&\frac{c_{0}}{\omega}\bar{\Phi}_{0}^{2}\nabla\cdot\left(\vec{K}_{\star}-\vec{K}_{D}\right)+\frac{5}{2}\frac{c_{0}}{\omega}\nabla\cdot\left(\frac{T_{0}}{T_{i}}\vec{K}_{Di}\right)\bar{p}_{0}\bar{T}_{0}-\\&\frac{c_{0}}{\omega}\left[\nabla\left(\frac{n_{0}}{n_{i}}\right)\cdot\left(2\vec{K}-\vec{K}_{D}\right)-\frac{n_{0}}{n_{i}}\nabla\cdot\vec{K}_{D}+\nabla\cdot\left(\left(\frac{3}{2}\eta_{i}-1\right)\vec{K}_{\star}\right)\right]\bar{\Phi}_{0}\bar{p}_{0}\left.\right)\end{aligned}\tag{C.5}$$

where

$$\begin{aligned}\nabla\cdot V&=\nabla\cdot\left(e^{\star}\frac{\partial L}{\partial\nabla S}e\right)\\&=\nabla e^{\star}\cdot\frac{\partial L}{\partial\nabla S}e+e^{\star}\nabla\cdot\frac{\partial L}{\partial\nabla S}e+e^{\star}\frac{\partial L}{\partial\nabla S}\cdot\nabla e\end{aligned}$$

It is very easy to prove that:

$$-\nabla e^{\star}\cdot\frac{\partial L}{\partial\nabla S}e+e\frac{\partial L^{\star}}{\partial\nabla S}\cdot\nabla e^{\star}=0$$

3)

$$\begin{aligned}AA^{\star}\left(e^{\star}\tilde{M}\left[e\right]+e\tilde{M}^{\star}\left[e^{\star}\right]\right)&=AA^{\star}\left(\right.2\frac{c_{0}}{\omega}\nabla\cdot\vec{K}\left[\bar{\Phi}_{0}^{2}+\frac{n_{0}}{n_{i}}\bar{\Phi}_{0}\bar{p}_{0}\right]\\&\quad+2\left(\frac{c_{0}}{\omega}\vec{K}\cdot\frac{\nabla n_{i}}{n_{i}}\bar{\Phi}_{0}^{2}-\delta\frac{T_{0}}{T_{e}}\bar{\Phi}_{0}\bar{T}_{0}\right)\left.\right)\end{aligned}\tag{C.6}$$

By adding the equation (C.4, C.5, C.6) we get

$$A^{\star}V\cdot\nabla A+AV\cdot\nabla A^{\star}+AA^{\star}\{\ \nabla\cdot V+2\frac{c_0}{\omega}\vec{K}\cdot\left(\frac{\nabla n_i}{n_i}\bar{\Phi}_0^2-\nabla\left(\frac{n_0}{n_i}\right)\bar{\Phi}_0\bar{p}_0\right)$$

$$+\frac{c_0}{\omega}\nabla\left(\frac{n_0}{n_i}\right)\cdot\vec{K}_D\bar{\Phi}_0\bar{p}_0+\frac{5}{2}\frac{c_0}{\omega}\bar{p}_0\bar{T}_0\nabla\left(\frac{T_0}{T_i}\right)\cdot\vec{K}_{Di}+\frac{c_0}{\omega}\left(\bar{\Phi}_0^2+\frac{n_0}{n_i}\bar{\Phi}_0\bar{p}_0\right)\nabla\cdot\vec{K}_D-$$

$$\frac{c_0}{\omega}\left(\bar{\Phi}_0^2+\left(\frac{3}{2}\eta_i-1\right)\bar{\Phi}_0\bar{p}_0\right)\nabla\cdot\vec{K}_{\star}+\frac{5}{2}\frac{c_0}{\omega}\bar{p}_0\bar{T}_0\left(\frac{T_0}{T_i}\right)\nabla\cdot\vec{K}_{Di}-2\delta\frac{T_0}{T_e}\bar{\Phi}_0\bar{T}_0\ \}=0\quad\text{(C.7)}$$

Writing explicitly the terms in the equation (C.7) we get the equation for the wave amplitude given in the 4th chapter .

Proof

The contra-variant components of the group velocity V are given by:

$$\vec{V}=H^{\alpha}=\mathbf{e}^{\star}\frac{\partial L}{\partial\nabla S}\mathbf{e}=e_ie^j\frac{\partial L_j^i}{\partial\vec{k}},\ \ \vec{k}=\nabla S,\ k_{\alpha}=S_{\alpha}\qquad\text{(C.8)}$$

Lets consider the eigenvalue problem for the matrix:

$$Le=He,$$

and take its derivative in respect with $\partial/\partial s^{\alpha}$. One gets

$$L^{\alpha}e+Le^{\alpha}=H^{\alpha}e+He^{\alpha}$$

By multiplying the last relation with $e^{\star}$ on the left hand side, one has:

$$e^{\star}L^{\alpha}e+e^{\star}Le^{\alpha}=e^{\star}H^{\alpha}e+e^{\star}He^{\alpha},$$

$$e^{\star}L^{\alpha}e=-e^{\star}Le^{\alpha}+e^{\star}H^{\alpha}e+e^{\star}He^{\alpha},$$

$$Le^{\alpha}=He^{\alpha},e^{\star}e=1$$

$$e^{\star}L^{\alpha}e=H^{\alpha}-e^{\star}He^{\alpha}+e^{\star}He^{\alpha},$$

The result is then:

$$e^{\star}L^{\alpha}e=H^{\alpha}$$

Appendix D

The equations for the toroidal ITG mode in rotating tokamak plasma.

The dispersion relation that describe the ITG mode in a rotating tokamak plasma, in the beam tracing approximation, has already been included in the 4th chapter (section 4.4.4). We find useful to include here also the set of fluid equations from where that dispersion relation has been obtained.

When rotation is included, the total velocity writes:

$$\vec{v} = \vec{v}_0 + \vec{v}_i, \;\; where \;\; \vec{v}_0 = v_{0\vartheta} \nabla a \times \nabla\zeta + v_{0\zeta} \nabla\zeta$$

$\vec{v}_0$ represents the background velocity and it satisfies the incompressibility condition:

$$\nabla \cdot \vec{v}_0 = 0$$

The poloidal, the toroidal and the parallel background velocities are taken to be:

$$\begin{aligned} v_{0\vartheta} &= \frac{B_p \langle V_p \rangle}{\langle B_p \rangle}, \\ v_{0\zeta} &= \frac{B_t \langle V_p \rangle}{\langle B_p \rangle} - R\Omega_E, \\ v_{||0} &= \frac{B \langle V_p \rangle}{\langle B_p \rangle} - \frac{\langle R B_t \rangle}{B} \Omega_E \end{aligned} \tag{D.1}$$

The equations above were related in [99] and represent a standard result that a divergence free flow can be expressed in a component parallel to the magnetic field proportional to B, and a rigid body rotation in the toroidal direction. B_P and B_t represent the poloidal and toroidal magnetic field, respectively. Because of the

toroidal symmetry the divergence free nature of the magnetic field can be written as $\nabla \cdot B_p = 0$.

The toroidal magnetic field satisfies $Bt = B_{t0}R_0/R$, where R is the major radius. The poloidal magnetic field satisfies $Bp = B_{p0}R_0\nabla\Psi/R(\nabla\Psi)_0$. The lowest order electric field potential is assumed to be a flux function, and the radial electric field E_r satisfies $E_r = E_{r0}RB_p/R_0B_{p0}$. Ω_E is a rotation frequency in the toroidal direction which is connected with the effective radial electric field $\Omega_E = c\langle E_r^\star\rangle/\langle RB_p\rangle$.

The fluid equations that describe the ITG mode, with rotation included, take the form:

(I) ***The continuity equation***:

$$\frac{\partial \tilde{n}_i}{\partial t} + \vec{v}_0 \cdot \nabla \tilde{n}_i + \nabla \cdot (n_i \vec{v}_i) = 0 \tag{D.2}$$

(II) ***The energy equation***:

$$\frac{3}{2} n_i \left(\frac{\partial}{\partial t} + \vec{v}_0 \cdot \nabla \right) \tilde{T}_i + \frac{3}{2} n_i \vec{v}_i \cdot \nabla T_i + n_i T_i \nabla \cdot \vec{v}_i - \frac{5}{2} n_i \left(\vec{v}_{\star i} - \vec{v}_{Di} \right) \cdot \nabla \tilde{T}_i = 0 \tag{D.3}$$

(III) ***The parallel velocity equation***:

$$\left(\frac{\partial}{\partial t} + \vec{v}_0 \cdot \nabla\right) \frac{v_{||i}}{c_0} + \frac{\vec{v_i}}{c_0} \cdot \nabla v_{||0} + c_0 \vec{e}_{||} \cdot \nabla \frac{e\Phi}{T_0} + \frac{n_0}{n_i} c_0 \vec{e}_{||} \cdot \nabla \frac{\tilde{p}_i}{p_0} = 0 \tag{D.4}$$

Starting from the above set of equations (I,II,III), considering also the perturbed electron density response $\delta n_e/n_e = e\Phi/T_e$ and the perturbation of the ion pressure $\tilde{p}_i = \tilde{n}_i T_i + n_i \tilde{T}_i$, applying step by step the beam tracing approach, one gets the dispersion relation, equation 4.71, introduced in chapter 4.

Appendix E

Geometric optics in plasma characterized by non-Hermitian dielectric tensors

The geometric-optics approximation is widely used in studying electromagnetic phenomena in inhomogeneous plasmas of various types and dimensions. Most of the studies are based on ray tracing although the general theory, which uses the properties of the local dielectric tensor $\underline{\epsilon}(\vec{k},\omega;\vec{r},t)$ of the plasma also allows one to find the wave amplitude of the electromagnetic field along the rays. The theory developed to date is limited to cases where the tensor $\underline{\epsilon}$ is Hermitian or "almost" Hermitian, namely it can be written as $\underline{\epsilon} = i\underline{\epsilon}_A + \underline{\epsilon}_H$, where $\underline{\epsilon}_H$ is Hermitian and $\underline{\epsilon}_A$ is the anti-Hermitian part, with $\underline{\epsilon}_A \ll \underline{\epsilon}_H$. This restriction on the type of the dielectric tensor was imposed in order to provide a dispersion relation $D(\vec{k},\omega,\vec{r},t) = det\underline{\epsilon}_H = 0$ with a real solution $\omega = \omega(\vec{k};\vec{r},t)$ for real $\vec{k}$. The anti-Hermitian part $\underline{\epsilon}_A$ then contributes only to the equation for the electromagnetic field and usually leads to a weak energy dissipation along the rays. This case was discussed in chapter 4, when the beam tracing technique was presented.

There are, however, cases where $\underline{\epsilon}$ has a large anti-Hermitian part. This was actually the situation in the study of the ITG mode. The use of only the Hermitian part in these cases is not justified. The determinant of the dielectric tensor is complex and therefore also cannot directly provide a real Hamiltonian for the ray equations. The problem in this case can be solved by reordering the terms in the expression for the determinant of $\underline{\epsilon}$ so that it can be written in the form $D = A(D_0 + iD_1)$, where D_0 and D_1 are real and $D_1 \ll D_0$. Then D_0 is used in the ray equations and the small correction D_1 is used to determine the transport of energy along the rays. This way of constructed the real Hamiltonian is nontrivial

in the general case, and involves a study of all the terms in the expression for the determinant. Moreover the possibility of such a reordering is more a priori.

E.1 The ray equation

L. Friedland and I.B. Bernstein have proposed in [100] a more simple and general method of constructed the real Hamiltonian plasmas. The method does not require the study of the determinant itself. They have derived also the general transport equation for the amplitude of the electric field of the wave along the ray, but this one is not going to be discussed here.
To present this method we are considering again the equations

$$\underline{L} \cdot \vec{a}_0 = 0 \tag{E.1}$$

$$\underline{L} \cdot \vec{a}_1 + \underline{M} \cdot \vec{a}_0 = 0 \tag{E.2}$$

As have been discussed in chapter 4, the equation (**??**) has nontrivial solution if

$$D = det(\underline{L}) = 0. \tag{E.3}$$

In chapter 4, we have restricted ourself to the case $\epsilon = \epsilon_H + i\epsilon_A$, with $\epsilon_A \ll \epsilon_H$. If, however, the dielectric tensor is non-Hermitian, in the expression of $\underline{L}$ appears this time $\underline{\epsilon}$ and not only $\underline{\epsilon}_H$. So that the equation (E.3) in general cannot have a real solution $\omega = \omega(\vec{k}; \vec{r}, t)$ for real $\vec{k}$. Since D is a complex function both, its real and imaginary parts, must simultaneously vanish. This gives two, not necessarily consistent dispersion relations for ω and $\vec{k}$. Thus, in order to be consistent we must modify the zero-order dispersion relation. This can be done in the following way. Let us add and subtract a small quantity

$$\Delta = i\nu \frac{\partial \underline{L}}{\partial \omega} \cdot (\vec{a}_0 - \frac{i}{k}\vec{a}_1), \tag{E.4}$$

in the equation (E.3). We assume ν in (E.4) real and of order $1/k$. Then equation (E.3) becomes

$$(\underline{L} + i\nu \frac{\partial \underline{L}}{\partial \omega}) \cdot \vec{a}_0 - \frac{i}{k}(\underline{L} + i\nu \frac{\partial \underline{L}}{\partial \omega}) \cdot \vec{a}_1 - \frac{i}{k}\underline{M} \cdot \vec{a}_0 - i\nu \frac{\partial \underline{L}}{\partial \omega} \cdot \vec{a}_0 = 0 \tag{E.5}$$

We define $\Omega = \omega + i\nu$ and correct to the first order in k

$$\tilde{\underline{L}} = \underline{L}(\vec{k}, \Omega; \vec{r}).$$

The equations (E.1) and (E.2) become:

$$\underline{\tilde{L}} \cdot \vec{a}_0 = 0, \tag{E.6}$$

$$\frac{i}{k}\underline{\tilde{L}} \cdot \vec{a}_1 + \frac{i}{k}\underline{M} \cdot \vec{a}_0 + i\nu\frac{\partial \underline{L}}{\partial \omega} = 0. \tag{E.7}$$

Note that the only difference between equations (E.1) and (E.6) in that in the latter we are formally allowing the frequency Ω to have small imaginary part $i\nu$. This assumption introduces a new term in the first-order equation (E.7) as compared to (E.2). The modified dispersion relation is therefore

$$\tilde{D} = det(\underline{\tilde{L}}) = D(\vec{k}, \Omega; \vec{r}) \tag{E.8}$$

On separating real and imaginary part in (E.8), one gets a set of two equations for two quantities ω and ν, and the aforementioned inconsistency is removed. One can also use the smallness of ν and derive a real dispersion relation for ω and $\vec{k}$, independent of ν. This can be conveniently done in the following way. Let us rewrite (E.7) in the form

$$D(\Omega) = D_0(\Omega) + iD_1(\Omega) \tag{E.9}$$

where D_0 and D_1 are the real and imaginary parts of the determinant $D(\omega)$. For simplicity the arguments $\vec{k}$ and $\vec{r}$ will not be indicated explicitly. On multiplying

$$D^H(\Omega) = D_0(\Omega) - iD_1(\Omega) \tag{E.10}$$

one gets

$$\Phi(\Omega) = DD^H = D_0^2(\Omega) + D_1^2(\Omega) = 0 \tag{E.11}$$

Correct to the second order in ν, this equation can be written

$$\Phi(\Omega) = \Phi(\omega) + i\nu\Phi_\omega(\omega) - \frac{1}{2}\nu^2\Phi_{\omega\omega}(\omega) = 0 \tag{E.12}$$

Since $\Phi(\omega) \geq 0$, ν will be real if and only if

$$\Phi_\omega(\omega) = 0 \tag{E.13}$$

and

$$\Phi_{\omega\omega}(\omega) \geq 0 \tag{E.14}$$

In this case

$$\nu = \pm\frac{2\Phi(\omega)}{\Phi_{\omega\omega}(\omega)} \tag{E.15}$$

The plus and minus signs in this solution correspond to the zeros $\Omega = \omega + i\nu$ of $D^H(\Omega)$ and $D(\Omega)$, respectively. Note that the real parts of the zeros are identical. Note also that equations (E.13) and (E.14) define a minimum of the function $\Phi(x)$ at the point $x = \omega$.

To find the radial position, the poloidal angle, the radial and poloidal wave number one has to solve the set of equations:

$$\frac{\partial \Phi_\omega}{\partial a} = \frac{\partial \Phi_\omega}{\partial \vartheta} = \frac{\partial \Phi_\omega}{\partial k_a} = \frac{\partial \Phi_\omega}{\partial k_\vartheta} = \Phi_\omega = 0 \tag{E.16}$$

By solving the equations (E.16) with the appropriate initial conditions, one can simultaneously determine ν from equation (E.15). The smallness of ν in comparison with ω will then give an estimate of wether the geometric-optics approximation can be applied in a given case.